UNIVERSITY OF BIRMINGHAM

DESIGN OF MICROWAVE HYBRID COUPLERS USING INTER-COUPLED RESONATORS

by

SHANI LU

A thesis submitted to the University of Birmingham for the degree of

MASTER OF PHILOSOPHY

School of Electronic, Electrical and Computer Engineering

The University of Birmingham

April 2012

Abstract

Design techniques for two-port coupled resonator filters are extended here to four-port coupled resonator circuits. Formulations to represent scattering parameters in terms of the general coupling matrix for four-port coupled resonator circuits are derived. The major part of this work is concerned with the synthesis of the coupled resonator hybrid couplers. Two types of hybrid couplers, $90°$ and $180°$, are presented. The design approach is based on an analytic solution, calculating the coupling matrix from the equivalent circuit of conventional hybrids. To verify the design methodology, an X-band coupled resonator $90°$ hybrid coupler is implemented using waveguide cavities.

Acknowledgements

I am extremely grateful for the guidance and support of my supervisor Prof. Mike Lancaster. He gave me many important advice and helpful suggestions during my study. I would also like to express my appreciation to Dr. Paul Smith and Dr. Fred Huang for their useful advice in numerous discussions. Many thanks for Warren Hay for the fabrication of the waveguide device and Dr. Xiaobang Shang for his help during the measurements.

My thanks go to Carlos Alberto Leal Sevillano whose help and friendship has been invaluable. Thanks to Atsushi Saito and my office mates who have helped make working in EDT group a very pleasant experience. Finally, my sincere gratitude goes to my parents, without whose support this work would never have been completed.

Table of Contents

Chapter 1

Introduction

1.1 Purpose of study

Inter-coupled resonators have been used for many years to make microwave filters [1]. A simplest topology for a two-port coupled resonator filter is given in Figure 1.1, where the solid dots are resonators and the line linking two resonators represents the coupling between them.

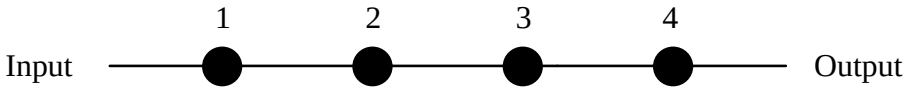

Figure 1.1: A two-port coupled resonator filter.

Synthesis of two-port coupled resonator filters has been well presented in literature such as [2]. A general technique for the design of coupled resonator filters is based on coupling coefficients of inter-coupled resonators and external quality factors of the input and output resonators [3]. The design technique used for two-port filters has been extended to three-port circuits such as power dividers and diplexers [4]. The novel network in [4] can do the function of filtering and power division at the same time. However, this theory can also be extended to a four-port network as depicted in Figure 1.2.

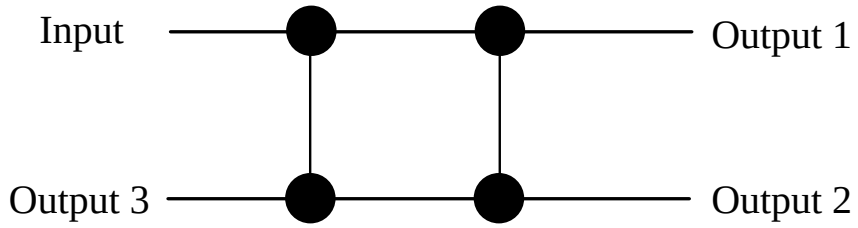

Figure 1.2: A four-port coupled resonator circuits.

This research work aims to design hybrid couplers based on inter-coupled resonators. The proposed coupled resonator hybrid couplers will have an embedded filtering function, and will be used in a new type of Butler matrix [5]. The Butler Matrix is a very attractive beam-forming network due to its ability to form orthogonal beams in a simple design.

Once the resonator configuration is known for the whole Butler matrix, the whole matrix can be considered as a resonator superstructure [6], allowing for optimisation of bandwidth and band shape.

A recent work [7] proposed a 60 GHz smart antenna receiver subsystem, where an antenna array, a 4×4 Butler matrix, and bandpass filters are integrated into a single substrate. This subsystem has been proven suitable for low-cost 60GHz indoor communication. Shown in Figure 1.3 is the block diagram of the RF front-end with the antenna array.

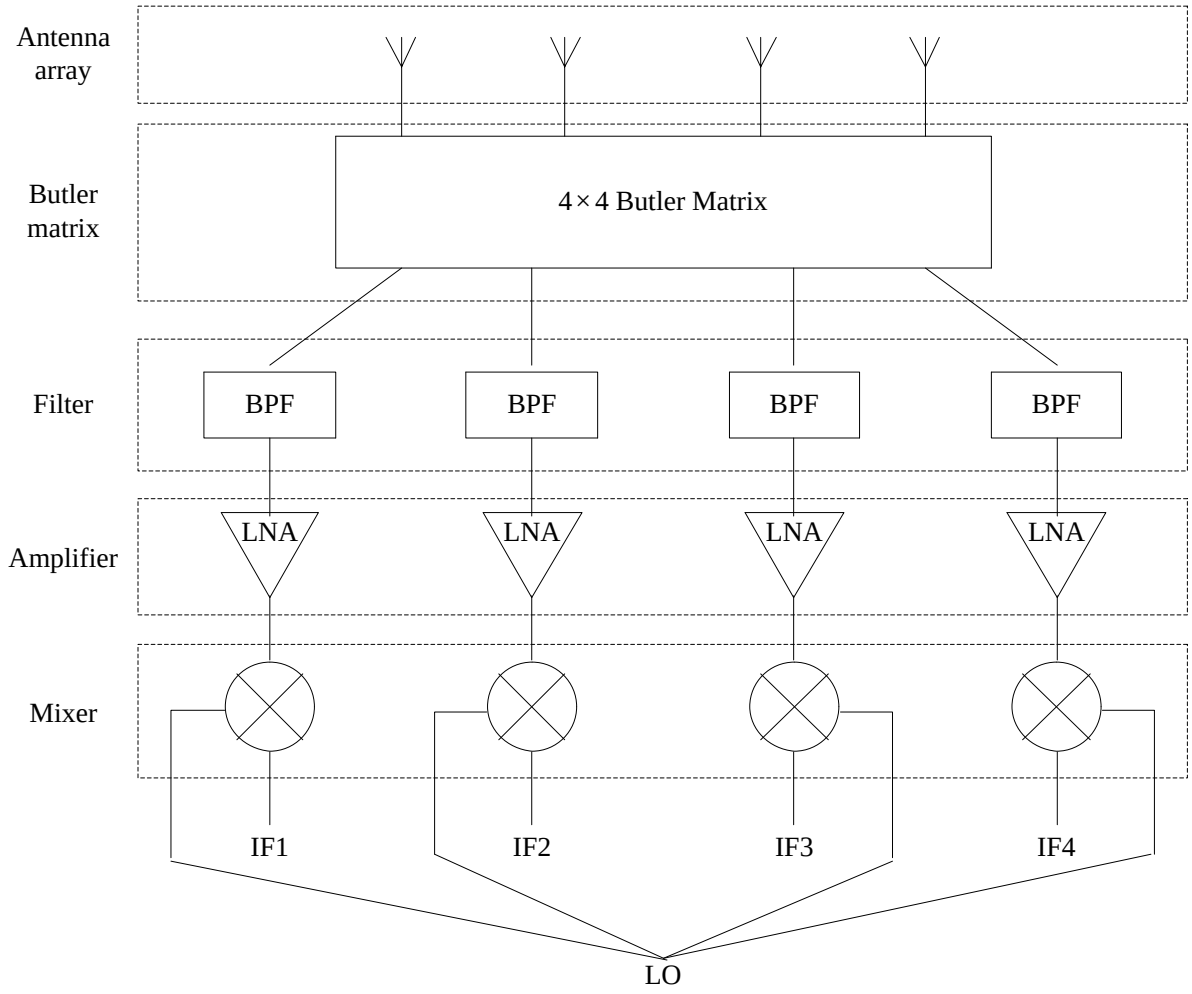

Figure 1.3: Block diagram of the RF front-end with antenna array.

Compared with the subsystem shown in Figure 1.3, the proposed structure will potentially reduce the size of whole system since the filtering function is embedded in the couplers. The topology of such a resonator superstructure is given in Figure 1.4.

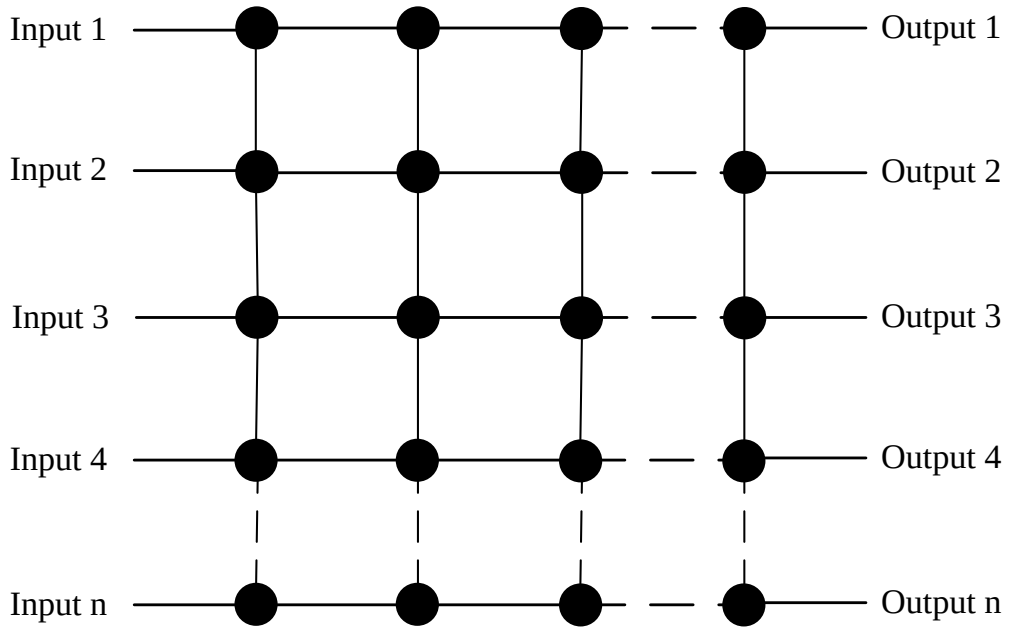

Figure 1.4: A resonator superstructure.

1.2 Structure of thesis

An introduction to directional couplers and hybrid couplers is given in the rest of this chapter, along with some of the most common applications. We briefly describe related theories of a two-port coupled resonator filter, including the coupling matrix representation and formulations for coupling coefficients and external quality factors.

The general coupling matrix is of importance for representing two-port filter topologies. In Chapter 2, we extend this concept to general four-port coupled resonator circuits. An important formulation to represent the scattering parameters in terms of the general coupling matrix is derived. This formula provides the basis for this research work.

In Chapter 3, an approach to design coupled resonator hybrid couplers is proposed. Both $90°$ hybrid couplers and $180°$ hybrid couplers are covered. For each section, we start by discussing some general properties of the conventional hybrid coupler, and then synthesize a

coupled resonator hybrid coupler from the equivalent circuit. Calculations of coupling coefficients and external quality factors are explained in details. Numerical examples of coupled resonator hybrids are also given.

Chapter 4 presents the implementation of an X-band $90°$ hybrid coupler using waveguide cavity resonators. Waveguide cavity resonators are chosen because of their high unloaded quality factors. After a brief introduction to some general properties of the waveguide cavity resonator, we discuss the extraction of coupling coefficients and external quality factors from physical structures. Design of the physical dimensions of the coupled-resonator 90° hybrid coupler is also provided. Finally, we discuss the fabrication and measurement results of the proposed device.

The final chapter provides conclusions drawn from this research work and suggestions of further research directions.

1.3 Directional couplers overview

Directional couplers [8] are passive microwave devices used for power division or power combining. Figure 1.5 (a) shows an arbitrary power division, where an input signal is divided by the coupler into two signals of lesser power. When used as a combiner, the coupler takes two signals to provide only one output. The coupler may be a three-port component as illustrated in Figure 1.5, or maybe a four-port component.

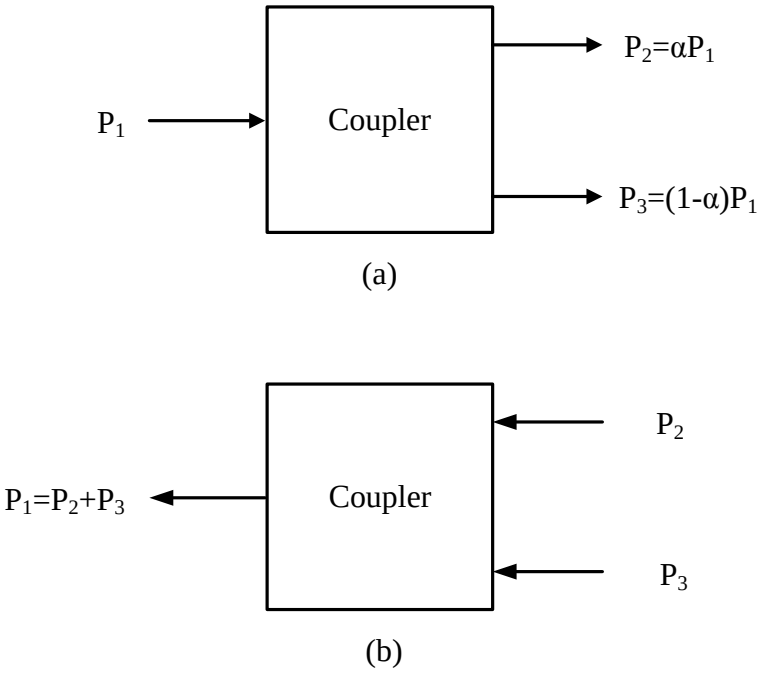

Figure 1.5: (a) An arbitrary power division and (b) power combining [9].

With reference to Figure 1.6 (a), which is a commonly used symbol for directional couplers, the ideal directional coupler has the property that a wave incident in port 1 couples power into ports 2 and 3 but not into port 4. For the wave incident in port 4, the power is coupled into ports 2 and 3 but not into port 1. Thus ports 1 and 4 are uncoupled. Similarly, ports 2 and 3 are also uncoupled. However, port 4 is usually terminated with a matched load and not accessible to the user. This results in a three-port component as shown in Figure 1.6 (b).

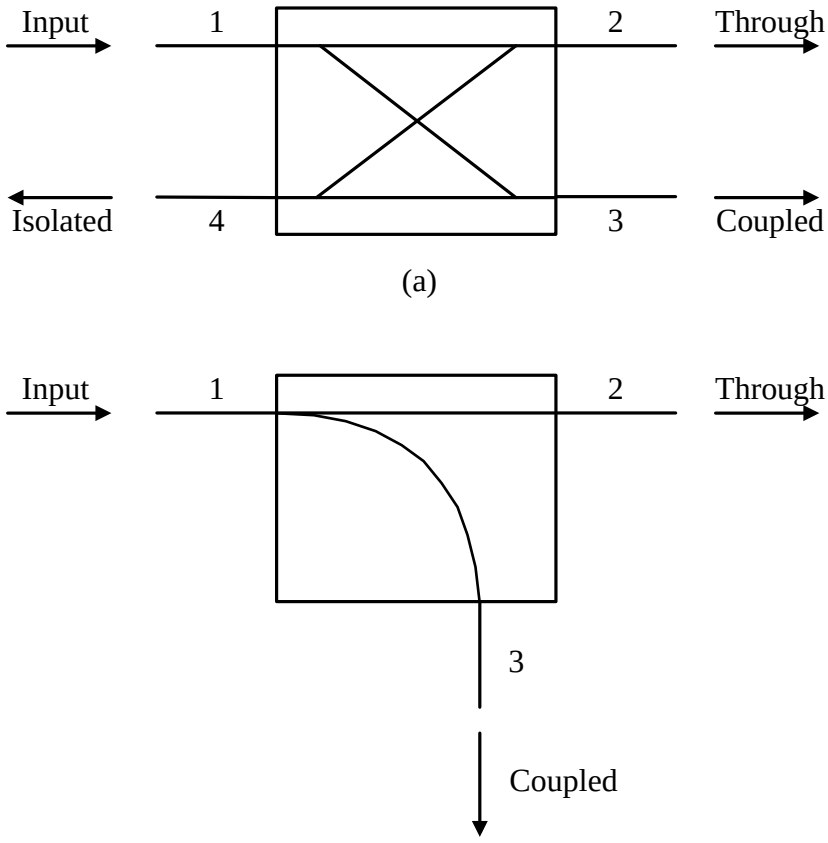

Figure 1.6: (a) Symbol for directional couplers and (b) symbol for a directional coupler with port 4 terminated with a matched load [9].

The performance of a directional coupler is characterized by two parameters, the coupling and the directivity. The coupling factor indicates the fraction of the input power that is coupled to the output port, and the directivity is a measure of how well the power is coupled in the desired direction. Let P_1 be the power supplied to port 1, P_3 be the coupled power in the forward direction in port 3 and P_4 be the power coupled in the backward direction in port 4. The coupling in decibels is then given by

$$C = 10 \log \frac{P_1}{P_3} \tag{1.1}$$

The directivity is defined as

$$D = 10 \log \frac{P_3}{P_4} \tag{1.2}$$

Ideally, the power P_4 coupled in port 4 should be zero, and therefore the directivity of the coupler would be infinite.

The ideal directional coupler, as illustrated in Figure 1.6 (a), is a lossless reciprocal four-port network matched at all ports with $S_{14} = S_{23} = 0$. Thus the scattering matrix [9] has the form

$$[S] = \begin{bmatrix} 0 & S_{12} & S_{13} & 0 \\ S_{12} & 0 & 0 & S_{24} \\ S_{13} & 0 & 0 & S_{34} \\ 0 & S_{24} & S_{34} & 0 \end{bmatrix} \tag{1.3}$$

Several properties of the ideal directional coupler may be deduced from the symmetry and unitary properties of its scattering matrix [10]. If we take the product of row 1 with the conjugate of row 4 in (1.3), and similarly row 2 with the conjugate of row 3, we obtain

$$S_{12}S_{24}^* + S_{13}S_{34}^* = 0 \tag{1.4}$$

$$S_{12}S_{13}^* + S_{24}S_{34}^* = 0 \tag{1.5}$$

If we note that $\left|S_{12}S_{24}^*\right| = \left|S_{12}\right|\left|S_{24}\right|$, (1.4) and (1.5) are seen to give

$$\left|S_{12}\right|\left|S_{24}\right| = \left|S_{13}\right|\left|S_{34}\right| \tag{1.6}$$

$$\left|S_{12}\right|\left|S_{13}\right| = \left|S_{24}\right|\left|S_{34}\right| \tag{1.7}$$

Now divide (1.6) by (1.7) to obtain

$$\frac{|S_{24}|}{|S_{13}|} = \frac{|S_{13}|}{|S_{24}|} \tag{1.8}$$

which implies that

$$|S_{13}| = |S_{24}| \tag{1.9}$$

so that the coupling between ports 1 and 3 equals that between ports 2 and 4.

Use of (1.9) in (1.6) gives

$$|S_{12}| = |S_{34}| \tag{1.10}$$

so that the coupling between ports 1 and 2 is the same as that between ports 3 and 4.

Then the product of the first row with its conjugate in (1.3) yields

$$|S_{12}|^2 + |S_{13}|^2 = 1 \tag{1.11}$$

similarly,

$$|S_{12}|^2 + |S_{24}|^2 = 1 \tag{1.12}$$

By properly choosing the terminal planes on ports 1 and 3, we can adjust the phase angle of scattering parameters, so that

$$S_{12} = S_{34} = C_1 \tag{1.13}$$

$$S_{13} = C_2 e^{j\alpha} \tag{1.14}$$

$$S_{24} = C_2 e^{j\beta} \tag{1.15}$$

where C_1 and C_2 are real, and α and β are phase constants to be determined.

Use of (1.13) and (1.14) in (1.11) gives

$$C_1^2 + C_2^2 = 1 \tag{1.16}$$

Substituting (1.13) to (1.15) into (1.4) yields a relation between the two phase constants as

$$\alpha + \beta = \pi \pm 2n\pi \tag{1.17}$$

In practice, there are two particular choices:

1. The $90°$ coupler: The phase constants are chosen equal, $\alpha = \beta = \pi/2$. Then the scattering matrix has the form

$$[S] = \begin{bmatrix} 0 & C_1 & jC_2 & 0 \\ C_1 & 0 & 0 & jC_2 \\ jC_2 & 0 & 0 & C_1 \\ 0 & jC_2 & C_1 & 0 \end{bmatrix} \tag{1.18}$$

2. The $180°$ coupler: The phase constants are chosen to be $180°$ apart, $\alpha = 0$, $\beta = \pi$. Then the scattering matrix has the form

$$[S] = \begin{bmatrix} 0 & C_1 & C_2 & 0 \\ C_1 & 0 & 0 & -C_2 \\ C_2 & 0 & 0 & C_1 \\ 0 & -C_2 & C_1 & 0 \end{bmatrix} \tag{1.19}$$

1.4 Hybrid couplers overview

Directional couplers can be designed for arbitrary power division. However, hybrid couplers [9] are special cases of directional couplers with equal power division (3dB), which implies

$$C_1 = C_2 = \frac{1}{\sqrt{2}} \tag{1.20}$$

Hybrid couplers have either a 90 °or a 180 °phase shift between the output ports.

1.4.1 90 °hybrid couplers functional description

The 90 ° hybrid coupler, also known as the quadrature hybrid coupler, is a 3dB directional coupler with 90 ° phase difference in the two output ports. With reference to a 90 ° hybrid symbol shown in Figure 1.7, a signal applied to port 1 will be evenly split into two components with a 90 °phase difference at ports 2 and 3, and port 4 will be isolated.

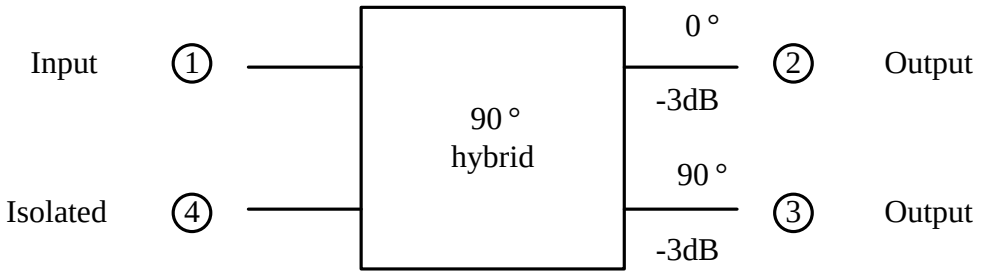

Figure 1.7: Symbol of a 90 °hybrid coupler [9].

The branch-line hybrid coupler [9] has a 90 °phase difference between ports 2 and 3 when fed at port 1, and is an example of the 90 °hybrid coupler. Its scattering matrix has the form

$$[S] = \frac{1}{\sqrt{2}} \begin{bmatrix} 0 & 1 & j & 0 \\ 1 & 0 & 0 & j \\ j & 0 & 0 & 1 \\ 0 & j & 1 & 0 \end{bmatrix} \tag{1.21}$$

1.4.2 180 °hybrid couplers functional description

The 180 °hybrid coupler is a 3dB directional coupler with a 180 °phase shift between the two output ports. It can also be operated so that the two outputs are in phase. With reference to

Figure 1.8, a signal applied to port 4 will be split equally into two components with 180 ° phase difference at ports 2 and 3, and port 1 will be isolated. If the input is applied to port 1, it will be evenly divided into two in-phase components at port 2 and 3, and port 4 will be isolated. Conversely, signals input into ports 2 and 3 will add at port 1 and the difference of the two signals will appear at port 4.

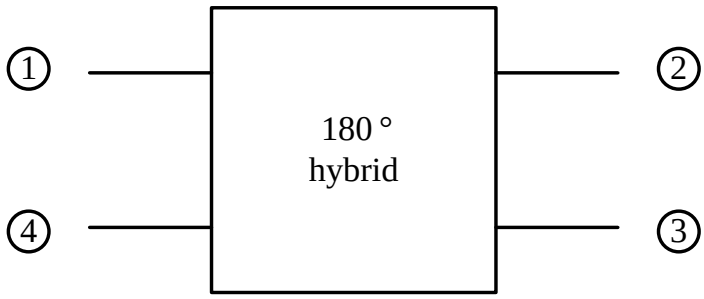

Figure 1.8: Symbol for a 180 °hybrid coupler.

The rat-race hybrid coupler [9] has a 180 ° phase shift between ports 2 and 3 when fed at port 4, and is an example of the 180 °hybrid coupler. Its scattering matrix has the form

$$[S] = \frac{1}{\sqrt{2}} \begin{bmatrix} 0 & 1 & 1 & 0 \\ 1 & 0 & 0 & -1 \\ 1 & 0 & 0 & 1 \\ 0 & -1 & 1 & 0 \end{bmatrix} \tag{1.22}$$

1.4.3 Hybrid couplers common applications

Hybrid couplers are used in many practical circuits such as power dividers, power combiners, mixers [11] and other microwave components and systems. An example of 90 ° hybrid couplers being used in power splitter and power combiner networks to produce a power amplifier [12] is given in Figure 1.9.

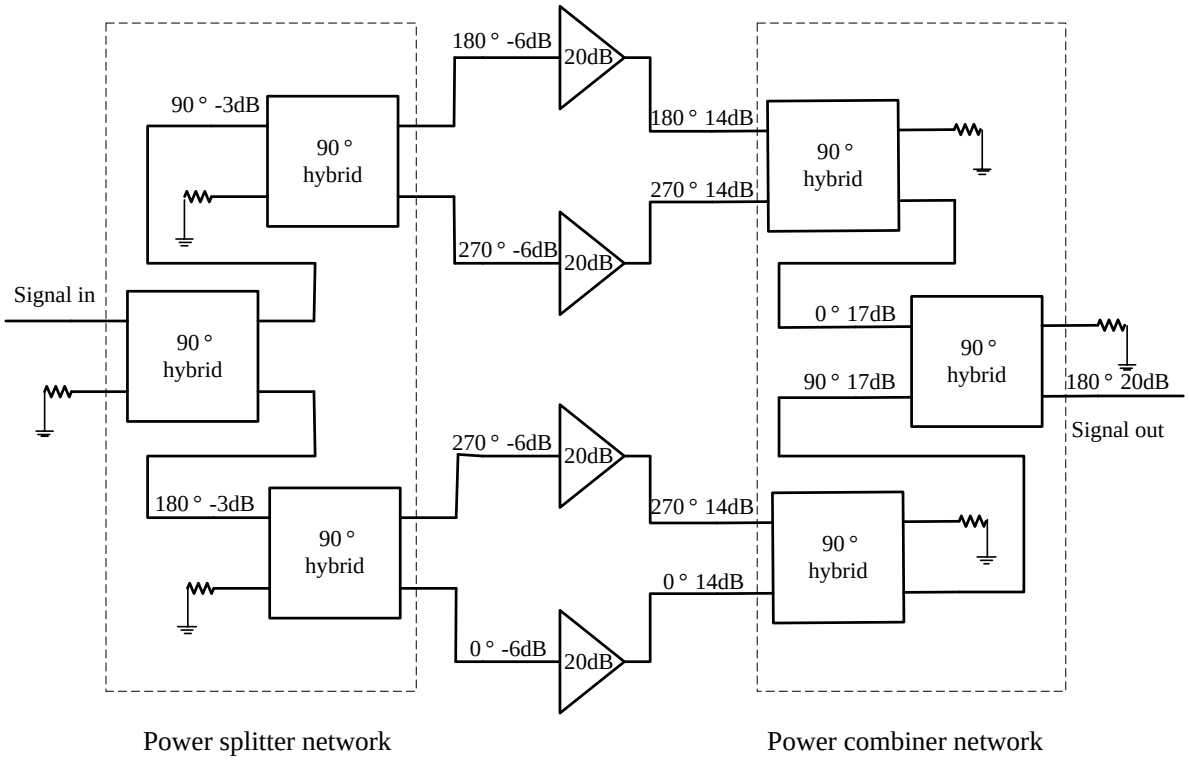

Figure 1.9: 90 ° hybrid couplers used in a power amplifier.

The hybrid couplers can be used to combine power as well as splitting it. As shown in Figure 1.9, an input signal is first split up to feed multiple low power amplifiers, then combined to produce a single output with high power. The phases of inputs to each power combiner are arranged such that the inputs are 90 ° out of phase with each other. With reference to Figure 1.10, this causes the power to add at the output of the combiner and to cancel at the isolation port.

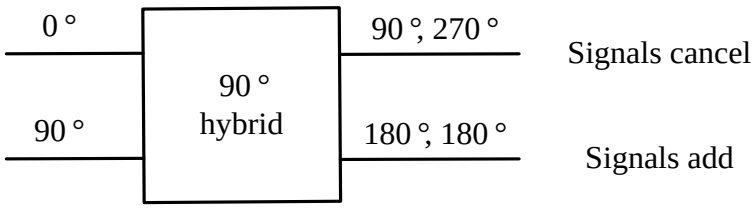

Figure 1.10: Phase arrangement on a 90 ° hybrid power combiner.

The $90°$ hybrid couplers, together with phase shifters, are also used in beam-forming networks [13], such as the Butler matrix [14], to create a radio beam in any prescribed direction. The Butler matrix was first described by Jesse Butler and Ralph Lowe [15]. It takes 2^n inputs and performs a spatial Fast Fourier Transform (FFT) to provide 2^n orthogonal beams. The schematic diagram of a 4×4 Butler matrix is shown in Figure 1.11.

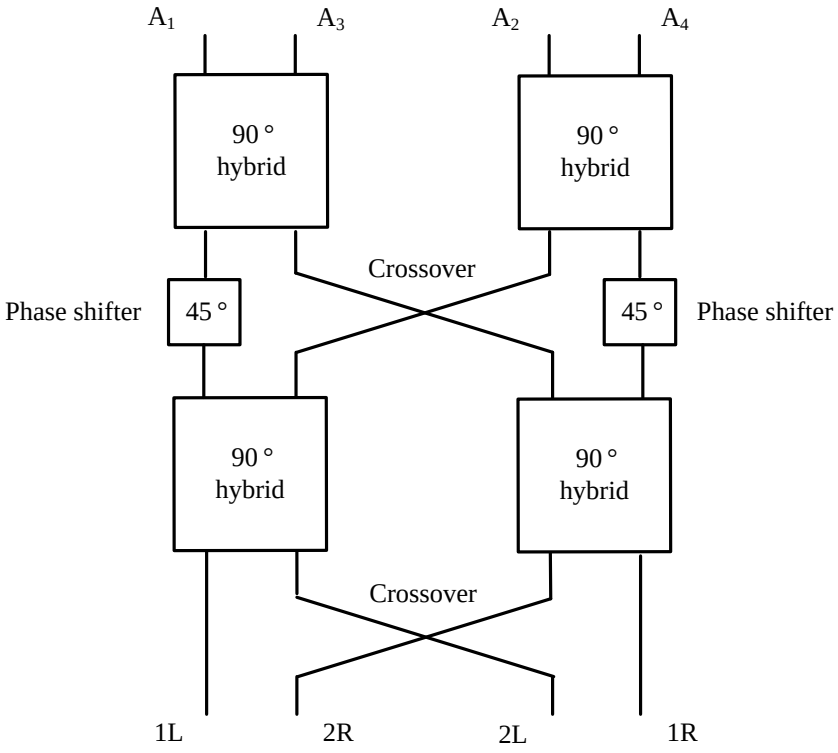

Figure 1.11: Schematic diagram of a 4×4 Butler matrix.

With reference to Figure 1.11, the Butler matrix splits the input power into 4 outputs with same amplitude but with linear phase taper. The phase taper is different for each input port. The outputs are linearly combinations of the inputs and can expressed as

$$1L = \frac{1}{4}(A_1\angle225^\circ + A_2\angle270^\circ + A_3\angle315^\circ + A_4\angle0^\circ) \tag{1.23}$$

$$2R = \frac{1}{4}(A_1\angle 270^\circ + A_2\angle 45^\circ + A_3\angle 180^\circ + A_4\angle 315^\circ) \tag{1.24}$$

$$2L = \frac{1}{4}(A_1\angle 315^\circ + A_2\angle 180^\circ + A_3\angle 45^\circ + A_4\angle 270^\circ) \tag{1.25}$$

$$1R = \frac{1}{4}(A_1\angle 0^\circ + A_2\angle 315^\circ + A_3\angle 270^\circ + A_4\angle 225^\circ) \tag{1.26}$$

Systematic design procedure for the Butler matrix is well explained in [16]. Because the Butler matrix is a passive reciprocal network, it works the same when it transmits energy as when it receives energy. Each beam can be used by a dedicated transmitter or receiver. Figure 1.12 shows a 4×4 Butler matrix used as a feed circuit for an antenna array.

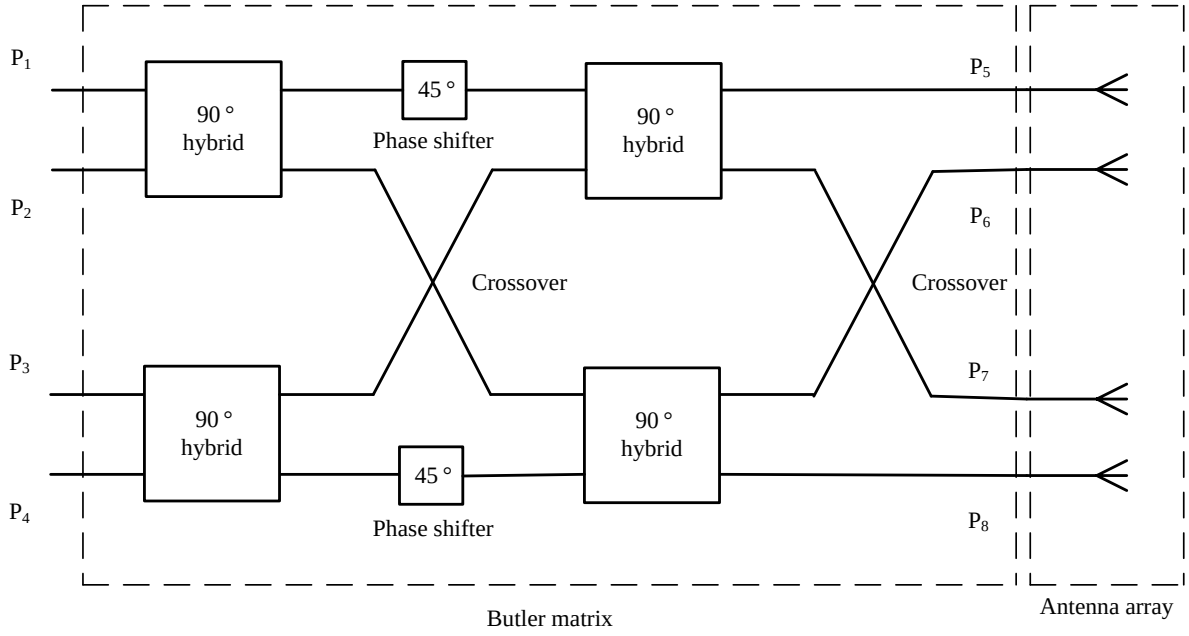

Figure 1.12: A 4×4 Butler matrix with antenna array.

1.5 Coupled resonator filters overview

Coupled resonator filters have been extensively studied in literature [17-20]. There is a general technique for the design of coupled resonator filters based on coupling coefficients of inter-coupled resonators and external quality factors of the input and output resonators. This design method can be applied to any type of resonator despite its physical structure [3].

1.5.1 General coupling matrix of two-port coupled resonator filters

The general coupling matrix is of importance for representing different coupled-resonator filter topologies. As presented in [3], the general coupling matrix can be derived either from a set of node equations or from a set of loop equations.

Figure 1.13 (a) shows the equivalent circuit for node equation formulation. As can be seen, all the resonators are electrically coupled together, thus a set of node equations can be formed. L_i, C_i and G_i denote the inductance, capacitance and conductance, respectively; i_s is the source current; and v_i represents the node voltage.

However, the couplings associated with the *n*-coupled resonators are based on mutual inductance in Figure 1.13 (b), where L_i, C_i and R_i denote the inductance, capacitance and resistance, respectively; e_s is the source voltage; and i_i represents the loop current. Hence we can obtain a set of loop equations.

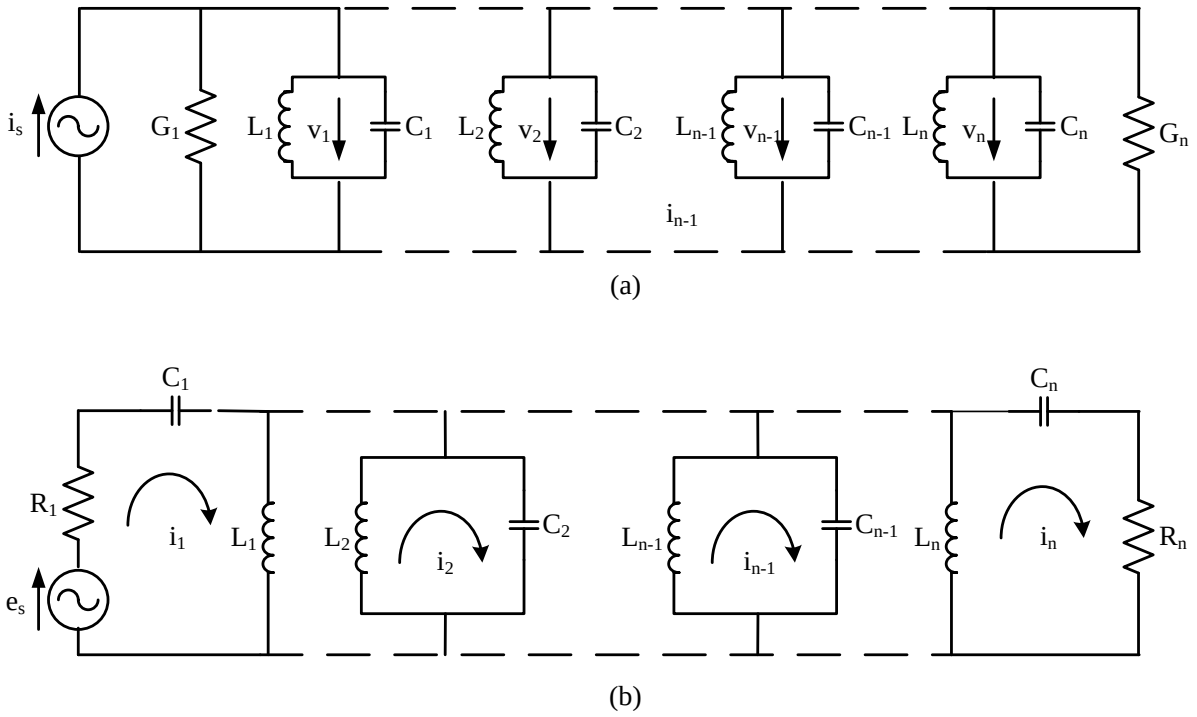

Figure 1.13: Equivalent circuits of *n*-coupled resonators for (a) node-equation formulation and (b) loop-equation formulation [3].

Regardless of the type of coupling, a general normalized matrix $[A]$ of a two-port *n*-coupled resonator filter are found as [3]

$$[A]=[q]+p[U]-j[m] \tag{1.27}$$

where $[q]$ is the general external quality factor matrix with all entries zero, except for $q_{11}=1/q_{e1}$ and $q_{nn}=1/q_{en}$, $p=j\dfrac{1}{FBW}(\dfrac{\omega}{\omega_0}-\dfrac{\omega_0}{\omega})$ is the complex lowpass frequency variable, $[U]$ is the $n\times n$ identity matrix, and $[m]$ is the general coupling matrix.

The transmission and reflection scattering parameters can be expressed in terms of the general normalized matrix $[A]$ as [3]

$$S_{11} = \pm(1 - \frac{1}{q_{e1}}[A]_{11}^{-1})$$
$$S_{21} = 2\frac{1}{\sqrt{q_{e1}q_{en}}}[A]_{n1}^{-1} \tag{1.28}$$

1.5.2 Filter synthesis in terms of coupling coefficients and external quality factors

Design formulations for Butterworth lowpass prototype filters and Chebyshev lowpass prototype filters have been presented in many reference books [21]. However, these equations are given in terms of the so called g value, which is the numerical value either of inductance in henries or of capacitance in farads. The coupling coefficients and the external quality factors for a coupled resonator bandpass filter with midband frequency of ω_0, lower passband edge of ω_l, and upper passband edge of ω_u can be obtained from the g values as [3]

$$M_{i,i+1} = \frac{FBW}{\sqrt{g_i g_{i+1}}}, \qquad for \quad i = 1, \quad 2, \quad \cdots \quad N-1 \tag{1.29}$$

$$Q_{e1} = \frac{g_0 g_1}{FBW} \tag{1.30}$$

$$Q_{eN} = \frac{g_N g_{N+1}}{FBW} \tag{1.31}$$

where FBW is the fractional bandwidth of the bandpass filter defined as

$$FBW = \frac{\omega_u - \omega_l}{\omega_0} \tag{1.32}$$

Chapter 2

Four-Port Coupled Resonator Circuits

In the previous chapter, we briefly described how coupled resonator filters are analyzed and synthesised in terms of coupling coefficients and external quality factors. However, this design technique can be extended to four-port coupled resonator circuits. In this chapter, we will derive the general coupling matrix representation for four-port *n*-coupled resonators. This formula provides the basis for this research work, and will be used in the synthesis of the coupled resonator hybrid couplers in Chapter 3. Analogous to the two-port resonator filter, the general coupling matrix can be formulated either from a set of loop equations or from a set of node equations [3].

2.1 Loop equation formulation

Figure 2.1 depicts an equivalent circuit of a lossless four-port n-coupled resonator circuit, where L_i, C_i and R_i denote the inductance, capacitance and resistance, respectively; e_s is the voltage source; and i_i represents the loop current. With reference to Figure 2.1, resonators 1, 2, *n-1*, *n* are connected to four ports, and a voltage source is connected to port 1. It is assumed that resonators are magnetically coupled together, and the magnetic couplings are represented by dash lines in Figure 2.1.

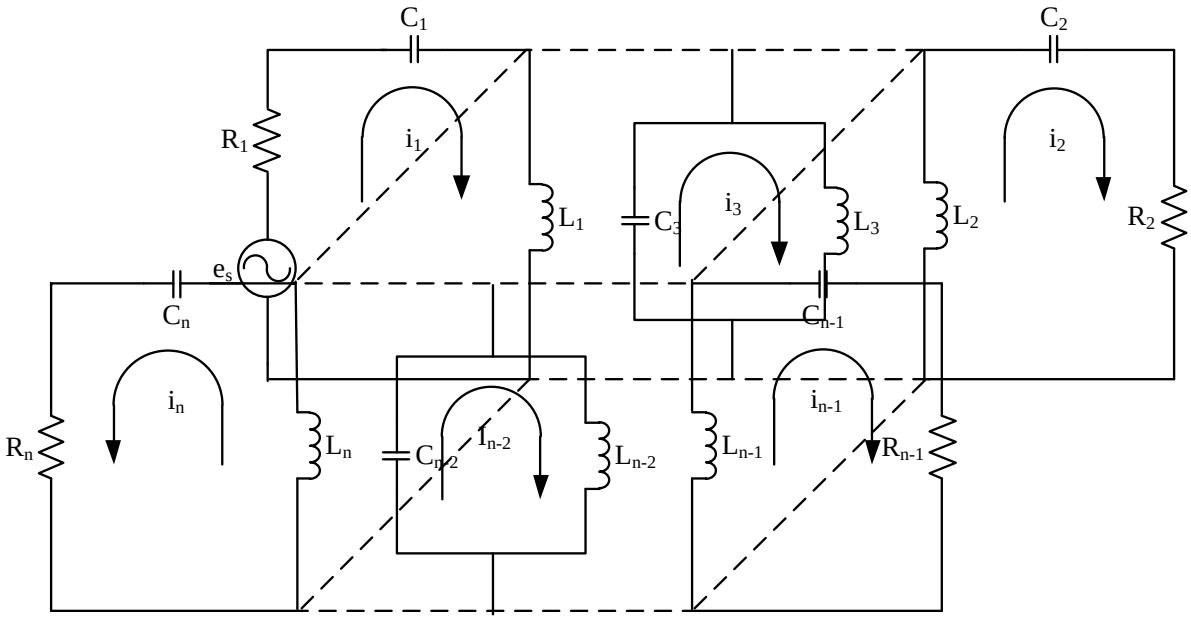

Figure 2.1: Equivalent circuit of four-port *n*-coupled resonators for loop equations [3].

According to voltage law, a set of loop equations for the circuit illustrated in Figure 2.1 can be obtained as

$$
\begin{aligned}
&(R_1 + j\omega L_1 + \frac{1}{j\omega C_1})i_1 - j\omega L_{12} i_2 \cdots \quad - j\omega L_{1(n-2)} i_{n-2} - j\omega L_{1(n-1)} i_{n-1} - j\omega L_{1n} i_n = e_s \\
&-j\omega L_{21} i_1 + (R_2 + j\omega L_2 + \frac{1}{j\omega C_2})i_2 \cdots \quad - j\omega L_{2(n-2)} i_{n-2} - j\omega L_{2(n-1)} i_{n-1} - j\omega L_{2n} i_n = 0 \\
&\qquad\qquad\qquad\qquad\qquad\qquad\qquad\qquad\qquad\qquad\qquad\qquad \vdots \\
&-j\omega L_{(n-2)1} i_1 - j\omega L_{(n-2)2} i_2 \cdots \quad + (j\omega L_{n-2} + \frac{1}{j\omega C_{n-2}})i_{n-2} - j\omega L_{(n-2)(n-1)} i_{n-1} - j\omega L_{(n-2)n} i_n = 0 \\
&-j\omega L_{(n-1)1} i_1 - j\omega L_{(n-1)2} i_2 \cdots \quad - j\omega L_{(n-1)(n-2)} i_{n-2} + (R_{n-1} + j\omega L_{n-1} + \frac{1}{j\omega C_{n-1}})i_{n-1} - j\omega L_{(n-1)n} i_n = 0 \\
&-j\omega L_{n1} i_1 - j\omega L_{n2} i_2 \cdots \quad - j\omega L_{n(n-2)} i_{n-2} - j\omega L_{n(n-1)} i_{n-1} + (R_n + j\omega L_n + \frac{1}{j\omega C_n})i_n = 0
\end{aligned}
\tag{2.1}
$$

where $L_{ij} = L_{ji}$ denotes the mutual inductance across resonators i and j.

Arrange this set of loop equations in matrix form

$$\begin{bmatrix} R_1 + j\omega L_1 + \frac{1}{j\omega C_1} & -j\omega L_{12} & \cdots & -j\omega L_{1(n-2)} & -j\omega L_{1(n-1)} & -j\omega L_{1n} \\ -j\omega L_{21} & (R_2 + j\omega L_2 + \frac{1}{j\omega C_2}) & \cdots & -j\omega L_{2(n-2)} & -j\omega L_{2(n-1)} & -j\omega L_{2n} \\ & & \vdots & & & \\ -j\omega L_{(n-2)1} & -j\omega L_{(n-2)2} & \cdots & (j\omega L_{(n-2)} + \frac{1}{j\omega C_{(n-2)}}) & -j\omega L_{(n-2)(n-1)} & -j\omega L_{(n-2)n} \\ -j\omega L_{(n-1)1} & -j\omega L_{(n-1)2} & \cdots & -j\omega L_{(n-1)(n-2)} & (R_{n-1} + j\omega L_{n-1} + \frac{1}{j\omega C_{n-1}}) & -j\omega L_{(n-1)n} \\ -j\omega L_{n1} & -j\omega L_{n2} & \cdots & -j\omega L_{n(n-2)} & -j\omega L_{n(n-1)} & (R_n + j\omega L_n + \frac{1}{j\omega C_n}) \end{bmatrix} \begin{bmatrix} i_1 \\ i_2 \\ \vdots \\ i_{n-2} \\ i_{n-1} \\ i_n \end{bmatrix} = \begin{bmatrix} e_s \\ 0 \\ \vdots \\ 0 \\ 0 \\ 0 \end{bmatrix}$$

or

$$[Z][i] = [v] \tag{2.2}$$

where $[Z]$ is an $n \times n$ impedance matrix.

For simplicity, let us consider all resonators resonate at the same frequency $\omega_0 = 1/\sqrt{LC}$, where $L = L_1 = L_2 \cdots = L_{n-2} = L_{n-1} = L_n$ and $C = C_1 = C_2 \cdots = C_{n-2} = C_{n-1} = C_n$. The impedance matrix in (2.2) may be expressed by

$$[Z] = \omega_0 L \cdot FBW \cdot [\overline{Z}] \tag{2.3}$$

where $FBW = \Delta\omega/\omega_0$ is the fractional bandwidth, and $[\overline{Z}]$ is the normalized impedance matrix. From (2.2) and (2.3), we obtain

$$\left[\bar{Z}\right]=\begin{bmatrix} \frac{R_1}{\omega_0 L\cdot FBW}+p & -j\frac{\omega}{\omega_0}\frac{L_{12}}{L}\frac{1}{FBW} & \cdots & -j\frac{\omega}{\omega_0}\frac{L_{1(n-2)}}{L}\frac{1}{FBW} & -j\frac{\omega}{\omega_0}\frac{L_{1(n-1)}}{L}\frac{1}{FBW} & -j\frac{\omega}{\omega_0}\frac{L_{1n}}{L}\frac{1}{FBW} \\ -j\frac{\omega}{\omega_0}\frac{L_{21}}{L}\frac{1}{FBW} & \frac{R_2}{\omega_0 L\cdot FBW}+p & \cdots & -j\frac{\omega}{\omega_0}\frac{L_{2(n-2)}}{L}\frac{1}{FBW} & -j\frac{\omega}{\omega_0}\frac{L_{2(n-1)}}{L}\frac{1}{FBW} & -j\frac{\omega}{\omega_0}\frac{L_{2n}}{L}\frac{1}{FBW} \\ & & \vdots & & & \\ -j\frac{\omega}{\omega_0}\frac{L_{(n-2)1}}{L}\frac{1}{FBW} & -j\frac{\omega}{\omega_0}\frac{L_{(n-2)2}}{L}\frac{1}{FBW} & \cdots & p & -j\frac{\omega}{\omega_0}\frac{L_{(n-2)(n-1)}}{L}\frac{1}{FBW} & -j\frac{\omega}{\omega_0}\frac{L_{(n-2)n}}{L}\frac{1}{FBW} \\ -j\frac{\omega}{\omega_0}\frac{L_{(n-1)1}}{L}\frac{1}{FBW} & -j\frac{\omega}{\omega_0}\frac{L_{(n-1)2}}{L}\frac{1}{FBW} & \cdots & -j\frac{\omega}{\omega_0}\frac{L_{(n-1)(n-2)}}{L}\frac{1}{FBW} & \frac{R_{n-1}}{\omega_0 L\cdot FBW}+p & -j\frac{\omega}{\omega_0}\frac{L_{(n-1)n}}{L}\frac{1}{FBW} \\ -j\frac{\omega}{\omega_0}\frac{L_{n1}}{L}\frac{1}{FBW} & -j\frac{\omega}{\omega_0}\frac{L_{n2}}{L}\frac{1}{FBW} & \cdots & -j\frac{\omega}{\omega_0}\frac{L_{n(n-2)}}{L}\frac{1}{FBW} & -j\frac{\omega}{\omega_0}\frac{L_{n(n-1)}}{L}\frac{1}{FBW} & \frac{R_n}{\omega_0 L\cdot FBW}+p \end{bmatrix} \quad (2.4)$$

with

$$p=j\frac{1}{FBW}\left(\frac{\omega}{\omega_0}-\frac{\omega_0}{\omega}\right) \quad (2.5)$$

Notice that

$$\frac{R_i}{\omega_0 L}=\frac{1}{Q_{ei}} \qquad for \quad i=1,\quad 2,\quad n-1,\quad n \quad (2.6)$$

where Q_{ei} is the external quality factor of the input or output resonator. Defining the coupling coefficient as

$$M_{ij}=\frac{L_{ij}}{L} \quad (2.7)$$

and assuming $\omega/\omega_0\approx 1$ for a narrow-band approximation, the impedance matrix in (2.4) can be simplified as

$$\left[\overline{Z}\right]=\begin{bmatrix} \frac{1}{q_{e1}}+p & -jm_{12} & \cdots & -jm_{1(n-2)} & -jm_{1(n-1)} & -jm_{1n} \\ -jm_{21} & \frac{1}{q_{e2}}+p & \cdots & -jm_{2(n-2)} & -jm_{2(n-1)} & -jm_{2n} \\ & & \vdots & & & \\ -jm_{(n-2)1} & -jm_{(n-2)2} & \cdots & p & -jm_{(n-2)(n-1)} & -jm_{(n-2)n} \\ -jm_{(n-1)1} & -jm_{(n-1)2} & \cdots & -jm_{(n-1)(n-2)} & \frac{1}{q_{e(n-1)}}+p & -jm_{(n-1)n} \\ -jm_{n1} & -jm_{n2} & \cdots & -jm_{n(n-2)} & -jm_{n(n-1)} & \frac{1}{q_{en}}+p \end{bmatrix} \tag{2.8}$$

where q_{ei} denotes the scaled external quality factor

$$q_{ei}=Q_{ei}\cdot FBW \qquad for \quad i=1,\quad 2,\quad n-1,\quad n \tag{2.9}$$

and m_{ij} represents the normalized coupling coefficient

$$m_{ij}=\frac{M_{ij}}{FBW} \tag{2.10}$$

To derive the scattering parameters of the four-port coupled-resonator circuit, the circuit in Figure 2.1 is represented by a four-port network as shown in Figure 2.2. The voltage and current variables at the ports are denoted by V_i and I_i, and a_i and b_i are the wave variables.

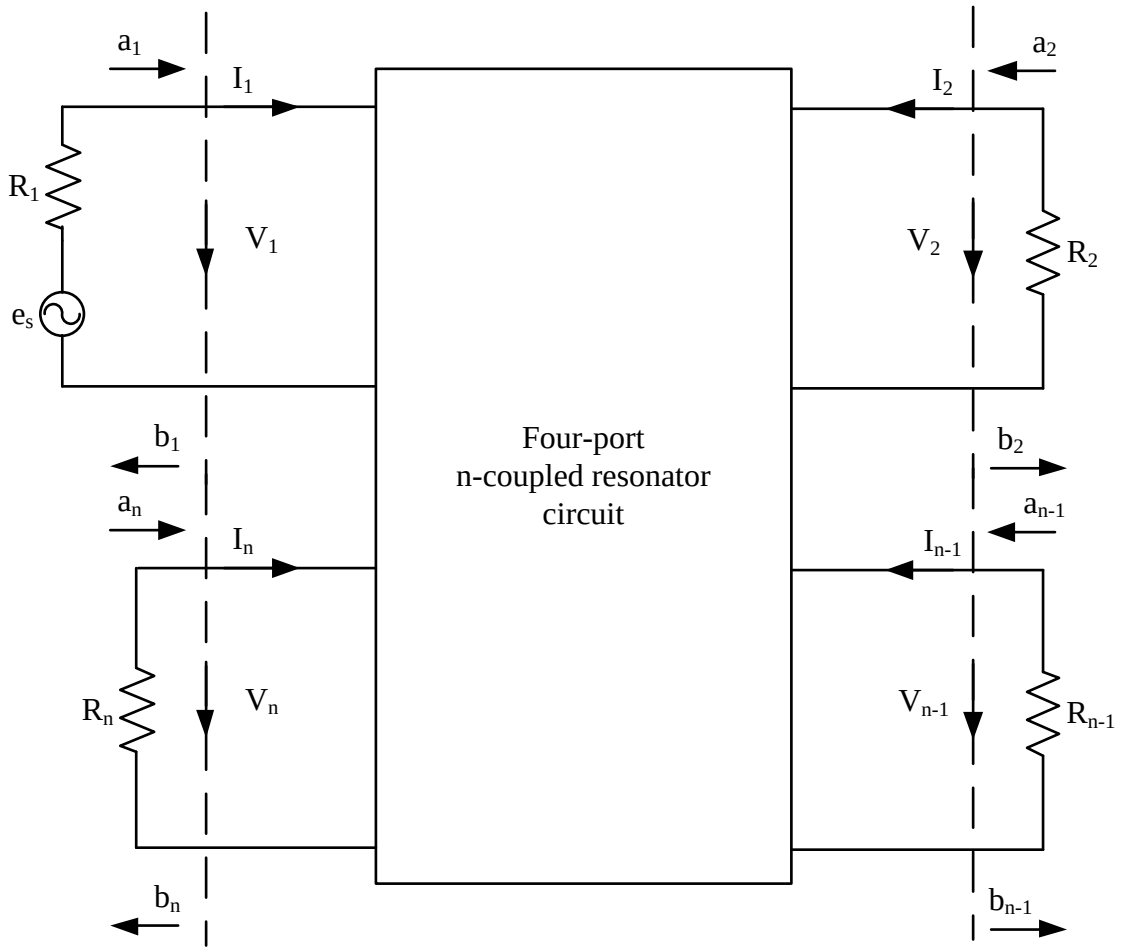

Figure 2.2: Network presentation of the circuit shown in Figure 2.1.

By inspecting Figure 2.1 and Figure 2.2, it can be found that $I_1 = i_1$, $I_2 = -i_2$, $I_{n-1} = -i_{n-1}$, $I_n = -i_n$, and $V_1 = e_s - i_1 R_1$, $V_2 = i_2 R_2$, $V_{n-1} = i_{n-1} R_{n-1}$, $V_n = i_n R_n$. With reference to [3], the relationships between the wave variables and the voltage and current variables are defined as

$$a_n = \frac{1}{2}(V_n \sqrt{Y_n} + \frac{I_n}{\sqrt{Y_n}})$$

$$b_n = \frac{1}{2}(V_n \sqrt{Y_n} - \frac{I_n}{\sqrt{Y_n}}) \qquad (2.11)$$

Hence the scattering parameters are calculated as

$$S_{11}=\frac{b_1}{a_1}\bigg|_{a_2=0,a_{n-1}=0,a_n=0}=1-\frac{2R_1 i_1}{e_s},\qquad S_{21}=\frac{b_2}{a_1}\bigg|_{a_2=0,a_{n-1}=0,a_n=0}=\frac{2\sqrt{R_1R_2}\,i_2}{e_s},$$

$$S_{(n-1)1}=\frac{b_{n-1}}{a_1}\bigg|_{a_2=0,a_{n-1}=0,a_n=0}=\frac{2\sqrt{R_1R_{n-1}}\,i_{n-1}}{e_s},\qquad S_{n1}=\frac{b_n}{a_1}\bigg|_{a_2=0,a_{n-1}=0,a_n=0}=\frac{2\sqrt{R_1R_n}\,i_n}{e_s} \tag{2.12}$$

By solving (2.2) and (2.3), the loop current i_i are found as

$$i_1=\frac{e_s}{\omega_0 L\cdot FBW}\left[\bar{Z}\right]^{-1}_{11}\qquad i_2=\frac{e_s}{\omega_0 L\cdot FBW}\left[\bar{Z}\right]^{-1}_{21}$$

$$i_{n-1}=\frac{e_s}{\omega_0 L\cdot FBW}\left[\bar{Z}\right]^{-1}_{(n-1)1}\qquad i_n=\frac{e_s}{\omega_0 L\cdot FBW}\left[\bar{Z}\right]^{-1}_{n1} \tag{2.13}$$

Substituting (2.13) into (2.12) yields

$$S_{11}=1-\frac{2R_1}{\omega_0 L\cdot FBW}\left[\bar{Z}\right]^{-1}_{11},\qquad S_{21}=\frac{2\sqrt{R_1R_2}}{\omega_0 L\cdot FBW}\left[\bar{Z}\right]^{-1}_{21},$$

$$S_{(n-1)1}=\frac{2\sqrt{R_1R_{n-1}}}{\omega_0 L\cdot FBW}\left[\bar{Z}\right]^{-1}_{(n-1)1},\qquad S_{n1}=\frac{2\sqrt{R_1R_n}}{\omega_0 L\cdot FBW}\left[\bar{Z}\right]^{-1}_{n1} \tag{2.14}$$

which can be simplified using (2.6) and (2.9) as

$$S_{11}=1-\frac{2}{q_{e1}}\left[\bar{Z}\right]^{-1}_{11},\qquad S_{21}=\frac{2}{\sqrt{q_{e1}q_{e2}}}\left[\bar{Z}\right]^{-1}_{21},$$

$$S_{(n-1)1}=\frac{2}{\sqrt{q_{e1}q_{e(n-1)}}}\left[\bar{Z}\right]^{-1}_{(n-1)1},\qquad S_{n1}=\frac{2}{\sqrt{q_{e1}q_{en}}}\left[\bar{Z}\right]^{-1}_{n1} \tag{2.15}$$

2.2 Node equation formulation

In this section, we will analyze four-port resonators with electric couplings. Figure 2.3 depicts the equivalent circuit of a lossless four-port *n*-coupled resonator circuit, where L_i, C_i and G_i denote the inductance, capacitance and conductance, respectively; i_s is the source current; and v_i represents the node voltage. With reference to Figure 2.3, resonators 1, 2, *n-1*, *n* are connected to four ports, and a voltage source is connected to port 1. The electric couplings are represented by dash lines in Figure 2.3.

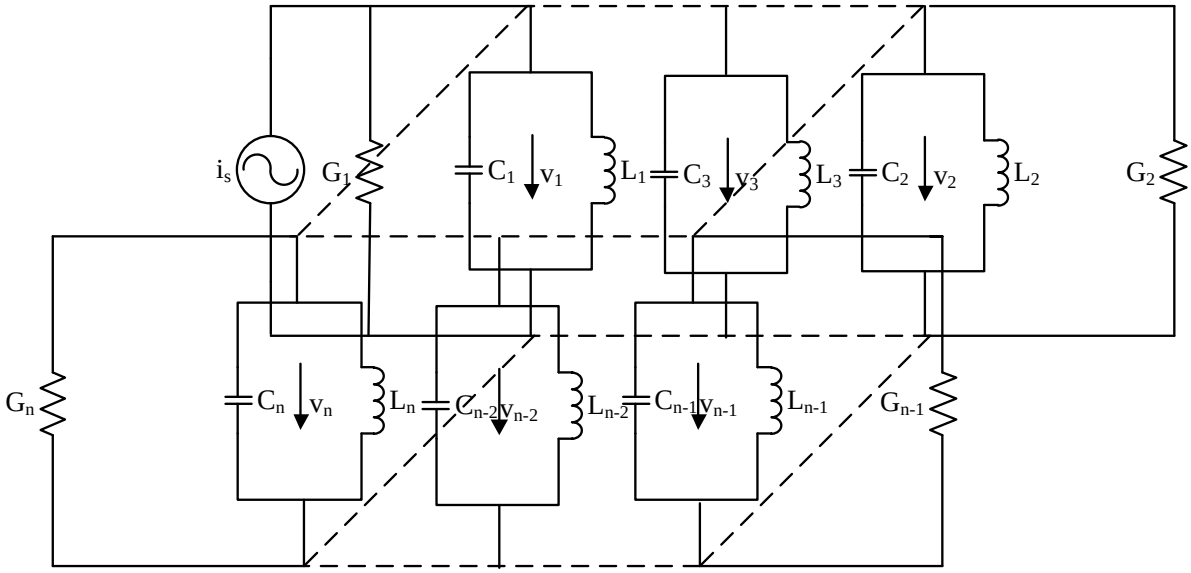

Figure 2.3: Equivalent circuit of four-port *n*-coupled resonators for node equations [3].

According to current law, a set of node equations for the circuit illustrated in Figure 2.3 can be obtained as

$$
\begin{aligned}
&(G_1 + j\omega C_1 + \frac{1}{j\omega L_1})v_1 - j\omega C_{12}v_2 \cdots \quad - j\omega C_{1(n-2)}v_{n-2} - j\omega C_{1(n-1)}v_{n-1} - j\omega C_{1n}v_n = i_s \\
&-j\omega C_{21}v_1 + (G_2 + j\omega C_2 + \frac{1}{j\omega L_2})v_2 \cdots \quad - j\omega C_{2(n-2)}v_{n-2} - j\omega C_{2(n-1)}v_{n-1} - j\omega C_{2n}v_n = 0 \\
&\qquad\qquad\qquad\qquad\qquad\qquad\qquad\qquad \vdots \\
&-j\omega C_{(n-2)1}v_1 - j\omega C_{(n-2)2}v_2 \cdots \quad + (j\omega C_{n-2} + \frac{1}{j\omega L_{n-2}})v_{n-2} - j\omega C_{(n-2)(n-1)}v_{n-1} - j\omega C_{(n-2)n}v_n = 0 \\
&-j\omega C_{(n-1)1}v_1 - j\omega C_{(n-1)2}v_2 \cdots \quad - j\omega C_{(n-1)(n-2)}v_{n-2} + (G_{n-1} + j\omega C_{n-1} + \frac{1}{j\omega L_{n-1}})v_{n-1} - j\omega C_{(n-1)n}v_n = 0 \\
&-j\omega C_{n1}v_1 - j\omega C_{n2}v_2 \cdots \quad - j\omega C_{n(n-2)}v_{n-2} - j\omega C_{n(n-1)}v_{n-1} + (G_n + j\omega C_n + \frac{1}{j\omega L_n})v_n = 0
\end{aligned}
\tag{2.16}
$$

where $C_{ij} = C_{ji}$ denotes the mutual capacitance across resonators i and j.

Arrange this set of node equations in matrix form

$$
\begin{bmatrix}
G_1 + j\omega C_1 + \frac{1}{j\omega L_1} & -j\omega C_{12} & \cdots & -j\omega C_{1(n-2)} & -j\omega C_{1(n-1)} & -j\omega C_{1n} \\
-j\omega C_{21} & G_2 + j\omega C_2 + \frac{1}{j\omega L_2} & \cdots & -j\omega C_{2(n-2)} & -j\omega C_{2(n-1)} & -j\omega C_{2n} \\
 & & \vdots & & & \\
-j\omega C_{(n-2)1} & -j\omega C_{(n-2)2} & \cdots & j\omega C_{n-2} + \frac{1}{j\omega L_{n-2}} & -j\omega C_{(n-2)(n-1)} & -j\omega C_{(n-2)n} \\
-j\omega C_{(n-1)1} & -j\omega C_{(n-1)2} & \cdots & -j\omega C_{(n-1)(n-2)} & G_{n-1} + j\omega C_{n-1} + \frac{1}{j\omega L_{n-1}} & -j\omega C_{(n-1)n} \\
-j\omega C_{n1} & -j\omega C_{n2} & \cdots & -j\omega C_{n(n-2)} & -j\omega C_{n(n-1)} & G_n + j\omega C_n + \frac{1}{j\omega L_n}
\end{bmatrix}
\begin{bmatrix} v_1 \\ v_2 \\ \vdots \\ v_{n-2} \\ v_{n-1} \\ v_n \end{bmatrix}
=
\begin{bmatrix} i_s \\ 0 \\ \vdots \\ 0 \\ 0 \\ 0 \end{bmatrix}
$$

or

$$
[Y][v] = [i] \tag{2.17}
$$

where $[Y]$ is an $n \times n$ admittance matrix.

Similarly, let us consider all resonators resonate at the same frequency $\omega_0 = 1/\sqrt{LC}$, where $L = L_1 = L_2 \cdots = L_{n-2} = L_{n-1} = L_n$ and $C = C_1 = C_2 \cdots = C_{n-2} = C_{n-1} = C_n$. The admittance matrix in (2.17) may be expressed by

$$[Y] = \omega_0 L \cdot FBW \cdot \left[\overline{Y}\right] \tag{2.18}$$

where $FBW = \Delta\omega/\omega_0$ is the fractional bandwidth, and $\left[\overline{Y}\right]$ is the normalized admittance matrix. From (2.17) and (2.18), we obtain

$$\left[\overline{Y}\right] = \begin{bmatrix} \frac{G_1}{\omega_0 C \cdot FBW} + p & -j\frac{\omega}{\omega_0}\frac{C_{12}}{C}\frac{1}{FBW} & \cdots & -j\frac{\omega}{\omega_0}\frac{C_{1(n-2)}}{C}\frac{1}{FBW} & -j\frac{\omega}{\omega_0}\frac{C_{1(n-1)}}{C}\frac{1}{FBW} & -j\frac{\omega}{\omega_0}\frac{C_{1n}}{C}\frac{1}{FBW} \\ -j\frac{\omega}{\omega_0}\frac{C_{21}}{C}\frac{1}{FBW} & \frac{G_2}{\omega_0 C \cdot FBW} + p & \cdots & -j\frac{\omega}{\omega_0}\frac{C_{2(n-2)}}{C}\frac{1}{FBW} & -j\frac{\omega}{\omega_0}\frac{C_{2(n-1)}}{C}\frac{1}{FBW} & -j\frac{\omega}{\omega_0}\frac{C_{2n}}{C}\frac{1}{FBW} \\ & & \vdots & & & \\ -j\frac{\omega}{\omega_0}\frac{C_{(n-2)1}}{C}\frac{1}{FBW} & -j\frac{\omega}{\omega_0}\frac{C_{(n-2)2}}{C}\frac{1}{FBW} & \cdots & p & -j\frac{\omega}{\omega_0}\frac{C_{(n-2)(n-1)}}{C}\frac{1}{FBW} & -j\frac{\omega}{\omega_0}\frac{C_{(n-2)n}}{C}\frac{1}{FBW} \\ -j\frac{\omega}{\omega_0}\frac{C_{(n-1)1}}{C}\frac{1}{FBW} & -j\frac{\omega}{\omega_0}\frac{C_{(n-1)2}}{C}\frac{1}{FBW} & \cdots & -j\frac{\omega}{\omega_0}\frac{C_{(n-1)(n-2)}}{C}\frac{1}{FBW} & \frac{G_{n-1}}{\omega_0 C \cdot FBW} + p & -j\frac{\omega}{\omega_0}\frac{C_{(n-1)n}}{C}\frac{1}{FBW} \\ -j\frac{\omega}{\omega_0}\frac{C_{n1}}{C}\frac{1}{FBW} & -j\frac{\omega}{\omega_0}\frac{C_{n2}}{C}\frac{1}{FBW} & \cdots & -j\frac{\omega}{\omega_0}\frac{C_{n(n-2)}}{C}\frac{1}{FBW} & -j\frac{\omega}{\omega_0}\frac{C_{n(n-1)}}{C}\frac{1}{FBW} & \frac{G_n}{\omega_0 C \cdot FBW} + p \end{bmatrix} \tag{2.19}$$

with

$$p = j\frac{1}{FBW}\left(\frac{\omega}{\omega_0} - \frac{\omega_0}{\omega}\right) \tag{2.20}$$

Notice that

$$\frac{G_i}{\omega_0 C} = \frac{1}{Q_{ei}} \qquad for \quad i = 1, \quad 2, \quad n-1, \quad n \tag{2.21}$$

where Q_{ei} is the external quality factor of the input or output resonator. Defining the coupling coefficient as

$$M_{ij} = \frac{C_{ij}}{C} \tag{2.22}$$

and assuming $\omega/\omega_0 \approx 1$ for a narrow-band approximation, the admittance matrix in (2.19) can be simplified as

$$\left[\overline{Y}\right] = \begin{bmatrix} \frac{1}{q_{e1}} + p & -jm_{12} & \cdots & -jm_{1(n-2)} & -jm_{1(n-1)} & -jm_{1n} \\ -jm_{21} & \frac{1}{q_{e2}} + p & \cdots & -jm_{2(n-2)} & -jm_{2(n-1)} & -jm_{2n} \\ & & \vdots & & & \\ -jm_{(n-2)1} & -jm_{(n-2)2} & \cdots & p & -jm_{(n-2)(n-1)} & -jm_{(n-2)n} \\ -jm_{(n-1)1} & -jm_{(n-1)2} & \cdots & -jm_{(n-1)(n-2)} & \frac{1}{q_{e(n-1)}} + p & -jm_{(n-1)n} \\ -jm_{n1} & -jm_{n2} & \cdots & -jm_{n(n-2)} & -jm_{n(n-1)} & \frac{1}{q_{en}} + p \end{bmatrix} \tag{2.23}$$

where q_{ei} denotes the scaled external quality factor

$$q_{ei} = Q_{ei} \cdot FBW \qquad for \quad i = 1, \quad 2, \quad n-1, \quad n \tag{2.24}$$

and m_{ij} represents the normalized coupling coefficient

$$m_{ij} = \frac{M_{ij}}{FBW} \tag{2.25}$$

Similarly the circuit in Figure 2.3 can be represented by a four-port network as shown in Figure 2.4. The voltage and current variables at the ports are denoted by V_i and I_i, and a_i and b_i are the wave variables.

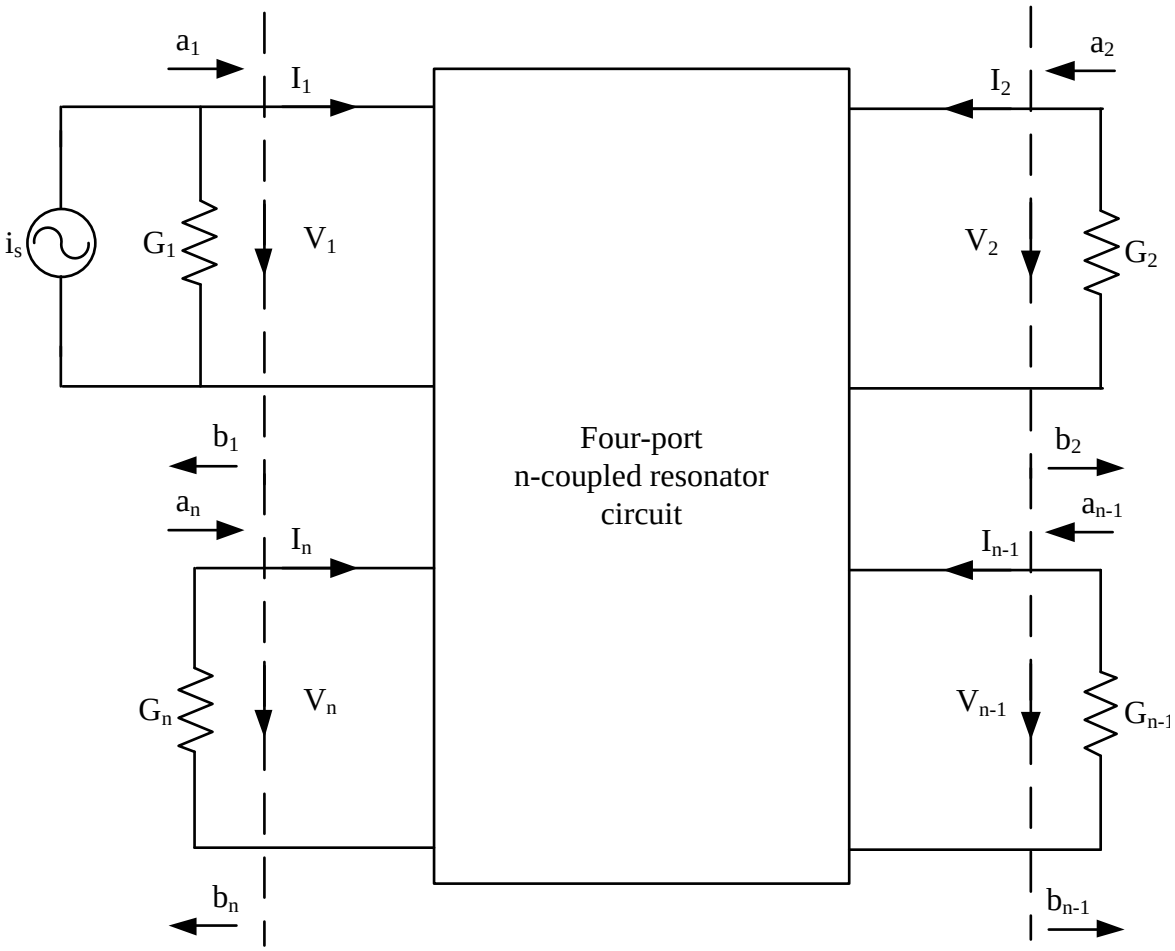

Figure 2.4: Network representation of a four-port *n*-coupled resonator circuit.

By inspecting Figure 2.3 and Figure 2.4, it can be found that $V_1 = v_1$, $V_2 = v_2$, $V_{n-1} = v_{n-1}$, $V_n = v_n$ and $I_1 = i_s - v_1 G_1$, $I_2 = -v_2 G_2$, $I_{n-1} = -v_{n-1} G_{n-1}$, $I_n = -v_n G_n$. Using (2.11), the scattering parameters can be calculated as

$$S_{11} = \left.\frac{b_1}{a_1}\right|_{a_2=0, a_{n-1}=0, a_n=0} = \frac{2v_1 G_1}{i_s} - 1, \qquad S_{21} = \left.\frac{b_2}{a_1}\right|_{a_2=0, a_{n-1}=0, a_n=0} = \frac{2v_2\sqrt{G_1 G_2}}{i_s},$$

$$S_{(n-1)1} = \left.\frac{b_{n-1}}{a_1}\right|_{a_2=0, a_{n-1}=0, a_n=0} = \frac{2v_{n-1}\sqrt{G_1 G_{n-1}}}{i_s}, \qquad S_{n1} = \left.\frac{b_n}{a_1}\right|_{a_2=0, a_{n-1}=0, a_n=0} = \frac{2v_n\sqrt{G_1 G_n}}{i_s} \tag{2.26}$$

The node voltages v_i can be calculated from (2.17) and (2.18)

$$v_1 = \frac{i_s}{\omega_0 C \cdot FBW}\left[\bar{Y}\right]_{11}^{-1} \qquad v_2 = \frac{i_s}{\omega_0 C \cdot FBW}\left[\bar{Y}\right]_{21}^{-1}$$
$$v_{n-1} = \frac{i_s}{\omega_0 C \cdot FBW}\left[\bar{Y}\right]_{(n-1)1}^{-1} \qquad v_n = \frac{i_s}{\omega_0 C \cdot FBW}\left[\bar{Y}\right]_{n1}^{-1} \tag{2.27}$$

Replacing the node voltages in (2.26) with those given by (2.27) results in

$$S_{11} = \frac{2G_1}{\omega_0 C \cdot FBW}\left[\bar{Y}\right]_{11}^{-1} - 1 \qquad S_{21} = \frac{2\sqrt{G_1 G_2}}{\omega_0 C \cdot FBW}\left[\bar{Y}\right]_{21}^{-1}$$
$$S_{(n-1)1} = \frac{2\sqrt{G_1 G_{n-1}}}{\omega_0 C \cdot FBW}\left[\bar{Y}\right]_{(n-1)1}^{-1} \qquad S_{n1} = \frac{2\sqrt{G_1 G_n}}{\omega_0 C \cdot FBW}\left[\bar{Y}\right]_{n1}^{-1} \tag{2.28}$$

which can be simplified using (2.21) and (2.24) as

$$S_{11} = \frac{2}{q_{e1}}\left[\bar{Y}\right]_{11}^{-1} - 1, \qquad S_{21} = \frac{2}{\sqrt{q_{e1} q_{e2}}}\left[\bar{Y}\right]_{21}^{-1},$$
$$S_{(n-1)1} = \frac{2}{\sqrt{q_{e1} q_{e(n-1)}}}\left[\bar{Y}\right]_{(n-1)1}^{-1}, \qquad S_{n1} = \frac{2}{\sqrt{q_{e1} q_{en}}}\left[\bar{Y}\right]_{n1}^{-1} \tag{2.29}$$

2.3 General coupling matrix

From the previous sections, we note that the formulation of the normalized impedance matrix in (2.8) is identical to that of the normalized admittance matrix in (2.23). So we would have a general formulation for four-port *n*-coupled resonators regardless of whether the coupling is magnetic or electric. The scattering parameters of four-port *n*-coupled resonators may be generalized from (2.15) and (2.29) as [22]

$$S_{11} = \pm(1 - \frac{2}{q_{e1}}[A]_{11}^{-1})$$

$$S_{21} = \frac{2}{\sqrt{q_{e1}q_{e2}}}[A]_{21}^{-1}$$

$$S_{(n-1)1} = \frac{2}{\sqrt{q_{e1}q_{e(n-1)}}}[A]_{(n-1)1}^{-1} \tag{2.30}$$

$$S_{n1} = \frac{2}{\sqrt{q_{e1}q_{en}}}[A]_{n1}^{-1}$$

with

$$[A] = [q] + p[U] - j[m] \tag{2.31}$$

where $[q]$ is the $n \times n$ matrix with all entries zero, except for $q_{11} = 1/q_{e1}$, $q_{22} = 1/q_{e2}$, $q_{(n-1)(n-1)} = 1/q_{e(n-1)}$, $q_{nn} = 1/q_{en}$, $[U]$ is the $n \times n$ identity matrix, and $[m]$ is the general coupling matrix.

The general matrix $[A]$ derived here is of importance for representing different four-port coupled resonator circuit topologies. The formulations in (2.30) and (2.31) will be employed in the synthesis of coupled resonator hybrid couplers in the next chapter.

Chapter 3

Synthesis of coupled resonator hybrid couplers

Hybrid couplers are passive microwave devices used to evenly divide the input signal into two signals of less power, and are used in many practical circuits such as balanced mixers [23], amplifiers and so forth. There are many available designs and configurations for hybrid couplers, including branch-line hybrid couplers and rat-race hybrid couplers [24-27]. In this chapter, an approach to design coupled resonator hybrid couplers is proposed. We first discuss some general properties of the conventional branch-line hybrid coupler, and then synthesize a coupled resonator $90°$ hybrid coupler from the equivalent circuit of the branch-line hybrid. The equations of the scattering parameters in terms of the general coupling matrix, derived in the previous chapter, will be used. Calculations of coupling coefficients and external quality factors are illustrated. Numerical examples of coupled resonator $90°$ hybrids, the simplest form and the one with an improved performance, will also be given. Finally the analysis and design of the coupled resonator $180°$ hybrid coupler are treated in a similar manner.

3.1 Conventional branch-line hybrid coupler

The branch-line hybrid coupler [28] shown in Figure 3.1 can easily be constructed in planar (microstrip or stripline) form. As illustrated in Figure 3.1, the branch-line hybrid has four ports with the terminal impedance Z_0. It consists of two quarter-wavelength transmission line sections of characteristic impedance Z_{01}. The two transmission line sections are connected by two shunt branches, which are both quarter-wavelength transmission line sections of characteristic impedance Z_{02}, at both ends. With reference to Figure 3.1, a signal applied to

port 1 will be evenly split into two components with a 90 ° phase difference at ports 2 and 3, and port 4 will be isolated. Observe that the branch-line hybrid is symmetrical, so any port can be used as the input port.

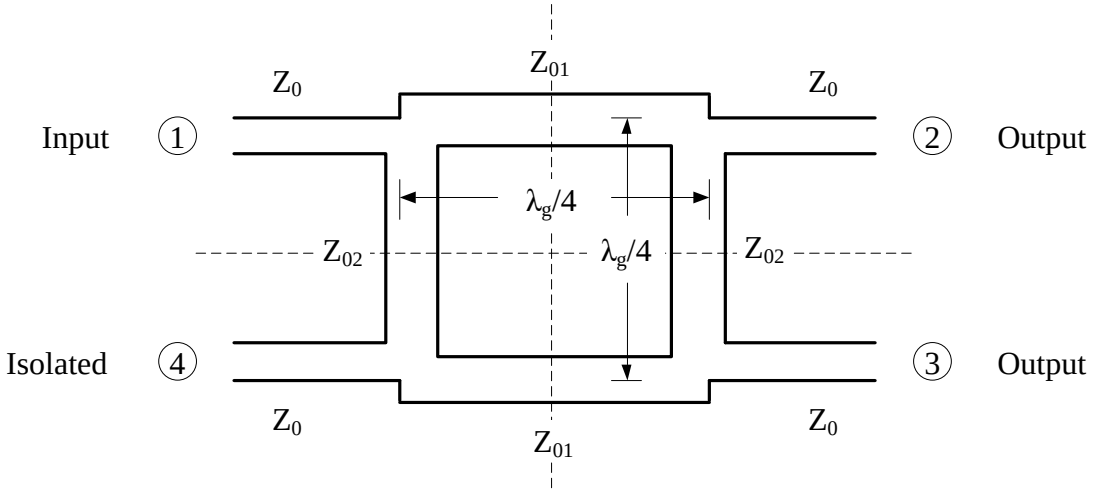

Figure 3.1: Geometry of a branch-line hybrid coupler [9].

3.1.1 Design of a branch-line hybrid coupler

At the centre frequency, scattering parameters of the branch-line hybrid are given by [29]

$$S_{21} = -j\frac{Z_{01}}{Z_0} \tag{3.1}$$

$$S_{31} = -\frac{Z_{01}}{Z_{02}} \tag{3.2}$$

$$S_{11} = S_{41} = 0 \tag{3.3}$$

Thus the complete scattering matrix can be expressed as

$$[S]=\begin{bmatrix} 0 & -j\frac{Z_{01}}{Z_0} & -\frac{Z_{01}}{Z_{02}} & 0 \\ -j\frac{Z_{01}}{Z_0} & 0 & 0 & -\frac{Z_{01}}{Z_{02}} \\ -\frac{Z_{01}}{Z_{02}} & 0 & 0 & -j\frac{Z_{01}}{Z_0} \\ 0 & -\frac{Z_{01}}{Z_{02}} & -j\frac{Z_{01}}{Z_0} & 0 \end{bmatrix} \tag{3.4}$$

From (1.18) and (3.4), we have

$$Z_{01} = Z_0 C_1 \tag{3.5}$$

$$Z_{02} = \frac{Z_{01}}{C_2} \tag{3.6}$$

Then using (1.20) in (3.5) and (3.6) gives

$$Z_{01} = \frac{1}{\sqrt{2}} Z_0 \tag{3.7}$$

$$Z_{02} = Z_0 \tag{3.8}$$

3.1.2 Performance of a branch-line hybrid coupler

The analysis of the branch-line hybrid can be carried out using the even- and odd-mode approach [30]. As shown in Figure 3.2, we first draw the schematic circuit of branch-line coupler in normalized form, where each line represents a transmission line with the characteristic impedance normalized to Z_0. We then assume that a wave of unit amplitude $A_1 = 1$ is incident at port 1.

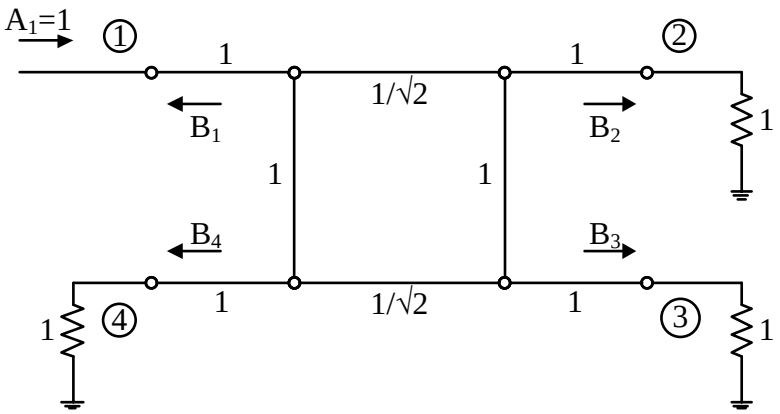

Figure 3.2: Schematic circuit of the normalized branch-line coupler [9].

The circuit of Figure 3.2 can be decomposed into the superposition of an even-mode excitation and an odd-mode excitation, as shown in Figure 3.3.

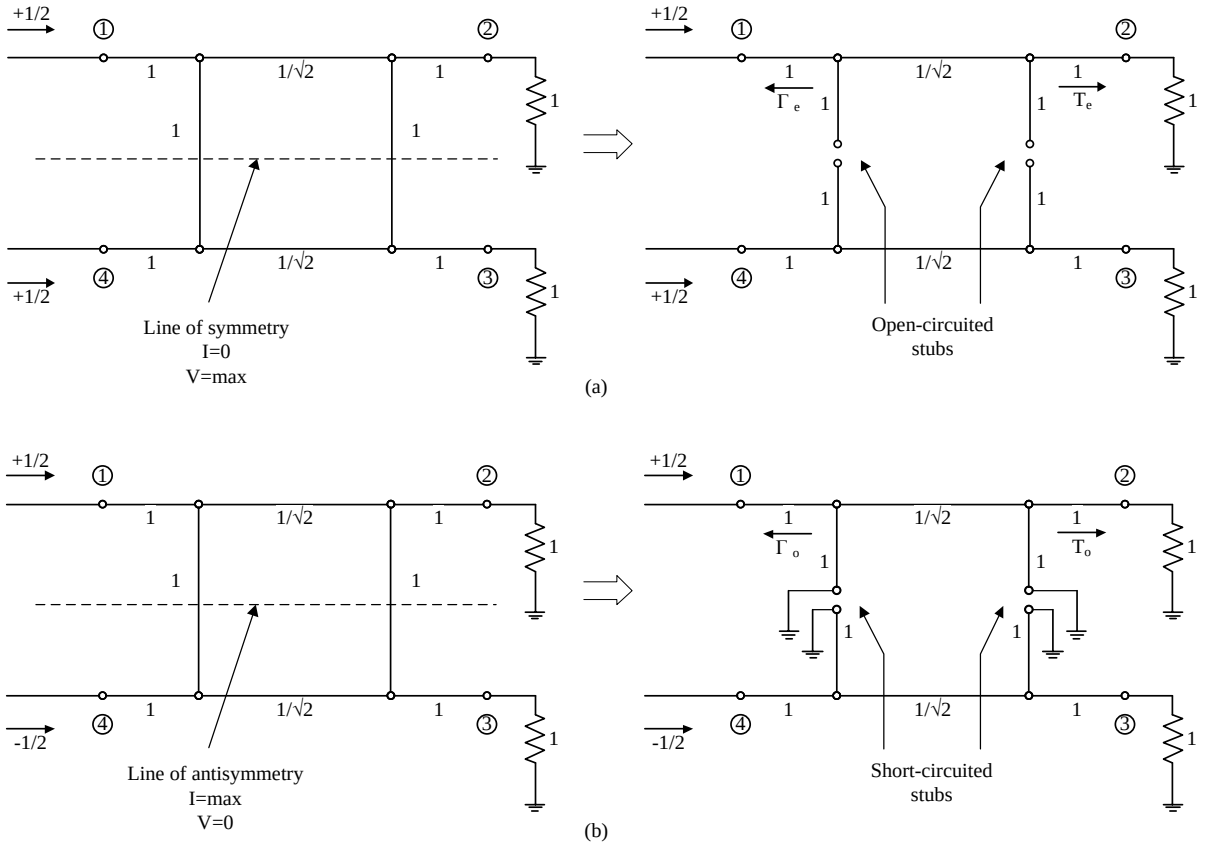

Figure 3.3: (a) Even-mode excitation and (b) Odd-mode excitation [9].

Because the circuit is linear, the actual response of Figure 3.2 can be obtained from the sum of the responses to the even-mode and odd-mode excitations. The amplitude of the emerging wave at each port of the branch-line hybrid coupler can be expressed as

$$B_1 = \frac{1}{2}\Gamma_e + \frac{1}{2}\Gamma_o \tag{3.9}$$

$$B_2 = \frac{1}{2}T_e + \frac{1}{2}T_o \tag{3.10}$$

$$B_3 = \frac{1}{2}T_e - \frac{1}{2}T_o \tag{3.11}$$

$$B_4 = \frac{1}{2}\Gamma_e - \frac{1}{2}\Gamma_o \tag{3.12}$$

where $T_{e,o}$ and $\Gamma_{e,o}$ are the even- and odd- mode transmission and reflection coefficients for the two port networks of Figure 3.3.

For the even-mode two-port circuit shown in Figure 3.3 (a), T_e and Γ_e can be calculated from multiplying the *ABCD* matrices of each cascade component in the circuit. Assume the branch-line hybrid coupler has a centre frequency of f_o, which implies that each branch has the length

$$l = \frac{\lambda_0}{4} = \frac{c/f_0}{4} = \frac{\pi c}{2\omega_0} \tag{3.13}$$

where λ_0 and ω_0 are the wavelength and radian frequency corresponding to the centre frequency f_o, respectively.

With reference to [9], the *ABCD* matrix of a transmission line section of length *l* and characteristic impedance Z_c can be expressed as

$$\begin{bmatrix} A & B \\ C & D \end{bmatrix} = \begin{bmatrix} \cos\beta l & jZ_c \sin\beta l \\ jY_c \sin\beta l & \cos\beta l \end{bmatrix} \tag{3.14}$$

where $\beta = \omega/c$ is the phase constant. Substituting the impedance of Figure 3.2 into (3.14) gives the *ABCD* matrix of the main branch as

$$\begin{bmatrix} A & B \\ C & D \end{bmatrix} = \begin{bmatrix} \cos\dfrac{\omega}{\omega_0}\dfrac{\pi}{2} & j\dfrac{1}{\sqrt{2}}\sin\dfrac{\omega}{\omega_0}\dfrac{\pi}{2} \\ j\sqrt{2}\sin\dfrac{\omega}{\omega_0}\dfrac{\pi}{2} & \cos\dfrac{\omega}{\omega_0}\dfrac{\pi}{2} \end{bmatrix} \tag{3.15}$$

However, for the open-circuited stub, the impedance is given as

$$Z_{oc} = -jZ_c \cot\beta l \tag{3.16}$$

where the length of each stub is $l = \dfrac{\lambda_0}{8} = \dfrac{\pi}{4}\dfrac{\omega}{\omega_0}$.

The *ABCD* matrix of the shunt open-circuited stub can be obtained as

$$\begin{bmatrix} A & B \\ C & D \end{bmatrix} = \begin{bmatrix} 1 & 0 \\ j\tan\dfrac{\omega}{\omega_0}\dfrac{\pi}{4} & 1 \end{bmatrix} \tag{3.17}$$

Thus for the two-port even-mode excitation, the *ABCD* matrix is found as

$$\begin{bmatrix} A & B \\ C & D \end{bmatrix}_e = \begin{bmatrix} 1 & 0 \\ j\tan\dfrac{\omega}{\omega_0}\dfrac{\pi}{4} & 1 \end{bmatrix} \begin{bmatrix} \cos\dfrac{\omega}{\omega_0}\dfrac{\pi}{2} & j\dfrac{1}{\sqrt{2}}\sin\dfrac{\omega}{\omega_0}\dfrac{\pi}{2} \\ j\sqrt{2}\sin\dfrac{\omega}{\omega_0}\dfrac{\pi}{2} & \cos\dfrac{\omega}{\omega_0}\dfrac{\pi}{2} \end{bmatrix} \begin{bmatrix} 1 & 0 \\ j\tan\dfrac{\omega}{\omega_0}\dfrac{\pi}{4} & 1 \end{bmatrix} \tag{3.18}$$

The transmission and reflection coefficients can be converted from the *ABCD* matrix [9] as

$$T_e = \frac{2}{A+B+C+D} \tag{3.19}$$

$$\Gamma_e = \frac{A+B-C-D}{A+B+C+D} \tag{3.20}$$

Similarly, for the odd-mode excitation, we obtain the *ABCD* matrix for the two port network

$$\begin{bmatrix} A & B \\ C & D \end{bmatrix}_o = \begin{bmatrix} 1 & 0 \\ -j\cot\frac{\omega}{\omega_0}\frac{\pi}{4} & 1 \end{bmatrix} \begin{bmatrix} \cos\frac{\omega}{\omega_0}\frac{\pi}{2} & j\frac{1}{\sqrt{2}}\sin\frac{\omega}{\omega_0}\frac{\pi}{2} \\ j\sqrt{2}\sin\frac{\omega}{\omega_0}\frac{\pi}{2} & \cos\frac{\omega}{\omega_0}\frac{\pi}{2} \end{bmatrix} \begin{bmatrix} 1 & 0 \\ -j\cot\frac{\omega}{\omega_0}\frac{\pi}{4} & 1 \end{bmatrix} \tag{3.21}$$

which gives the transmission and reflection coefficients as

$$T_o = \frac{2}{A+B+C+D} \tag{3.22}$$

$$\Gamma_o = \frac{A+B-C-D}{A+B+C+D} \tag{3.23}$$

Then the scattering parameters of the branch-line hybrid coupler are obtained as

$$S_{11} = \frac{B_1}{A_1} = B_1 = \frac{1}{2}\left(\Gamma_e + \Gamma_o\right) \tag{3.24}$$

$$S_{21} = \frac{B_2}{A_1} = B_2 = \frac{1}{2}\left(T_e + T_o\right) \tag{3.25}$$

$$S_{31} = \frac{B_3}{A_1} = B_3 = \frac{1}{2}\left(T_e - T_o\right) \tag{3.26}$$

$$S_{41} = \frac{B_4}{A_1} = B_4 = \frac{1}{2}\left(\Gamma_e - \Gamma_o\right) \tag{3.27}$$

with the amplitude of the incident wave $A_1 = 1$.

The calculated frequency responses are plotted in Figure 3.4 and Figure 3.5.

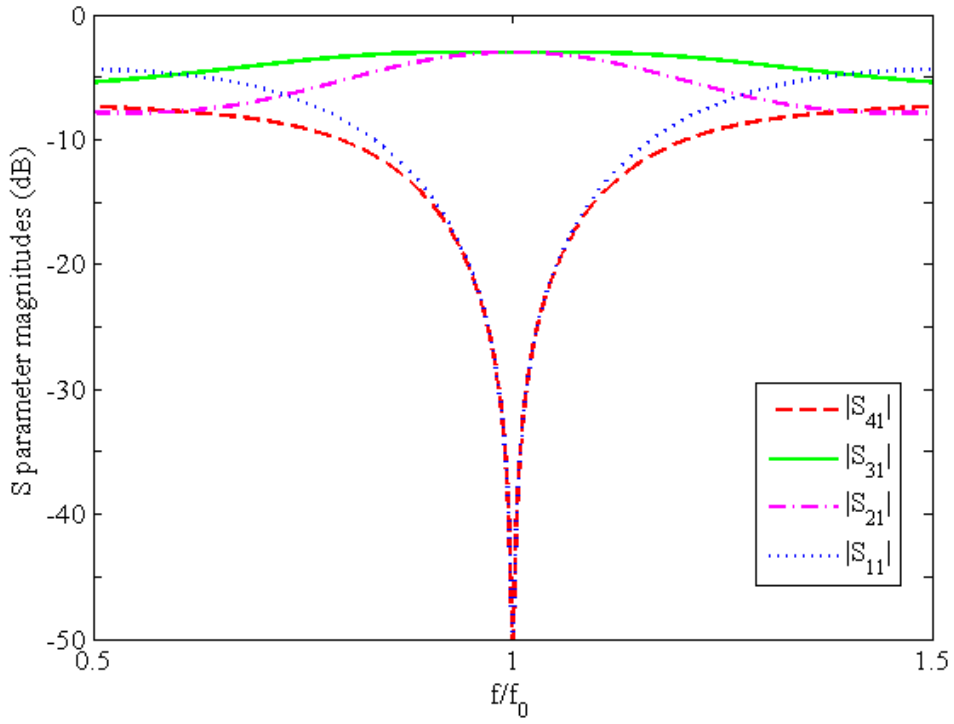

Figure 3.4: S parameter magnitudes versus frequency for branch-line hybrid coupler.

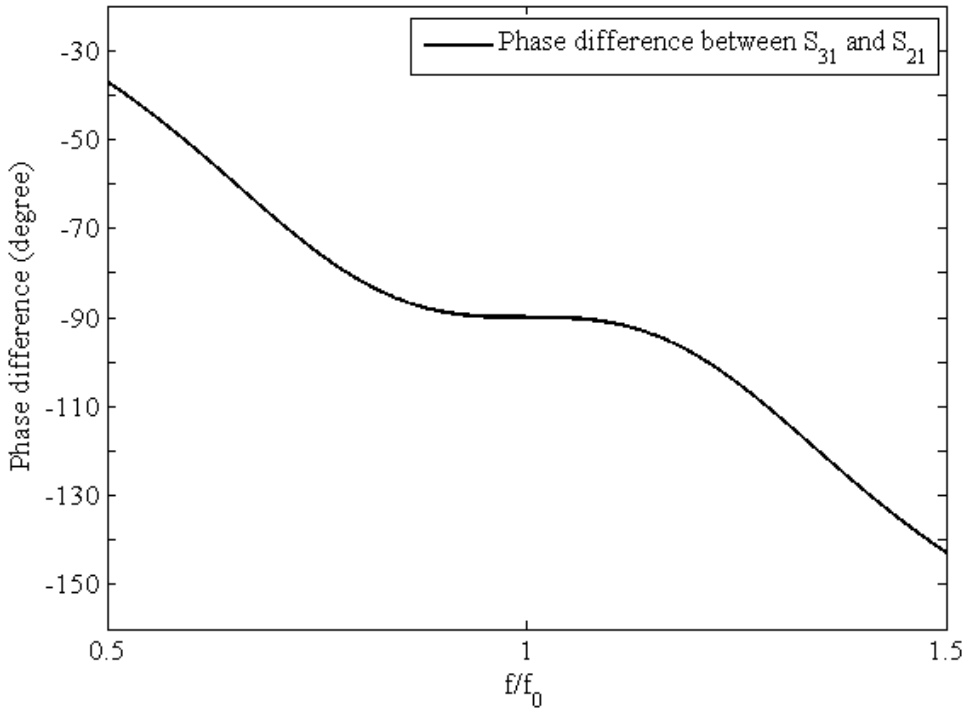

Figure 3.5: Phase difference between two outputs for branch-line hybrid coupler.

At the design frequency f_0, we obtain perfect 3dB power division in ports 2 and 3, perfect isolation and return loss in ports 4 and 1, and perfect 90 °phase difference between ports 3 and 2. However, all of these quantities degrade quickly as the frequency departs from f_0.

3.1.3 Equivalent circuit of a conventional branch-line hybrid coupler

A branch-line hybrid coupler as shown in Figure 3.1 consists of four quarter-wavelength transmission line sections. Each quarter-wavelength transmission line section can be expressed by its equivalent lumped elements as shown in Figure 3.6.

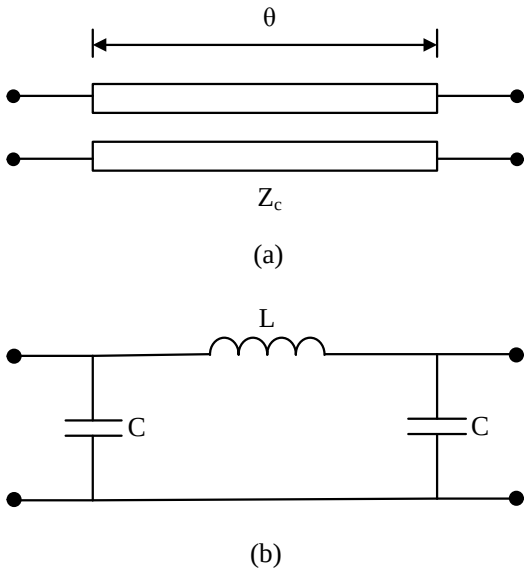

Figure 3.6: (a) A transmission line section and (b) its lumped element equivalent.

The values of the lumped elements can be obtained by equating the ABCD matrix parameters for both structures. For a lossless transmission line section of characteristic impedance Z_c and electrical length θ, the ABCD matrix is given by [9]

$$\begin{bmatrix} A & B \\ C & D \end{bmatrix} = \begin{bmatrix} \cos\theta & jZ_c \sin\theta \\ j\dfrac{\sin\theta}{Z_c} & \cos\theta \end{bmatrix} \tag{3.28}$$

The ABCD matrix of a π lumped-element network as shown in Figure 3.6 (b) is given by

$$\begin{bmatrix} A & B \\ C & D \end{bmatrix} = \begin{bmatrix} 1 & 0 \\ j\omega C & 1 \end{bmatrix} \begin{bmatrix} 1 & j\omega L \\ 0 & 1 \end{bmatrix} \begin{bmatrix} 1 & 0 \\ j\omega C & 1 \end{bmatrix} \tag{3.29}$$

which can be simplified as

$$\begin{bmatrix} A & B \\ C & D \end{bmatrix} = \begin{bmatrix} 1-\omega^2 LC & j\omega L \\ 2j\omega C - j\omega^3 LC^2 & 1-\omega^2 LC \end{bmatrix} \tag{3.30}$$

where ω denotes the radian frequency.

By equating the matrix parameters in (3.28) and (3.30) accordingly, we obtain

$$L = \frac{Z_c \sin\theta}{\omega} \tag{3.31}$$

$$C = \frac{1}{\omega Z_c}\sqrt{\frac{1-\cos\theta}{1+\cos\theta}} \tag{3.32}$$

For a quarter-wavelength transmission line section ($\theta = 90^\circ$), the values of the lumped elements are found as

$$L = \frac{Z_c}{\omega} \tag{3.33}$$

$$C = \frac{1}{Z_c \omega} \tag{3.34}$$

A branch-line coupler shown in Figure 3.1 consists quarter-wavelength transmission line sections of characteristic impedances Z_{01} and Z_{02}. By replacing these sections with equivalent lumped elements, the equivalent circuit for the branch-line hybrid coupler is obtained [31]. The diagram given in Figure 3.7 is the lumped-element equivalent circuit of the conventional branch-line hybrid coupler.

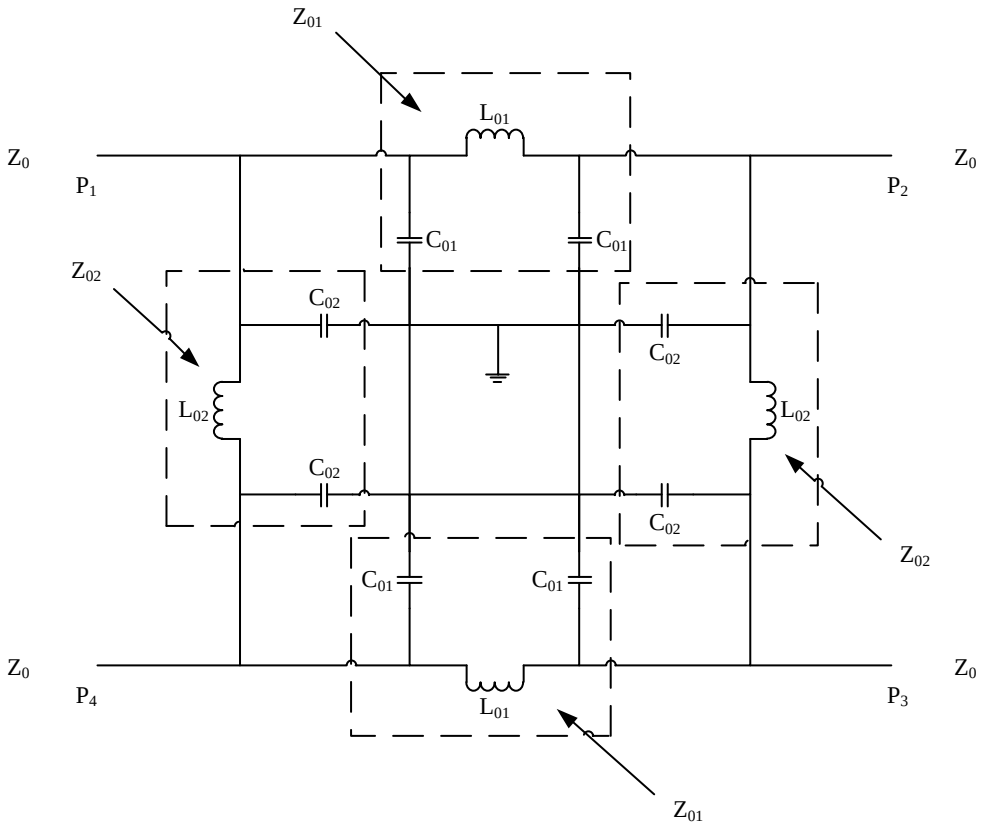

Figure 3.7: Lumped element equivalent circuit for a branch-line hybrid coupler [31].

The values of the lumped elements are given by

$$L_{01} = \frac{Z_{01}}{\omega_0} \qquad C_{01} = \frac{1}{Z_{01}\omega_0} \tag{3.35}$$

$$L_{02} = \frac{Z_{02}}{\omega_0} \qquad C_{02} = \frac{1}{Z_{02}\omega_0} \tag{3.36}$$

where ω_0 represents the radian frequency corresponding to the centre frequency of the branch-line coupler. Substituting (3.7) and (3.8) into (3.35) and (3.36) gives

$$L_{01} = \frac{Z_0}{\sqrt{2}\omega_0} \qquad C_{01} = \frac{\sqrt{2}}{Z_0\omega_0} \tag{3.37}$$

$$L_{02} = \frac{Z_0}{\omega_0} \qquad C_{02} = \frac{1}{Z_0 \omega_0} \tag{3.38}$$

3.2 Coupled resonator 90 ° hybrid coupler

In Section 3.1, we obtained the lumped element equivalent circuit for a branch-line hybrid coupler. However, in this section, we will synthesis a coupled resonator 90 ° hybrid coupler based on this equivalent circuit. We know that a parallel resonator can be seen as an open circuit at resonance. Hence four parallel resonators can be added to the four corners of the circuit shown in Figure 3.7, while the quarter-wavelength transmission lines can be seen as the couplings between resonators [32]. The topology of the proposed hybrid coupler is given Figure 3.8, where the black dot represents the resonator and the coupling is depicted by the line connecting two dots.

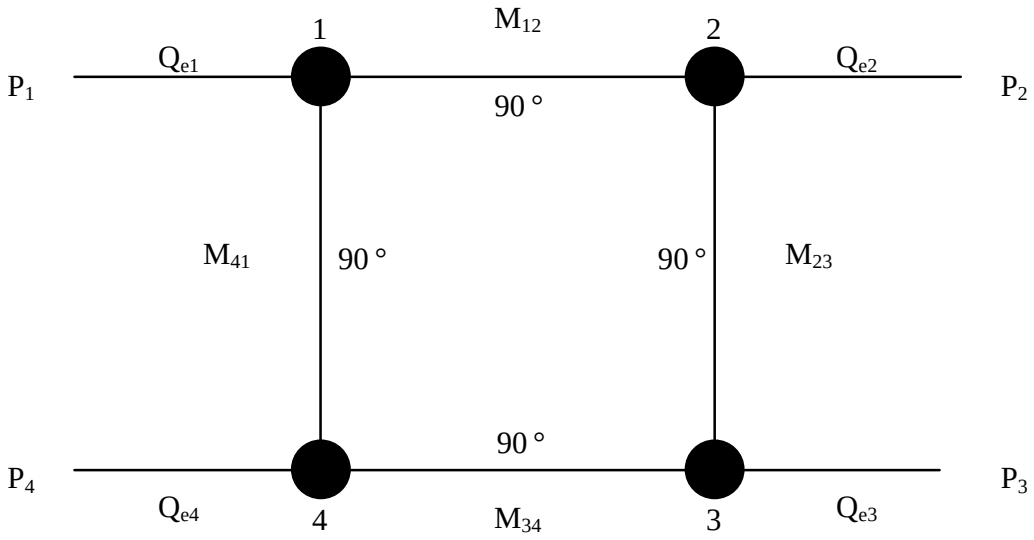

Figure 3.8: Topology of a four-coupled resonator hybrid coupler.

The proposed coupled resonator hybrid coupler can be synthesized using different ways: analytic solutions to calculate the required coupling coefficients M_{ij} and external quality

factors Q_{ei}, or optimization techniques to synthesis the coupling matrix [4;19;33]. However, in this work, we focus on the analytic solutions and will explicitly explain the calculation of coupling coefficients and external quality factors.

3.2.1 Equivalent circuit

Near resonance, a microwave resonator can usually be modelled by either a series or parallel LC lumped-element equivalent circuit. However, as discussed in the previous section, the branches are in shunt with the main line, so it is more convenient to consider a parallel resonant circuit. Four shunt resonators can thus be added to the lumped-element equivalent circuit of the branch-line hybrid coupler without changes in the behaviour of the device at the centre frequency. Shown in Figure 3.9 is the lumped-element equivalent of the 90 ° hybrid coupler with four parallel resonant circuits.

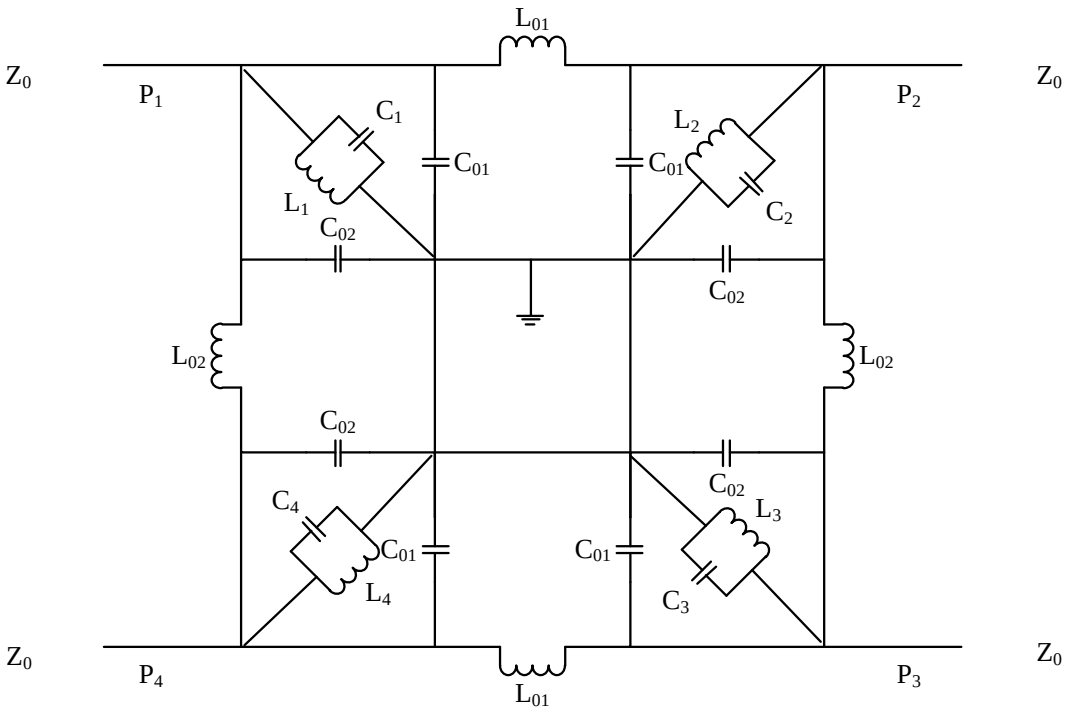

Figure 3.9: Equivalent circuit of a coupled resonator 90 °hybrid coupler [29].

3.2.2 Coupling matrix representation

The four-port coupled-resonator 90° hybrid coupler as described in previous section can be represented in terms of coupling matrix. Figure 3.10 depicts an equivalent circuit of such a coupled resonator hybrid coupler, where L_i, C_i and G_i denote the inductance, capacitance and conductance, respectively; i_s is the source current; and v_i represents the node voltage. The dash line connecting two resonators stands for the coupling between them. To derive the scattering parameters of this hybrid coupler, the circuit in Figure 3.10 is represented by a four-port network of Figure 3.11, where voltage and current variables at the ports are denoted by V_i and I_i, and a_i and b_i are the wave variables.

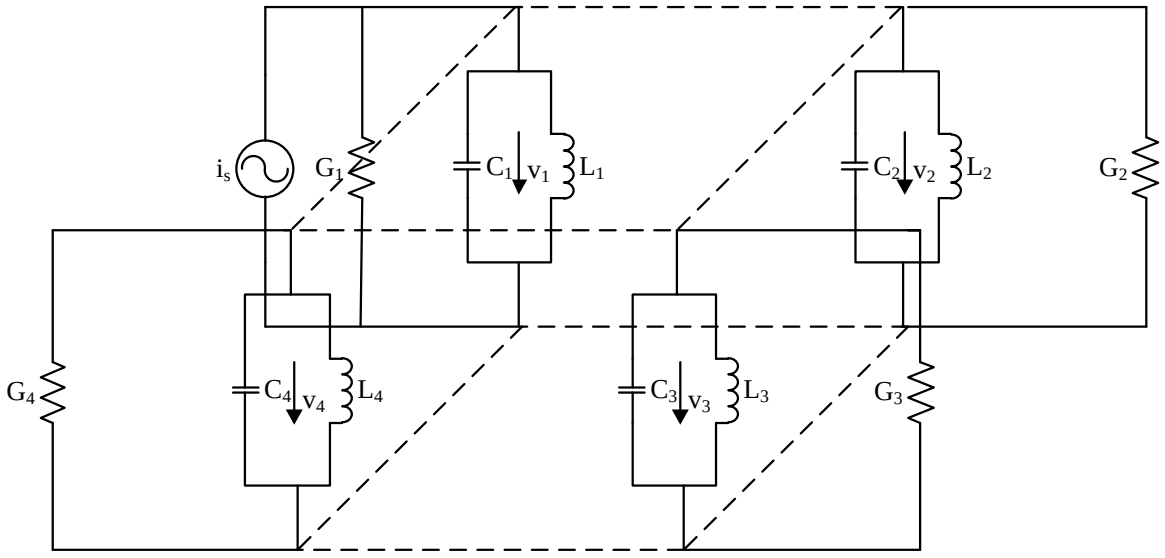

Figure 3.10: Equivalent circuit of a four-port four-coupled resonator hybrid coupler.

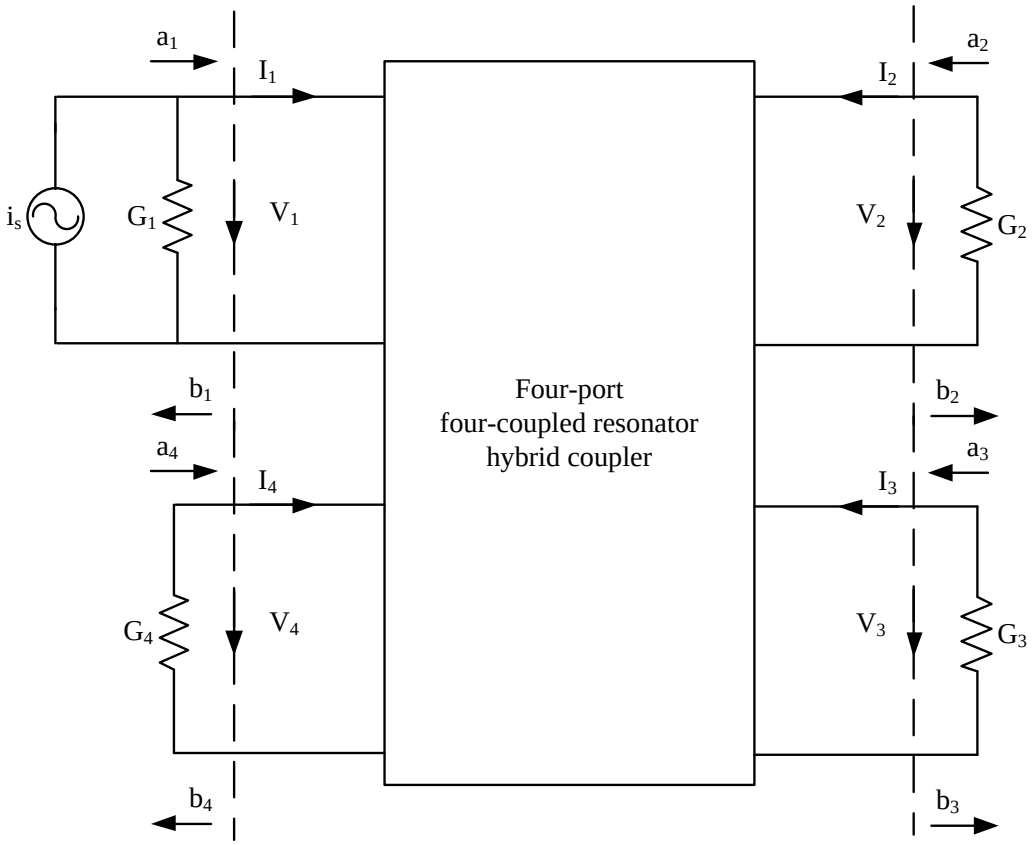

Figure 3.11: Network representation of four-port four-coupled resonator hybrid coupler.

Referring to Chapter 2, we have

$$S_{11} = \frac{2}{q_{e1}}[A]_{11}^{-1} - 1$$

$$S_{21} = \frac{2}{\sqrt{q_{e1}q_{e2}}}[A]_{21}^{-1}$$

$$S_{31} = \frac{2}{\sqrt{q_{e1}q_{e3}}}[A]_{31}^{-1} \qquad (3.39)$$

$$S_{41} = \frac{2}{\sqrt{q_{e1}q_{e4}}}[A]_{41}^{-1}$$

The normalized matrix $[A]$ of the four-coupled resonator hybrid coupler are found as

$$[A]=[q]+p[U]-j[m] \tag{3.40}$$

where $[q]$ is a 4×4 matrix with all entries zero, except for $q_{11}=1/q_{e1}$, $q_{22}=1/q_{e2}$, $q_{33}=1/q_{e3}$, $q_{44}=1/q_{e4}$, $[U]$ is the 4×4 identity matrix, and $[m]$ is the general coupling matrix.

3.2.3 Coupling coefficients and external quality factors extraction

Assume that the coupling coefficients introduced in Section 3.2.2 are based on mutual capacitance, and the associate couplings are electric couplings. The lumped element equivalent circuit for a synchronously tuned resonator circuit with electric coupling is shown in Figure 3.12, where L and C are self-inductance and self-capacitance, and C_m represents the mutual capacitance. The angular resonant frequency of the uncoupled resonator is $\omega=1/\sqrt{LC}$.

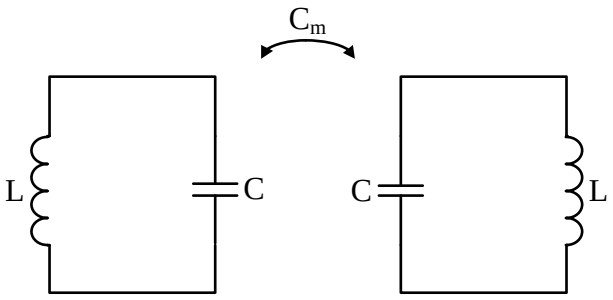

Figure 3.12: Synchronously tuned resonators with electric coupling.

However, the electric coupling can be represented by an admittance inverter $J=\omega C_m$. Figure 3.13 shows an alternative form of the equivalent circuit.

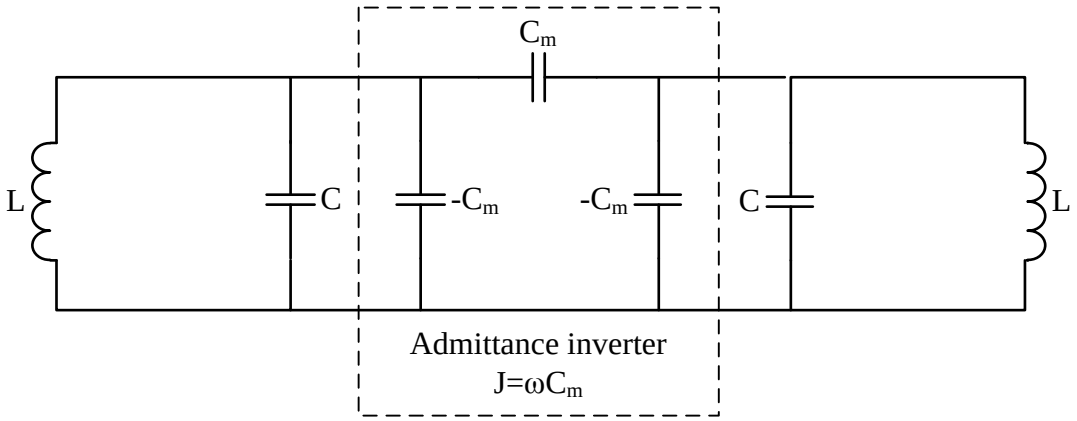

Figure 3.13: An alternative form with an admittance inverter to represent the coupling.

The electric coupling coefficient is given by [3]

$$k_E = \frac{C_m}{C} \tag{3.41}$$

Shown in Figure 3.14 (a) is the lumped element equivalent circuit of the main branch in the branch-line hybrid coupler, with the values of the lumped elements given by (3.37). An alternative form of the equivalent circuit is given in Figure 3.14 (b).

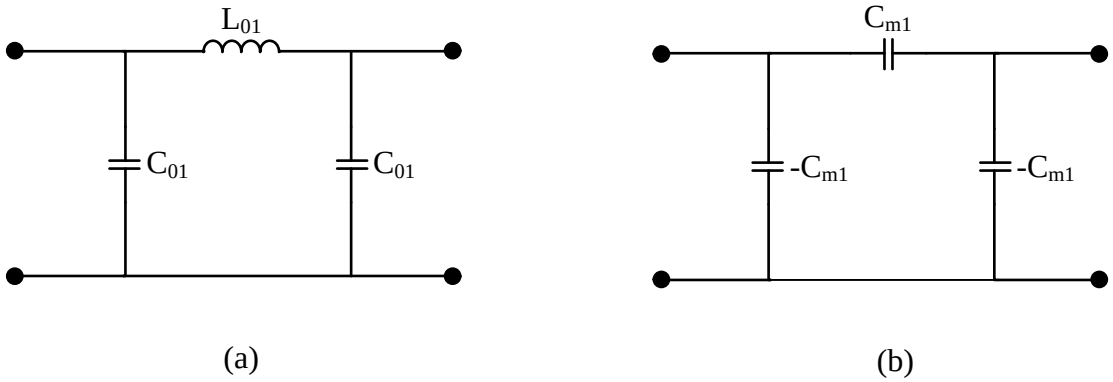

Figure 3.14: (a) Lumped element equivalent of the main branch in a branch-line hybrid coupler and (b) Alternative form of (a) with an admittance inverter.

By equating the *ABCD* matrices of the two configurations in Figure 3.14, the value of C_m can be found. Thus we can calculate the corresponding coupling coefficient.

At resonant frequency, the *ABCD* matrix of the configuration of Figure 3.14 (a) has the form

$$\begin{bmatrix} A & B \\ C & D \end{bmatrix} = \begin{bmatrix} 0 & j\omega L_{01} \\ j\omega C_{01} & 0 \end{bmatrix} \tag{3.42}$$

However, the *ABCD* matrix of the configuration of Figure 3.14 (b) is given by

$$\begin{bmatrix} A & B \\ C & D \end{bmatrix} = \begin{bmatrix} 0 & -j\dfrac{1}{\omega C_{m1}} \\ -j\omega C_{m1} & 0 \end{bmatrix} \tag{3.43}$$

Equating the elements in two *ABCD* matrices accordingly, we have

$$\begin{aligned} j\omega L_{01} &= -j\frac{1}{\omega C_{m1}} \\ j\omega C_{01} &= -j\omega C_{m1} \end{aligned} \tag{3.44}$$

which gives

$$\begin{aligned} C_{m1} &= -C_{01} \\ C_{m1} &= -\frac{1}{\omega^2 L_{01}} \end{aligned} \tag{3.45}$$

Using (3.37) in (3.45)yields

$$C_{m1} = -\frac{\sqrt{2}}{Z_0 \omega} \tag{3.46}$$

So, the coupling coefficient between resonators 1 and 2 is obtained as

$$k_{E1} = \frac{C_{m1}}{C} = -\frac{\sqrt{2}}{Z_0 \omega C} \tag{3.47}$$

Similarly, the coupling coefficient between resonators 2 and 3 can be calculated as

$$k_{E2} = \frac{C_{m1}}{C} = -\frac{1}{Z_0 \omega C} \tag{3.48}$$

The external quality factors are obtained by transforming (2.21) as

$$Q_{ei} = \frac{\omega C}{G_i} = Z_0 \omega C \qquad for \quad i = 1, \quad 2, \quad 3, \quad 4 \tag{3.49}$$

3.2.4 Frequency responses and adjustable bandwidth

For bandpass filters, the external quality factors become coarsely equal to the inverse of the fractional bandwidth (FBW) [21]. This is also true for a coupled-resonator hybrid coupler. For a hybrid coupler with a FBW of 10%, Q_e is found as $1/FBW = 10$. With reference to Figure 3.8, the coupling matrix can be calculated using (3.47) to (3.49) as

$$[M] = \begin{bmatrix} 0 & 0.1414 & 0 & 0.1 \\ 0.1414 & 0 & 0.1 & 0 \\ 0 & 0.1 & 0 & 0.1414 \\ 0.1 & 0 & 0.1414 & 0 \end{bmatrix} \tag{3.50}$$

The frequency response of the coupled-resonator hybrid coupler is plotted in Figure 3.15. Note that at the centre frequency, we obtain perfect 3dB power division in ports 2 and 3, and perfect return loss and isolation in ports 1 and 4.

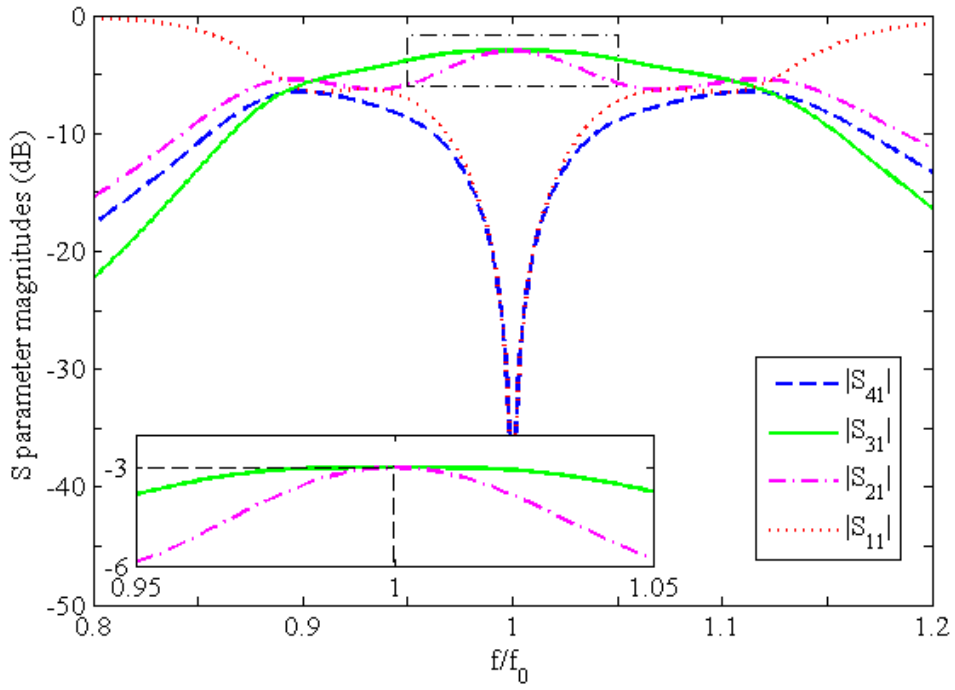

Figure 3.15: Frequency response of a four-coupled resonator 90° hybrid coupler.

Figure 3.16 shows the phase response of the 90 ° four-coupled resonator hybrid coupler. A perfect 90 °phase difference between two output ports is achieved at the centre frequency.

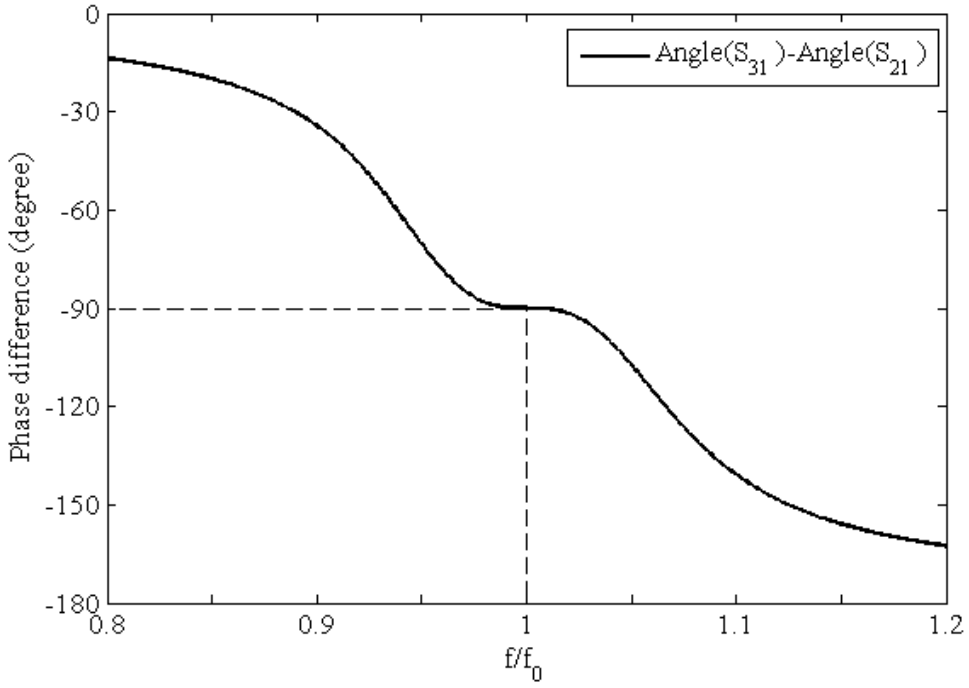

Figure 3.16: Phase difference between two output ports of a four-coupled resonator 90 ° hybrid coupler.

The *FBW* of the hybrid coupler can be changed by altering the coupling coefficients and external quality factors accordingly. The relationship between these quantities is given as

$$Q_{ei}^{'} = Q_{ei}/a$$

$$M_{ij}^{'} = M_{ij} \times a \tag{3.51}$$

$$FBW^{'} = FBW \times a$$

For example, if we double the coupling coefficients ($a = 2$) and half the external quality factors, a hybrid coupler with a *FBW* twice as large as the original one can be achieved. Figure 3.17 shows the S parameter magnitudes in decibel of two outputs with *FBW* of 10% and 20%.

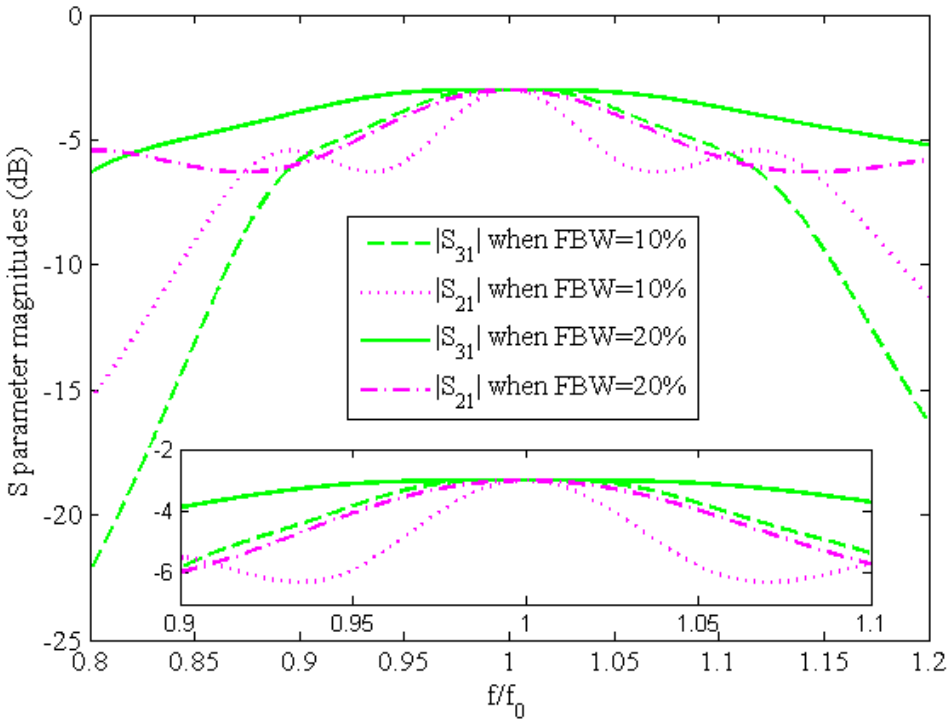

Figure 3.17: S parameter magnitudes of two output ports with different FBW .

Generally, a wider bandwidth coupled-resonator hybrid coupler can be achieved by stronger couplings between resonators.

3.3 Improved coupled resonator 90 °hybrid coupler

As shown in Figure 3.15, a perfect 3dB power division can be obtained at the centre frequency, however, the performance degrades quickly as the frequency departs from f_0. This can be improved by adding two additional resonators to the current coupled-resonator hybrid coupler. Shown in Figure 3.18 is the topology of a 90 °hybrid coupler consisting of six inter-coupled resonators.

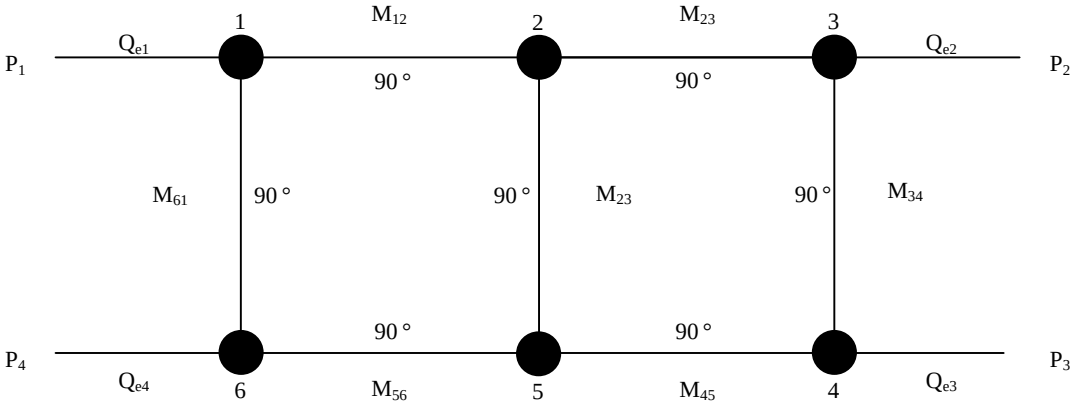

Figure 3.18: Topology of a six-coupled resonator hybrid coupler.

The coupling matrix for this topology is expressed as

$$[M]=\begin{bmatrix} 0 & M_{12} & 0 & 0 & 0 & M_{16} \\ M_{21} & 0 & M_{23} & 0 & M_{25} & 0 \\ 0 & M_{32} & 0 & M_{34} & 0 & 0 \\ 0 & 0 & M_{43} & 0 & M_{45} & 0 \\ 0 & M_{52} & 0 & M_{54} & 0 & M_{56} \\ M_{61} & 0 & 0 & 0 & M_{65} & 0 \end{bmatrix} \tag{3.52}$$

while the external quality factor matrix has the form

$$[Q]=\begin{bmatrix} Q_{e1} & 0 & 0 & 0 & 0 & 0 \\ 0 & 0 & 0 & 0 & 0 & 0 \\ 0 & 0 & Q_{e2} & 0 & 0 & 0 \\ 0 & 0 & 0 & Q_{e3} & 0 & 0 \\ 0 & 0 & 0 & 0 & 0 & 0 \\ 0 & 0 & 0 & 0 & 0 & Q_{e4} \end{bmatrix} \tag{3.53}$$

Analogous to the four-coupled resonator hybrid coupler, the coupling coefficients of the six-coupled resonator hybrid coupler can be calculated from the impedances of the three-branch branch-line coupler. Figure 3.19 depicts the geometry of a branch-line coupler with three shunt branches.

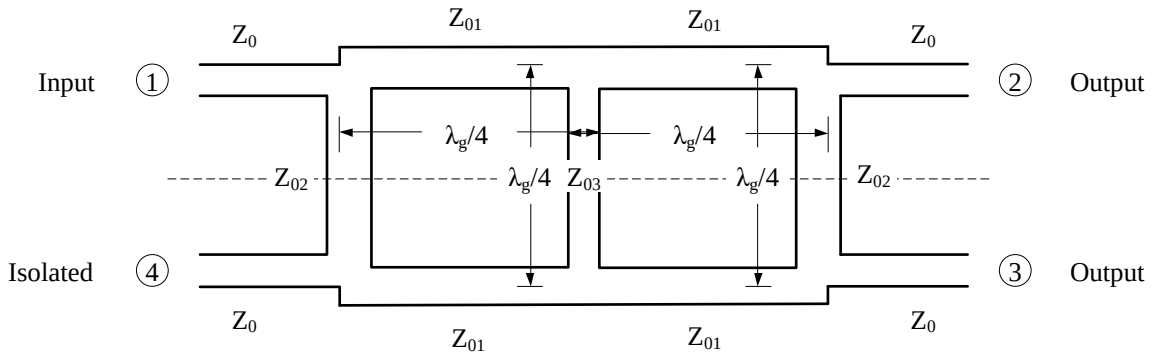

Figure 3.19: Geometry of a three-branch branch-line coupler [34].

The coupling coefficients are obtained from (3.34), (3.41) and (3.45) as

$$k_{E1} = -\frac{1}{Z_{01}\omega C} \tag{3.54}$$

$$k_{E2} = -\frac{1}{Z_{02}\omega C} \tag{3.55}$$

$$k_{E3} = -\frac{1}{Z_{03}\omega C} \tag{3.56}$$

while the external quality factors are given by (3.49) as

$$Q_{e1} = Q_{e2} = Q_{e3} = Q_{e4} = Z_0\omega C \tag{3.57}$$

With reference to [30], for 3dB coupling, the impedances of a branch-line coupler with three shunt branches are found as

$$Z_{01} = Z_{03} = \frac{1}{\sqrt{2}} Z_0 \tag{3.58}$$

$$Z_{02} = \frac{1}{\sqrt{2}-1} Z_0 \tag{3.59}$$

Hence we can calculate the required coupling coefficients for the coupled resonator hybrid coupler. For a hybrid coupler with a FBW of 10%, Q_e is found as $1/FBW = 10$. The coupling matrix is calculated as

$$[M] = \begin{bmatrix} 0 & -0.1414 & 0 & 0 & 0 & -0.0414 \\ -0.1414 & 0 & -0.1414 & 0 & -0.1414 & 0 \\ 0 & -0.1414 & 0 & -0.0414 & 0 & 0 \\ 0 & 0 & -0.0414 & 0 & -0.1414 & 0 \\ 0 & -0.1414 & 0 & -0.1414 & 0 & -0.1414 \\ -0.0414 & 0 & 0 & 0 & -0.1414 & 0 \end{bmatrix} \tag{3.60}$$

The S parameters can be represented in terms of the normalized coupling matrix and normalized external quality factor matrix. The frequency responses of the six-coupled resonator hybrid coupler are illustrated in Figure 3.20 and Figure 3.21.

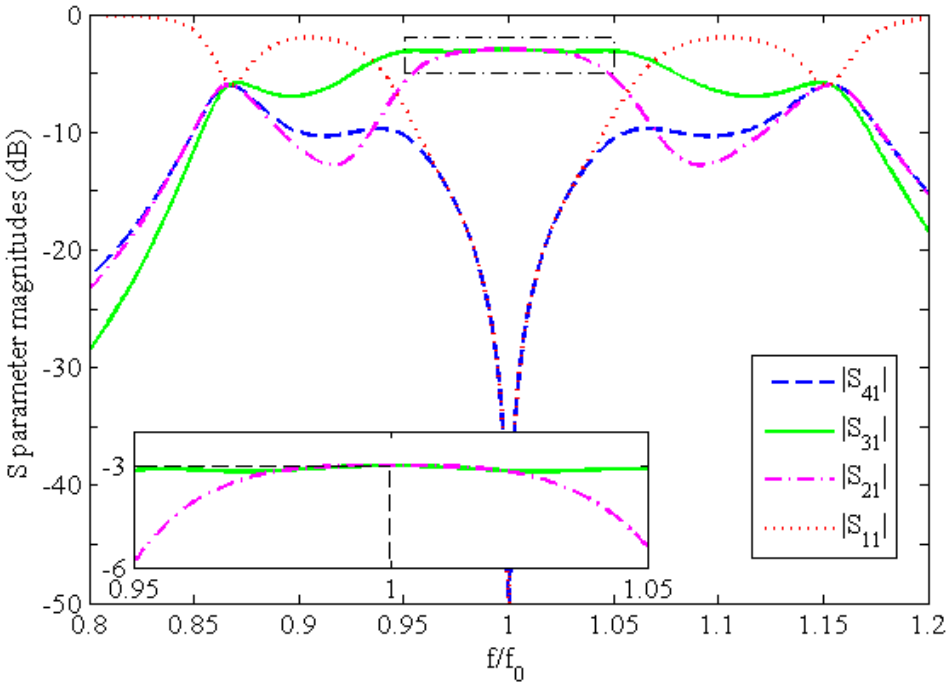

Figure 3.20: Frequency response of six-coupled resonator hybrid coupler.

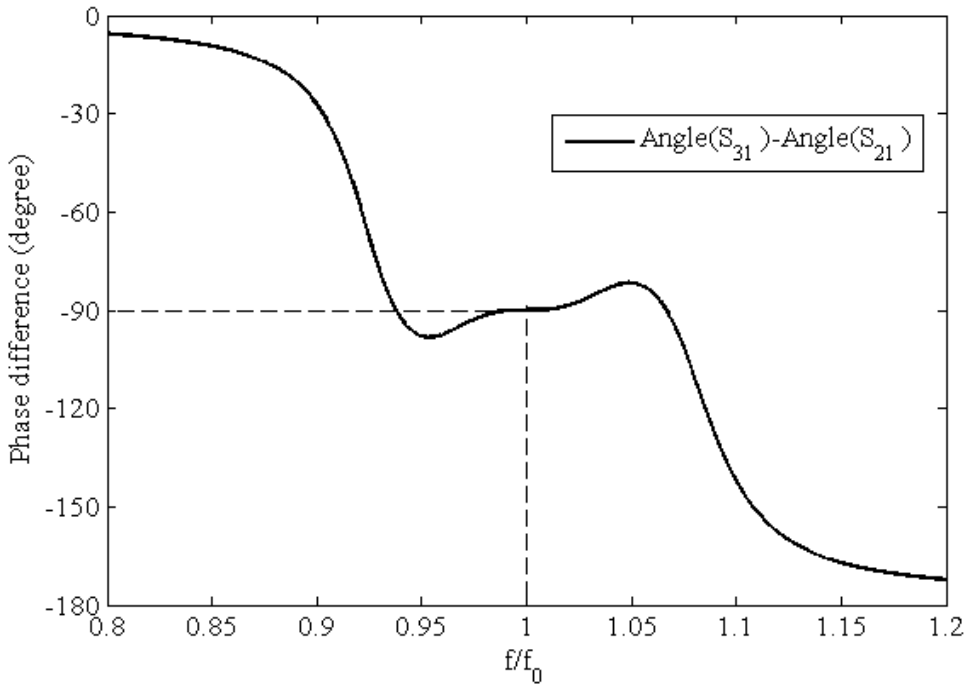

Figure 3.21: Phase difference between two output ports.

Shown in Figure 3.22 are the frequency responses of the conventional branch-line coupler, four-coupled resonator hybrid coupler and the six-coupled resonator hybrid coupler with the same 3dB bandwidth. As can be seen, all these hybrid couplers have perfect even power division near the centre frequency. As the frequency departs from f_0, the performance of the hybrid couplers degrade at different rates. With reference to Figure 3.22, the 1dB bandwidth of the conventional branch-line coupler is around 25%. For four-coupled resonator hybrid coupler, it is around 20%. However, the bandwidth can be increased to 30% with the six-coupled resonator hybrid coupler at the cost of an increased number of resonators.

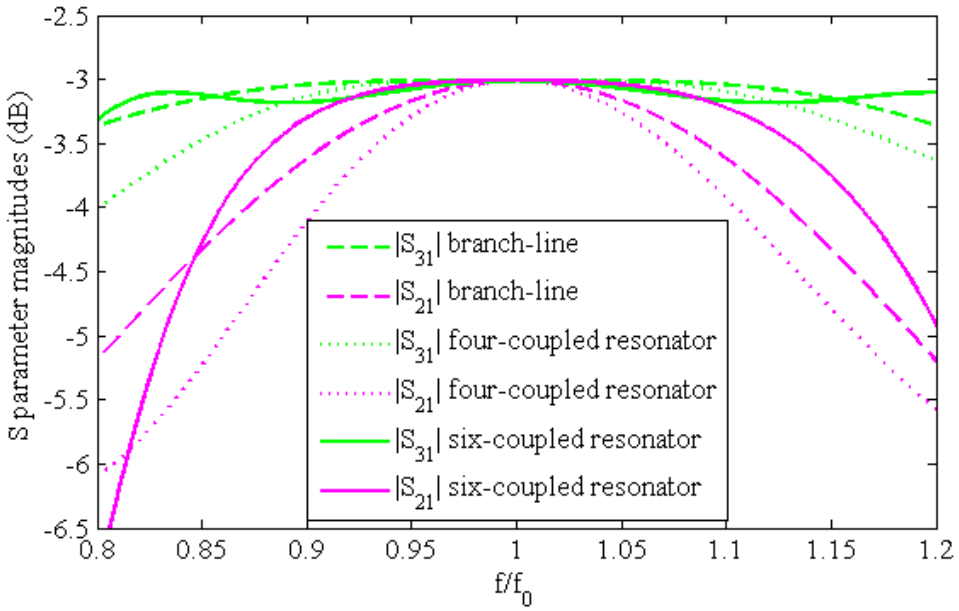

Figure 3.22: Comparison of S parameter magnitudes of output ports.

3.4 Coupled resonator 180 ° hybrid coupler

Similar to the synthesis of the coupled resonator 90 ° hybrid coupler, we will start by looking into the conventional rat-race hybrid coupler. The design of a rat-race hybrid coupler is given, and the frequency responses will be shown. We then obtain the equivalent circuit of the rat-race by substituting each section of transmission line with its lumped-element equivalent. Finally, the synthesis of the coupled-resonator 180 ° hybrid coupler is presented with a numerical example.

3.4.1 Conventional rat-race hybrid coupler

The rat-race hybrid coupler shown in Figure 3.23 can easily be fabricated using planar circuit construction. The ring hybrid has four ports with the terminal impedance Z_0. The spacing between ports 2 and 4 is $3\lambda_g / 4$, and the spacing between all other adjacent ports is $\lambda_g / 4$.

With reference to Figure 3.23, a signal applied to port 4 will be split equally into two components with 180 ° phase difference at ports 2 and 3, and port 1 will be isolated. If the input is applied to port 1, it will be evenly divided into two in-phase components at port 2 and 3, and port 4 will be isolated.

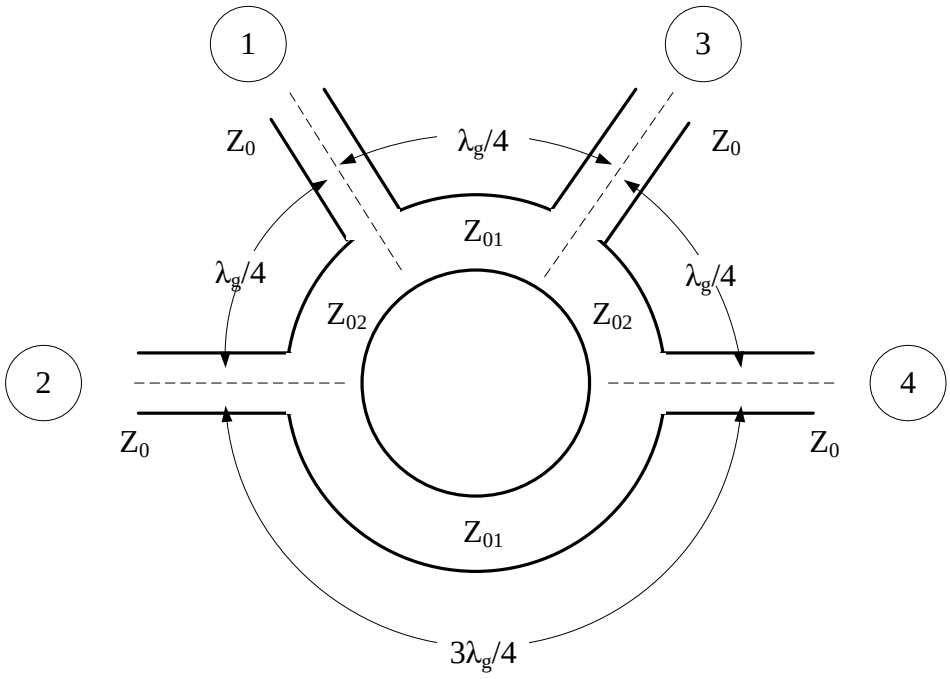

Figure 3.23: A rat-race hybrid coupler [10].

At the centre frequency, the scattering parameters of the circuit are given by [29]

$$S_{12} = -j\frac{Z_0}{Z_{02}} \tag{3.61}$$

$$S_{13} = -j\frac{Z_0}{Z_{01}} \tag{3.62}$$

$$S_{11} = S_{14} = 0 \tag{3.63}$$

and

$$S_{42} = j\frac{Z_0}{Z_{01}} \tag{3.64}$$

$$S_{43} = -j\frac{Z_0}{Z_{02}} \tag{3.65}$$

$$S_{41} = S_{44} = 0 \tag{3.66}$$

The scattering matrix of the ring hybrid has the form

$$[S] = \begin{bmatrix} 0 & -j\frac{Z_0}{Z_{02}} & -j\frac{Z_0}{Z_{01}} & 0 \\ -j\frac{Z_0}{Z_{02}} & 0 & 0 & j\frac{Z_0}{Z_{01}} \\ -j\frac{Z_0}{Z_{01}} & 0 & 0 & -j\frac{Z_0}{Z_{02}} \\ 0 & j\frac{Z_0}{Z_{01}} & -j\frac{Z_0}{Z_{02}} & 0 \end{bmatrix} \tag{3.67}$$

By properly choosing the values of Z_{01} and Z_{02}, the circuit can operate like a rat-race hybrid coupler. From scattering matrices (1.19) and (3.67) we have

$$Z_{01} = \frac{Z_0}{C_2} \tag{3.68}$$

$$Z_{02} = \frac{Z_0}{C_1} \tag{3.69}$$

Substituting(1.20) in (3.68) and (3.69) gives

$$Z_{01} = \sqrt{2}Z_0 \tag{3.70}$$

$$Z_{02} = \sqrt{2}Z_0 \tag{3.71}$$

The analysis of a rat-race hybrid coupler can be carried out using the even- and odd-mode approach [30], which has been well explained in the analysis of the branch-line coupler. The frequency response of the conventional rat-race hybrid coupler is shown in Figure 3.24. Note that an input signal applied to port 4 is evenly split between ports 2 and 3 at the centre frequency.

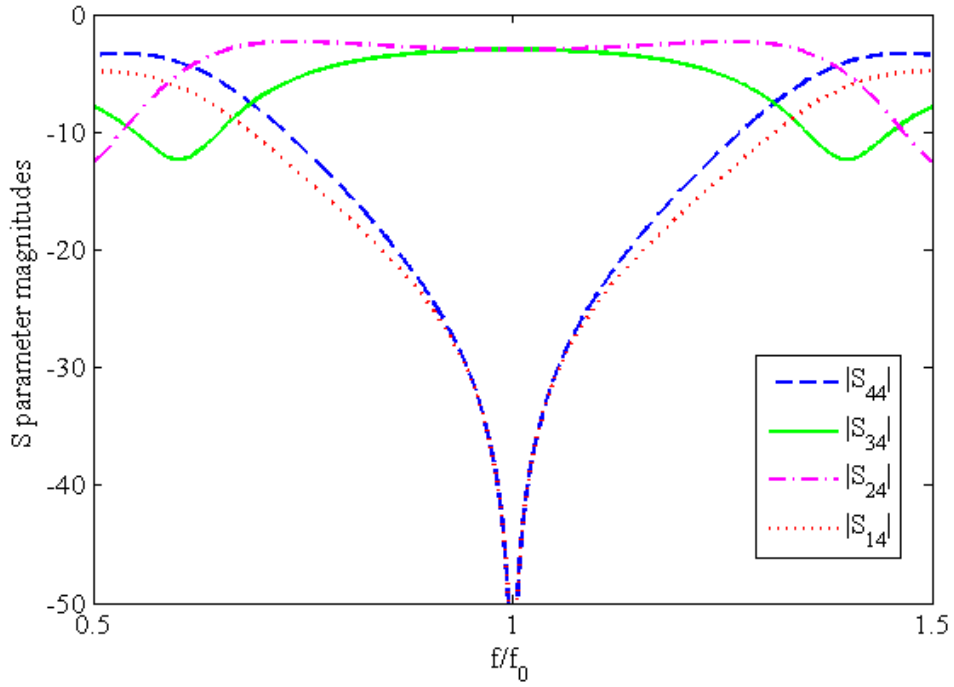

Figure 3.24: S parameter magnitudes versus frequency for rat-race hybrid coupler.

The phase difference between two output ports is plotted in Figure 3.25, where a perfect 180 ° phase difference is achieved at the centre frequency.

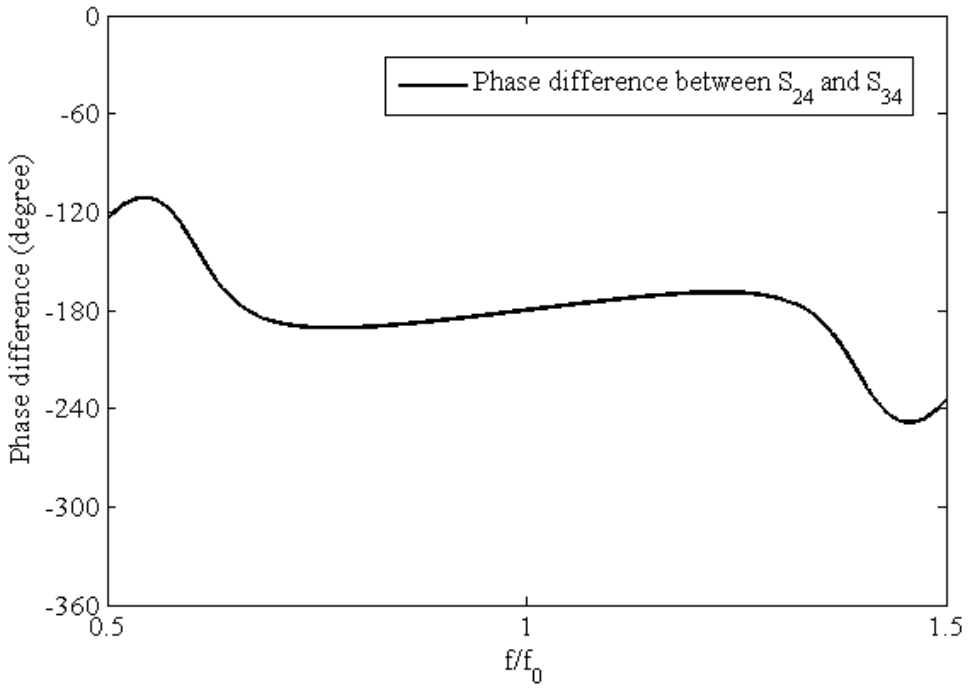

Figure 3.25: Phase difference between two output ports.

3.4.2 Equivalent circuit

A rat-race hybrid coupler as shown in Figure 3.23 consists of three quarter-wavelength transmission line sections and a three-quarter-wavelength transmission line section. Each transmission line section can be expressed by its equivalent lumped elements as shown in Figure 3.6. For a quarter-wavelength transmission line section ($\theta = 90^{\circ}$), the values of the lumped elements are given in (3.33) and (3.34). However, a three-quarter-wavelength transmission line section ($\theta = 270^{\circ}$) can be seen as three sections of quarter-wavelength transmission line. With reference to Figure 3.23, a rat-race hybrid coupler consists transmission line sections of characteristic impedances $Z_{01} = \sqrt{2}Z_0$ and $Z_{02} = \sqrt{2}Z_0$. By replacing these sections with equivalent lumped elements, the equivalent circuit for the rat-race hybrid coupler is obtained and shown in Figure 3.26.

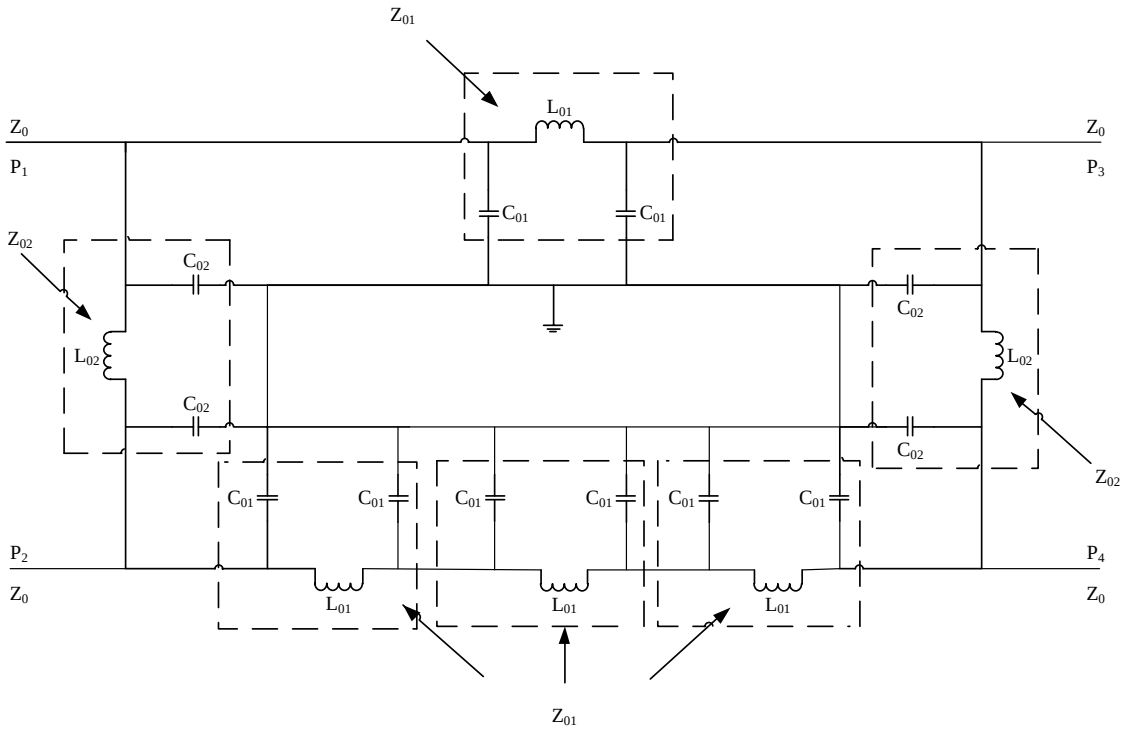

Figure 3.26: Lumped element equivalent circuit for a rat-race hybrid coupler [29].

The values of the lumped elements are given by

$$L_{01} = \frac{\sqrt{2}Z_0}{\omega_0} \qquad C_{01} = \frac{1}{\sqrt{2}Z_0\omega_0} \tag{3.72}$$

$$L_{02} = \frac{\sqrt{2}Z_0}{\omega_0} \qquad C_{02} = \frac{1}{\sqrt{2}Z_0\omega_0} \tag{3.73}$$

By adding six additional resonators to the equivalent circuit of the rat-race hybrid coupler, the equivalent circuit for a coupled-resonator $180\,°$ hybrid coupler is obtained and shown in Figure 3.27.

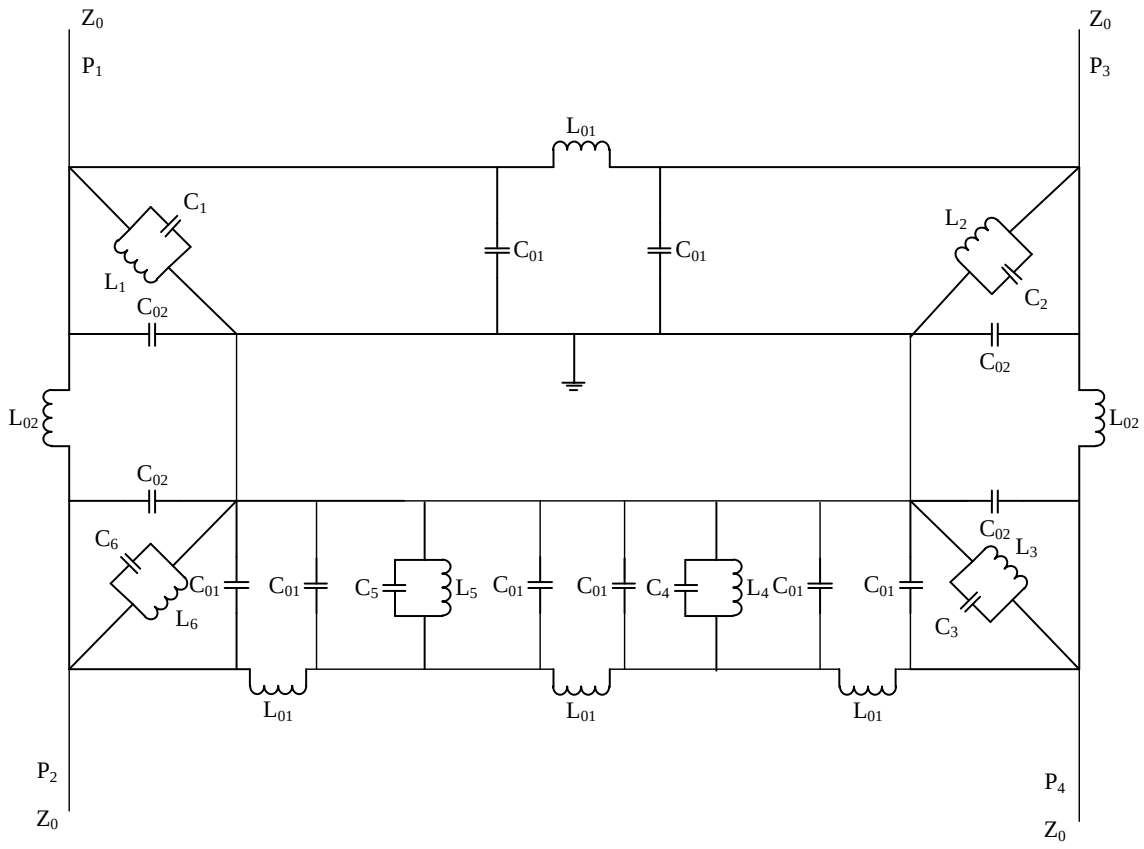

Figure 3.27: Lumped-element equivalent of a coupled-resonator 180 °hybrid coupler [29].

3.4.3 Coupling coefficients and external quality factors

The topology of a six-coupled resonator 180 °hybrid coupler is shown in Figure 3.28, where the black dot represents the resonator and the coupling is depicted by the line connecting two dots. The coupling coefficient can be calculated directly from the impedance of the corresponding transmission line section as

$$M_{12} = M_{34} = M_{45} = M_{56} = -\frac{1}{\sqrt{2}Z_0\omega C} \tag{3.74}$$

and

$$M_{23} = M_{61} = -\frac{1}{\sqrt{2}Z_0\omega C} \tag{3.75}$$

while the external quality factors are given by

$$Q_{e1} = Q_{e2} = Q_{e3} = Q_{e4} = Z_0\omega C \tag{3.76}$$

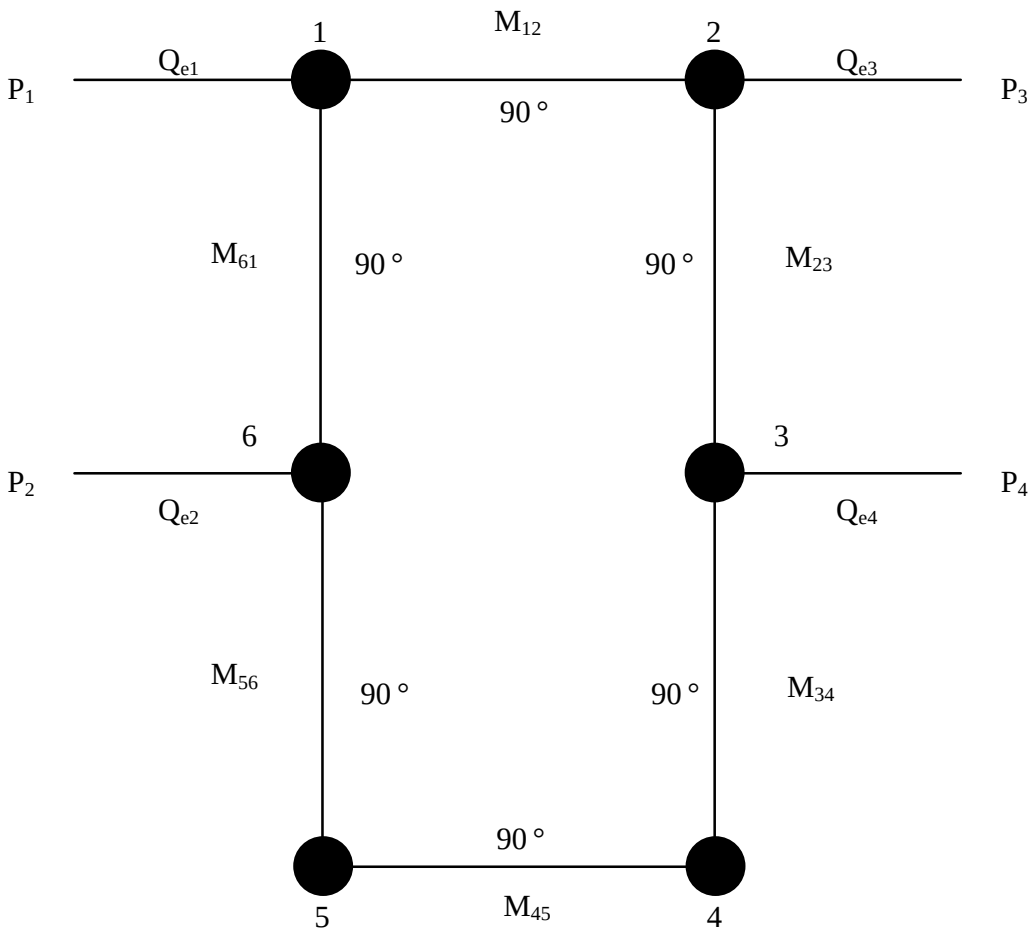

Figure 3.28: Topology of a six-coupled resonator 180° hybrid coupler.

3.4.4 Frequency responses

For a hybrid coupler with a FBW of 10%, Q_e is found as $1/FBW = 10$. The coupling matrix can be calculated as

$$[M]=\begin{bmatrix} 0 & -0.0707 & 0 & 0 & 0 & -0.0707 \\ -0.0707 & 0 & -0.0707 & 0 & 0 & 0 \\ 0 & -0.0707 & 0 & -0.0707 & 0 & 0 \\ 0 & 0 & -0.0707 & 0 & -0.0707 & 0 \\ 0 & 0 & 0 & -0.0707 & 0 & -0.0707 \\ -0.0707 & 0 & 0 & 0 & -0.0707 & 0 \end{bmatrix} \tag{3.77}$$

The frequency responses of the six-coupled resonator 180 °hybrid coupler are given in Figure 3.29 and Figure 3.30, where a perfect performance at centre frequency can be seen.

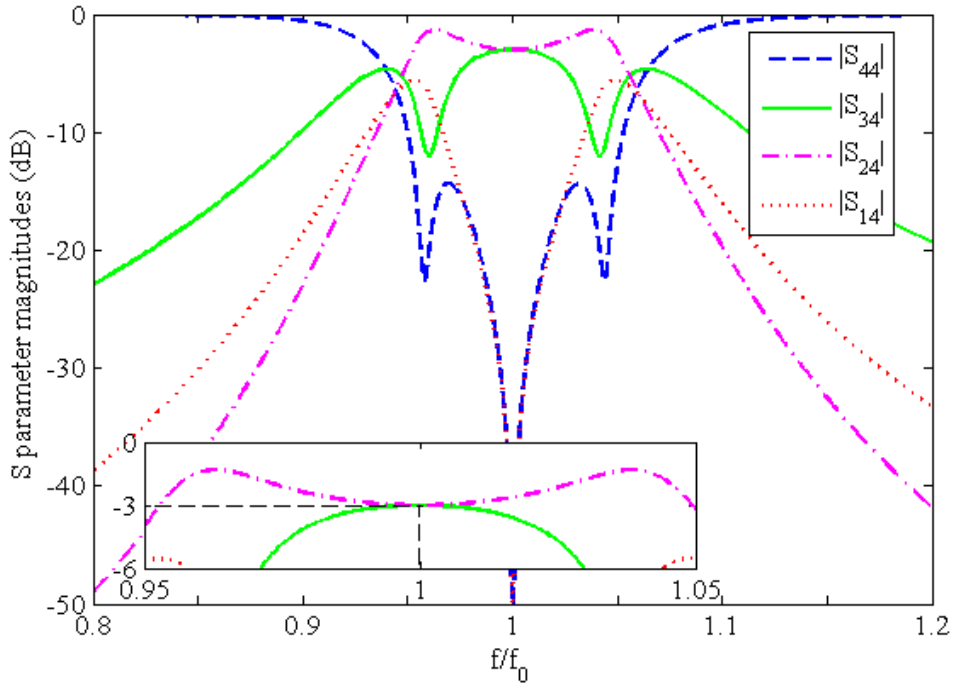

Figure 3.29: Frequency response of the six-coupled resonator 180° hybrid coupler.

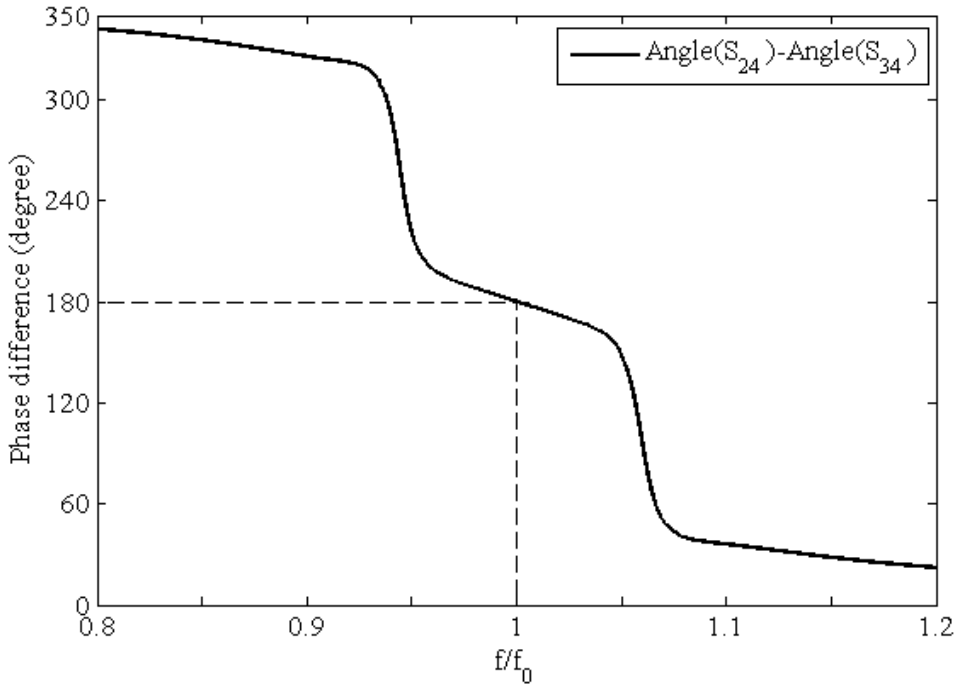

Figure 3.30: Phase difference between two output ports.

3.4.5 180 ° coupled resonator hybrid coupler with improved response

The coupled resonator hybrid coupler synthesized in the previous section is based on the conventional rat-race hybrid coupler. Although it operates perfectly at the centre frequency, the bandwidth is narrow. An improved rat-race hybrid coupler is proposed in [35] and the configuration is given in Figure 3.31. As can be seen four quarter-wave transformers are added to the four ports of the conventional rat-race hybrid coupler. Values of the parameters of the improved rat-race hybrid coupler are given in Table 1.

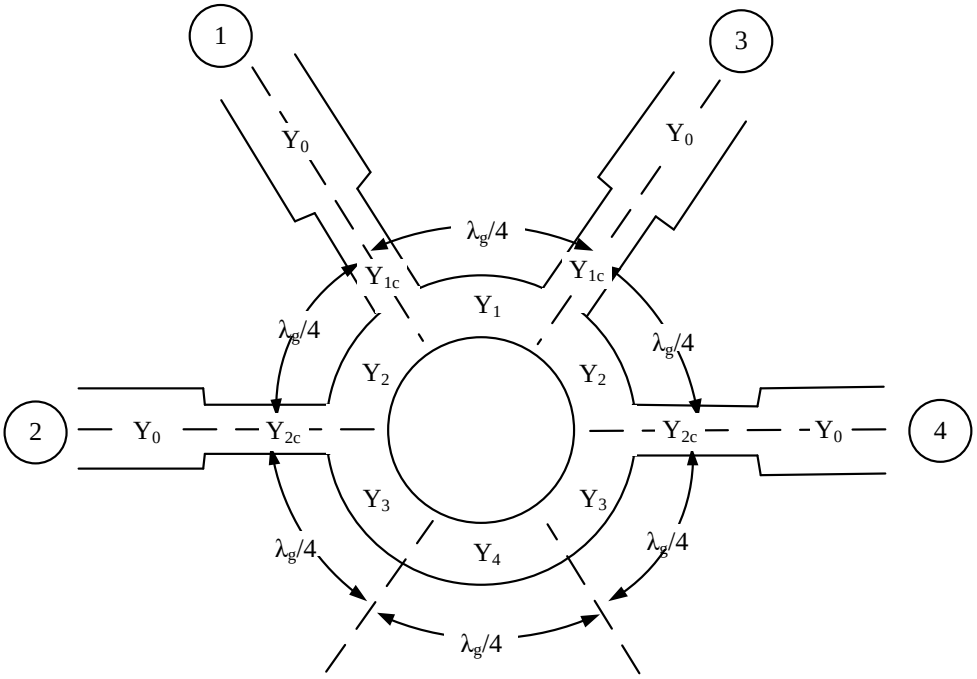

Figure 3.31: Configuration of an improved rat-race hybrid coupler [35].

The same method is used to obtain the equivalent circuit of the improved rat-race hybrid. Based on the topology shown in Figure 3.28, the topology of the improved 180 ° coupled resonator hybrid coupler can be obtained by adding four resonators to four ports, and is given in Figure 3.32.

Table 1: Optimized values of the parameters of the improved rat-race hybrid coupler [35].

Y_1	Y_2	Y_3	Y_4	Y_{1c}	Y_{2c}
0.7446	1.0114	1.128	1.128	0.9962	1.3758

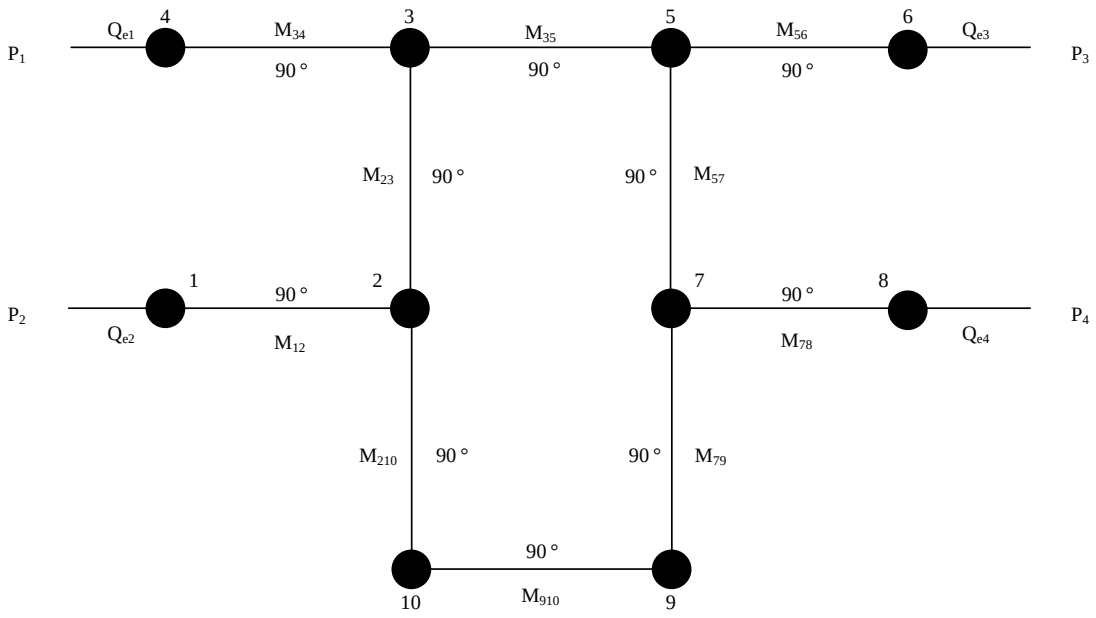

Figure 3.32: Topology of the improved coupled resonator 180° hybrid coupler.

The coupling matrix can be calculated from the values in Table 1 by using the equation $M_{Ei} = -\frac{1}{Z_i \omega C} = -\frac{Y_i}{\omega C}$, and the external quality factors are given by $Q_{e1} = Q_{e2} = Q_{e3} = Q_{e4} = \omega C / Y_0$. When FBW is 30%, Q_e is found as $1/FBW = 3.33$. The coupling matrix is calculated as

$$[M] = \begin{bmatrix} 0 & 0.4127 & 0 & 0 & 0 & 0 & 0 & 0 & 0 & 0 \\ 0.4127 & 0 & 0.3034 & 0 & 0 & 0 & 0 & 0 & 0 & 0.3384 \\ 0 & 0.3034 & 0 & 0.2989 & 0.2234 & 0 & 0 & 0 & 0 & 0 \\ 0 & 0 & 0.2989 & 0 & 0 & 0 & 0 & 0 & 0 & 0 \\ 0 & 0 & 0.2234 & 0 & 0 & 0.2989 & 0.3034 & 0 & 0 & 0 \\ 0 & 0 & 0 & 0 & 0.2989 & 0 & 0 & 0 & 0 & 0 \\ 0 & 0 & 0 & 0 & 0.3034 & 0 & 0 & 0.4127 & 0.3384 & 0 \\ 0 & 0 & 0 & 0 & 0 & 0 & 0.4127 & 0 & 0 & 0 \\ 0 & 0 & 0 & 0 & 0 & 0 & 0.3384 & 0 & 0 & 0.3384 \\ 0 & 0.3384 & 0 & 0 & 0 & 0 & 0 & 0 & 0.3384 & 0 \end{bmatrix} \quad (3.78)$$

The frequency response and phase response are given in Figure 3.33 and Figure 3.34 respectively.

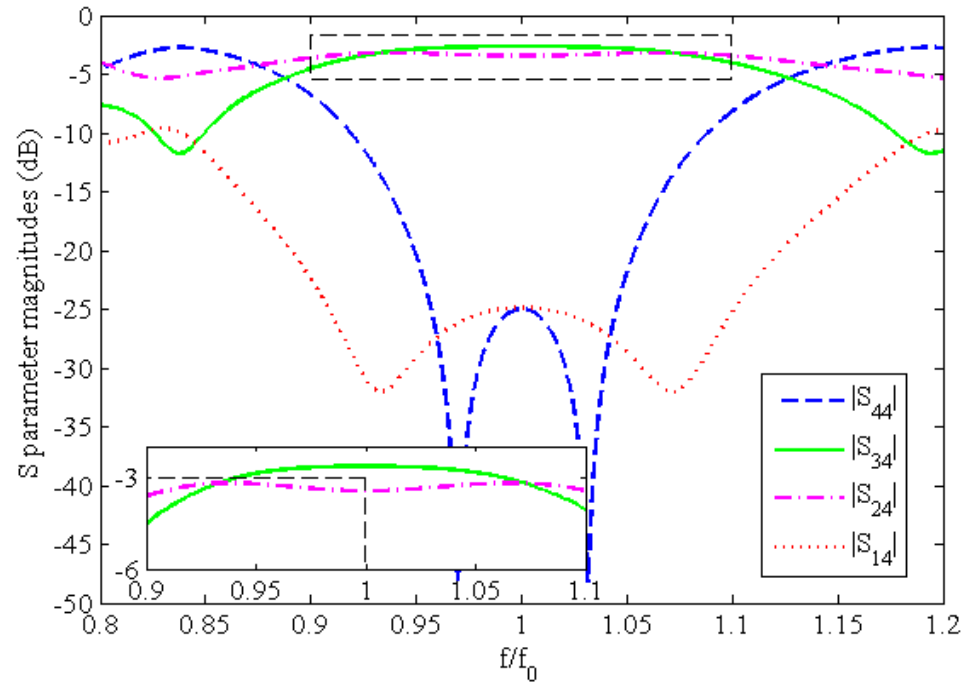

Figure 3.33: Frequency response of the ten-coupled resonator 180° hybrid coupler.

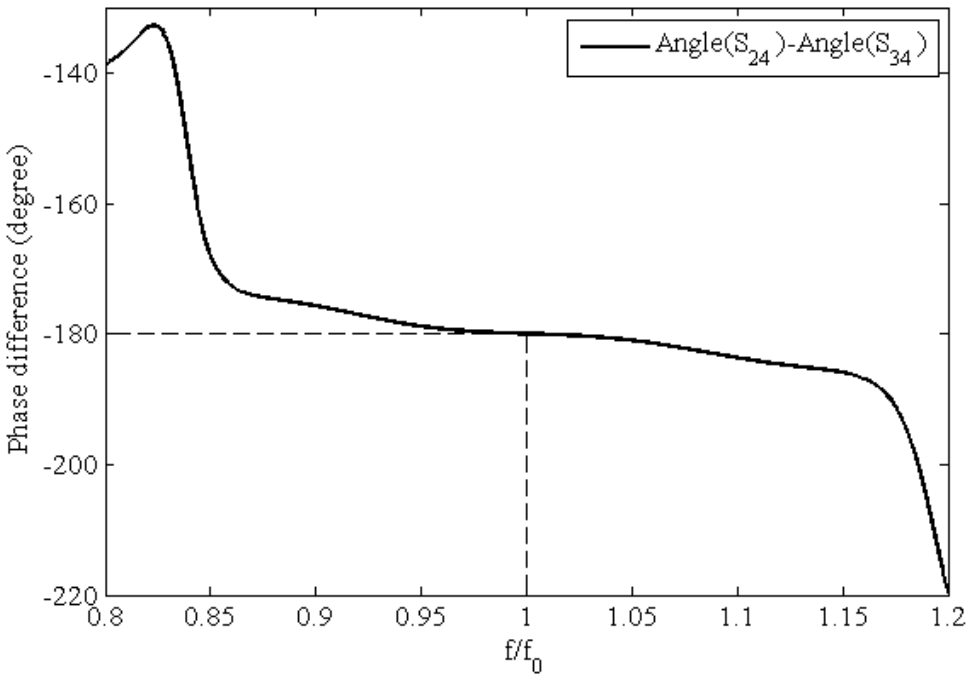

Figure 3.34: Phase response of the ten-coupled resonator 180° hybrid coupler.

The comparison of the response curves of the conventional rat-race, six-coupled resonator 180 ° hybrid coupler, and ten-coupled resonator 180 ° hybrid coupler is shown in Figure 3.35. Here, both the rat-race and six-coupled resonator hybrid coupler have a perfect performance at centre frequency. However, the ten-coupled resonator hybrid coupler realizes a wider bandwidth at the expense of ±0.5dB deviation from 3dB at the centre frequency.

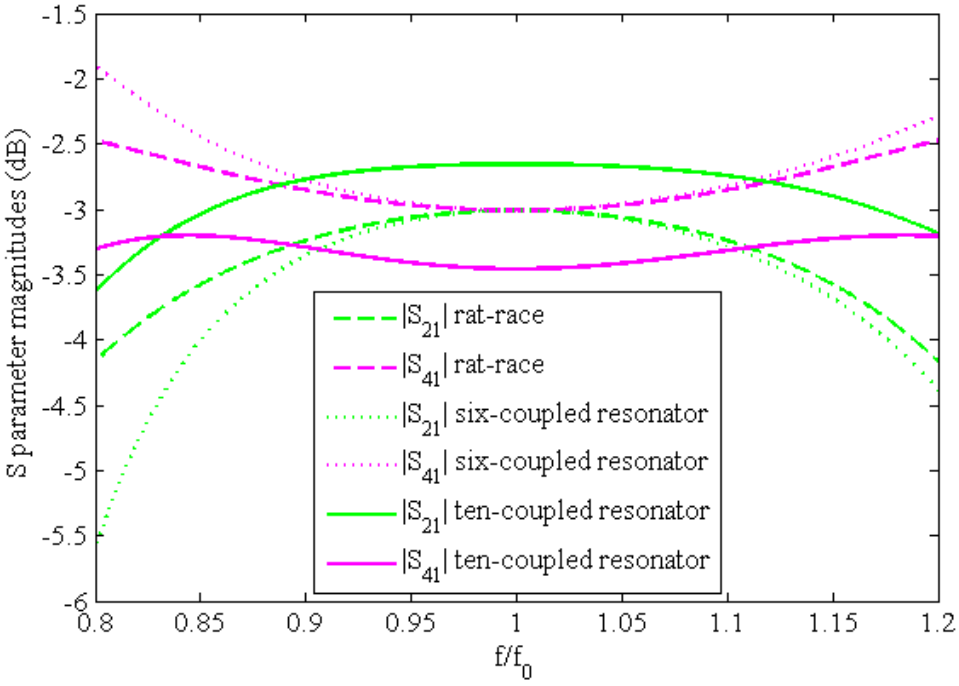

Figure 3.35: Comparison of the rat-race hybrid coupler, the six-coupled resonator hybrid coupler and the ten-coupled resonator hybrid coupler.

Chapter 4

Waveguide Resonator Implementation of a 90 ° Hybrid Coupler

The previous chapter discusses the synthesis and numerical design of both 90 ° and 180 ° coupled resonator hybrid couplers. In this chapter, the implementation of an X-band 90 ° hybrid coupler using waveguide cavity resonators is presented. Waveguide cavity resonators are chosen because of their high unloaded quality factors. We will first describe some general properties of the waveguide cavity resonator, including the resonant frequency and the unloaded quality factor. Then we will extract coupling coefficients and external quality factors from physical structures. Design of the physical dimensions of the coupled-resonator 90 ° hybrid coupler is also provided. Finally, we discuss the fabrication and measurement results of the proposed device.

4.1 Properties of waveguide cavity resonators

The waveguide cavity resonator [9] is constructed from a closed section of waveguide. Figure 4.1 depicts the geometry of a rectangular waveguide cavity. It consists of a length d of waveguide shorted at both ends ($z = 0,\ d$).

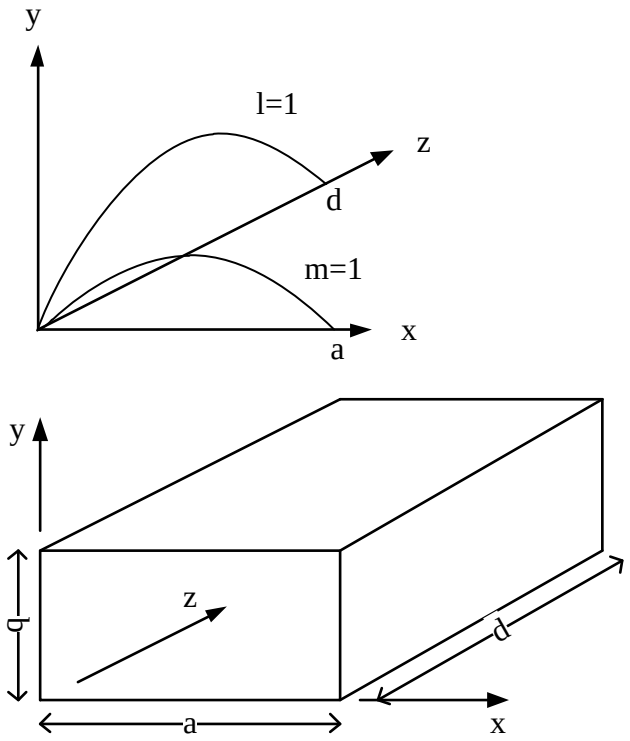

Figure 4.1: Geometry of a rectangular waveguide resonator [9].

The transverse electric fields (E_x, E_y) of the TE_{mn} or TM_{mn} rectangular waveguide mode can be written as [9]

$$\vec{E}_t(x,y,z) = \vec{e}(x,y)\left[A^+ e^{-j\beta_{mn}z} + A^- e^{j\beta_{mn}z}\right] \tag{4.1}$$

where $\vec{e}(x,y)$ is the transverse variation of the mode, and A^+, A^- are amplitudes of the forward and backward travelling waves. The propagation constant of *TE* or *TM* mode is given as [9]

$$\beta_{mn} = \sqrt{k^2 - \left(\frac{m\pi}{a}\right)^2 - \left(\frac{n\pi}{b}\right)^2} \tag{4.2}$$

where $k = \omega\sqrt{\mu\varepsilon}$, and μ, ε are the permeability and permittivity of the material filling the waveguide.

Applying the boundary condition that $\vec{E}_t = 0$ at $z = 0$ to (4.1) implies that $A^+ = A^-$. Then apply the condition that $\vec{E}_t = 0$ at $z = d$ yields

$$\vec{E}_t(x, y, d) = -\vec{e}(x, y) A^+ 2j \sin \beta_{mn} d = 0 \tag{4.3}$$

which implies

$$\beta_{mn} d = l\pi, \qquad l = 1, \quad 2, \quad 3, \quad \cdots \tag{4.4}$$

Thus the waveguide cavity must be an integer multiple of a half-guide wavelength long at the resonant frequency. A cutoff wavenumber for the rectangular cavity can be defined as [9]

$$k_{mnl} = \sqrt{\left(\frac{m\pi}{a}\right)^2 + \left(\frac{n\pi}{b}\right)^2 + \left(\frac{l\pi}{d}\right)^2} \tag{4.5}$$

where m, n, l refer to the number of variations in the standing wave pattern in the x, y, z directions, respectively. For the TE_{mnl} or TM_{mnl} mode, the resonant frequency is given by [9]

$$f_{mnl} = \frac{ck_{mnl}}{2\pi\sqrt{\mu_r \varepsilon_r}} = \frac{c}{2\pi\sqrt{\mu_r \varepsilon_r}} \sqrt{\left(\frac{m\pi}{a}\right)^2 + \left(\frac{n\pi}{b}\right)^2 + \left(\frac{l\pi}{d}\right)^2} \tag{4.6}$$

If $b < a < d$, the dominant resonant mode (lowest resonant frequency) is the TE_{101} mode. From (4.6) we found that the resonant frequency for TE_{101} mode is

$$f_{101} = \frac{ck_{101}}{2\pi\sqrt{\mu_r \varepsilon_r}} = \frac{c}{2\pi\sqrt{\mu_r \varepsilon_r}} \sqrt{\left(\frac{\pi}{a}\right)^2 + \left(\frac{\pi}{d}\right)^2} \tag{4.7}$$

The unloaded quality factor Q_u, which describes the quality of the resonator in terms of losses and energy storage, is generally defined as

$$Q_u = \omega \frac{average \quad energy \quad stored \quad in \quad the \quad resonator}{average \quad power \quad lost \quad in \quad the \quad resonator} \tag{4.8}$$

The losses may come from the finite conductivity of the cavity walls, the lossy dielectric filling material, and the radiation. Formally, the unloaded quality factor is defined as

$$\frac{1}{Q_u} = \frac{1}{Q_c} + \frac{1}{Q_d} + \frac{1}{Q_r} \tag{4.9}$$

If the cavity is filled with air and there is no radiation loss, the last two terms on the right in (4.9) are equal to zero. Thus the unloaded quality factor can be evaluated from the finite conductivity losses as [9]

$$Q_u = Q_c = \frac{\left(k_{101} ad\right)^3 b\eta}{2\pi^2 R_s \left(2a^3 b + 2d^3 b + a^3 d + d^3 a\right)} \tag{4.10}$$

where $\eta = \sqrt{\mu/\varepsilon}$ is the wave impedance, and $R_s = \sqrt{\frac{\omega\mu}{2\sigma}}$ is the resistance of the conducting walls with a conductivity σ.

Generally, the insertion loss of the coupled-resonator circuit is inversely proportional to the unloaded quality factor. Waveguide cavity resonators are chosen because of their high unloaded quality factor, thus low insertion loss.

4.2 Extraction of the coupling coefficient from the physical structure

The coupling coefficient of coupled microwave resonators can be found by using full-wave EM simulation. CST [36] is one of the commercially available software packages and is used to perform EM simulations throughout this work. Figure 4.2 shows the physical model used to extract the coupling coefficient of two coupled waveguide cavity resonators.

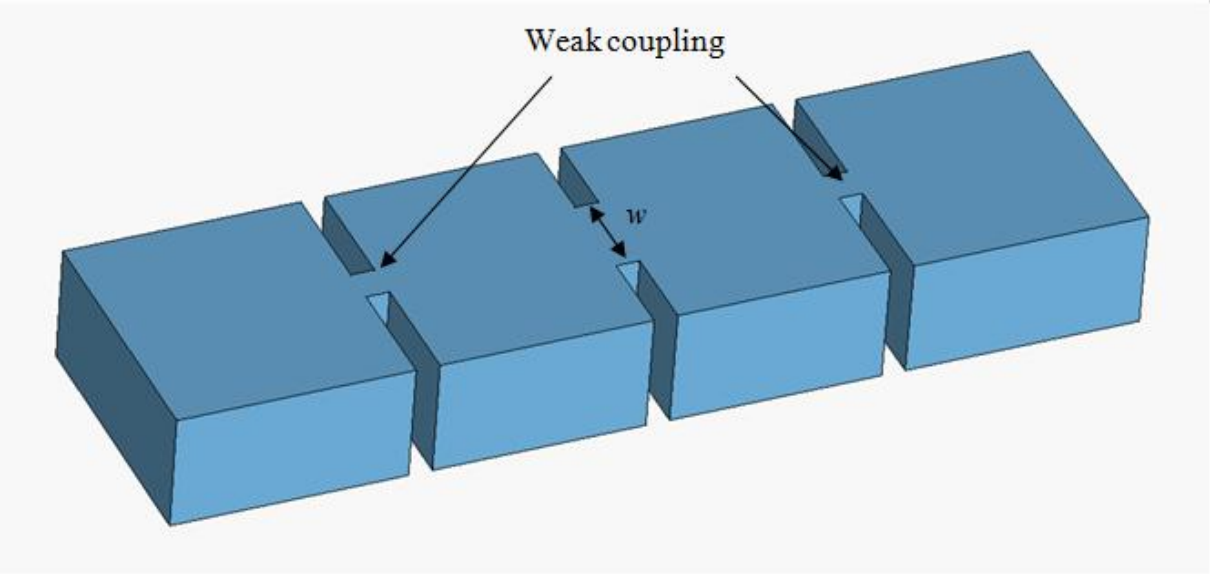

Figure 4.2: Model used to deduce the coupling coefficient of a pair of coupled resonators.

Note that the two coupled resonators should be weakly coupled to the input and output external ports so as to minimise the influence of the external coupling. This is achieved by a narrow iris between the resonator and the external port as shown in Figure 4.2. The simulated frequency response $|S_{21}|$ of the coupling structure is given in Figure 4.3, where two peaks can been seen at frequency ω_1 and ω_2. For a pair of synchronously tuned resonators, the coupling coefficient is defined as [3]

$$k = \frac{\omega_2^{\,2} - \omega_1^{\,2}}{\omega_2^{\,2} + \omega_1^{\,2}} \tag{4.11}$$

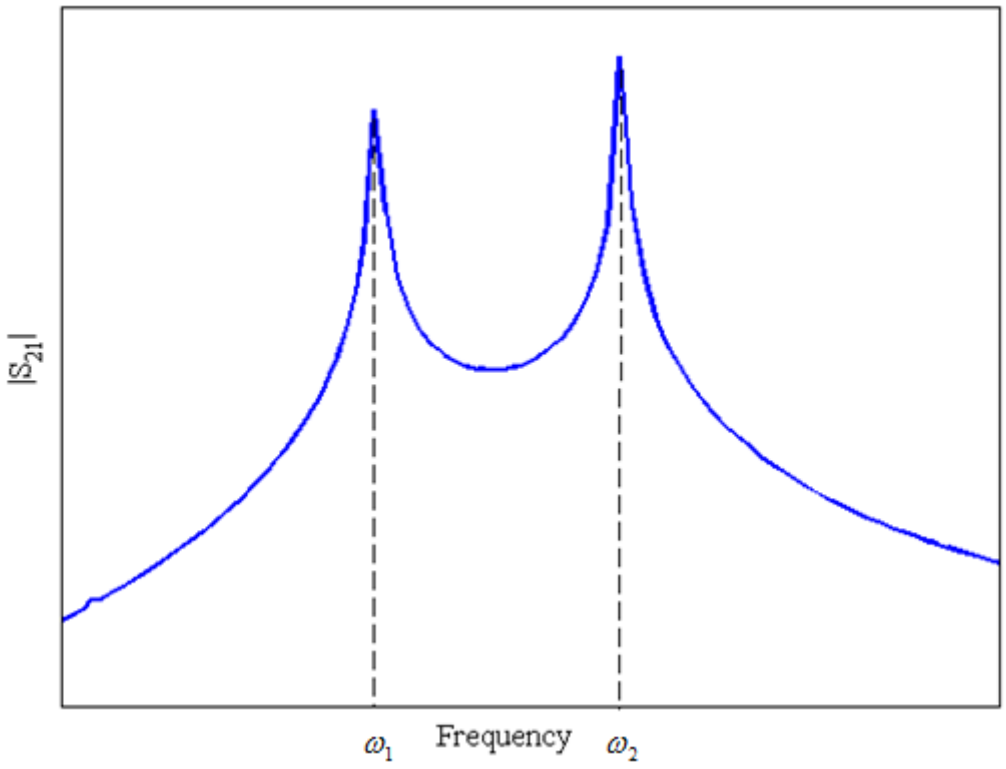

Figure 4.3: Frequency response of two coupled resonators showing two peaks.

From (4.11) it can be seen that the wider the separation between two peaks, the stronger the coupling. By altering the width of the coupling iris *w* between two resonators, the desired coupling coefficient can be achieved. A series of EM simulations may be performed by CST to produce the graph of the coupling coefficient against varying coupling iris dimensions, as shown in Figure 4.4

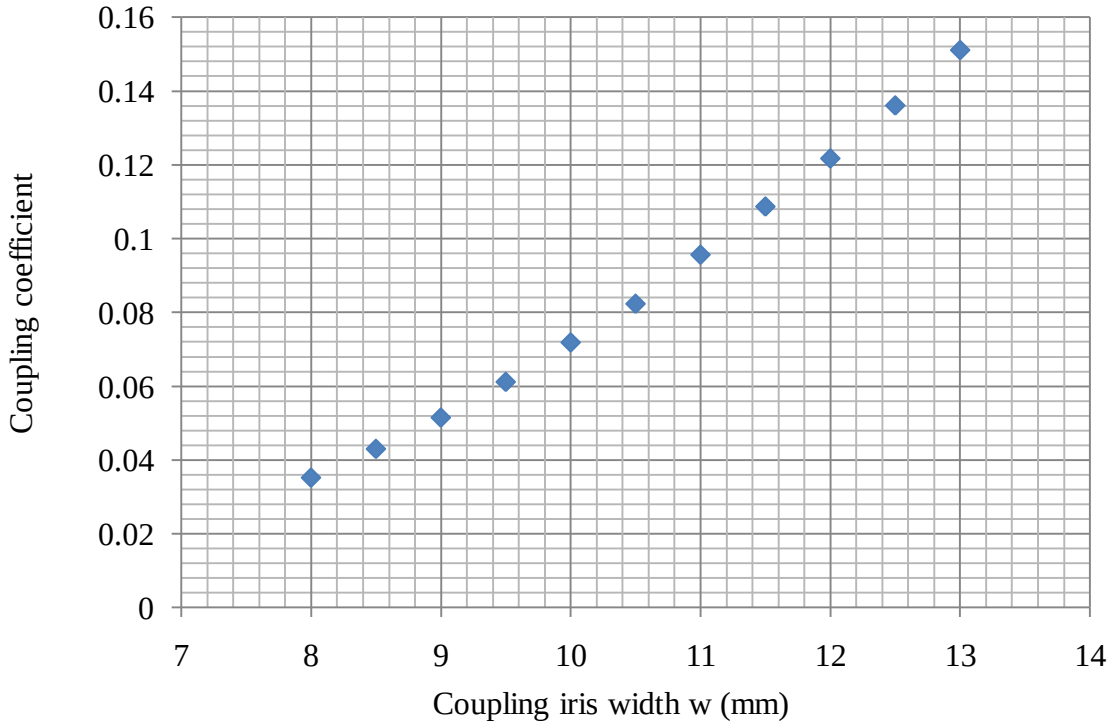

Figure 4.4 Coupling coefficient against varying coupling iris dimensions

4.3 Extraction of the external quality factor from the physical structure

Similarly, the external quality factor can be extracted from the frequency response of the resonator. Simulations are carried out using the structure as shown in Figure 4.5, where the resonator is symmetrically coupled to the input and output ports.

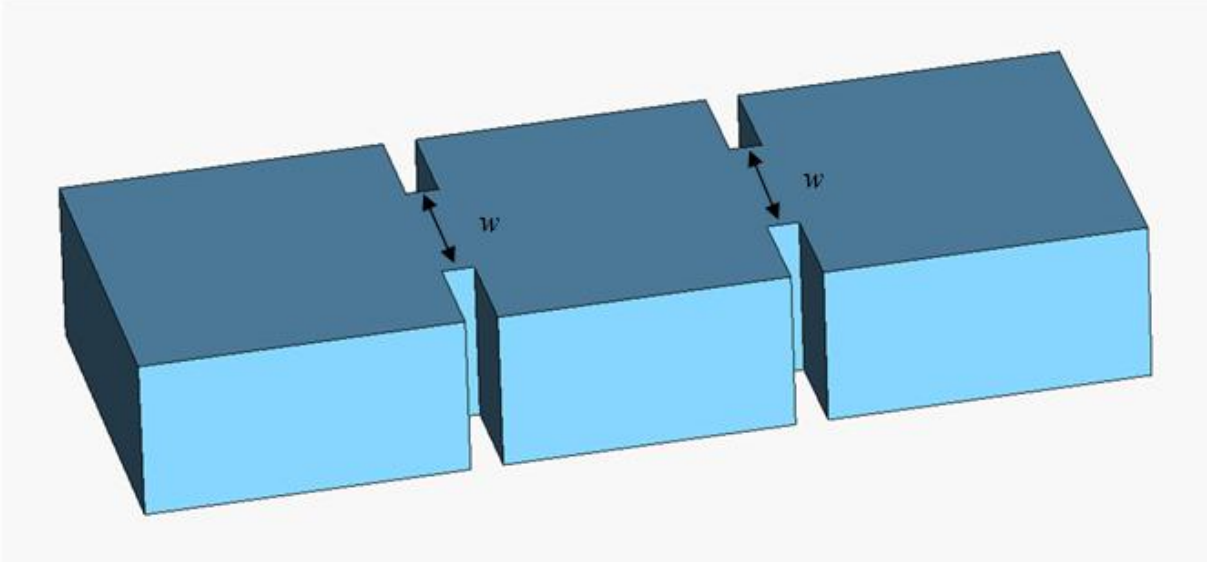

Figure 4.5: Model used to extract external quality factor of a waveguide cavity resonator.

The doubly loaded external quality factor [3] is defined as

$$Q_e' = \frac{\omega_0}{\Delta\omega_{3dB}} = \frac{Q_e}{2} \tag{4.12}$$

where ω_{3dB} is the bandwidth for which the attenuation for $|S_{21}|$ is 3dB from that at resonance, as indicated in Figure 4.6. The doubly loaded external quality factor Q_e' can be calculated from the frequency response by using (4.12). Then the external quality factor Q_e is simply twice of Q_e'. By symmetrically altering the coupling iris dimensions, the desired external quality factor can be obtained. However, the introduction of external coupling iris causes a decrease in the resonant frequency. Therefore the dimensions of the cavity must be slightly altered until the desired centre frequency is again obtained. A graph of the external quality factor against different coupling iris dimensions is plotted in Figure 4.7.

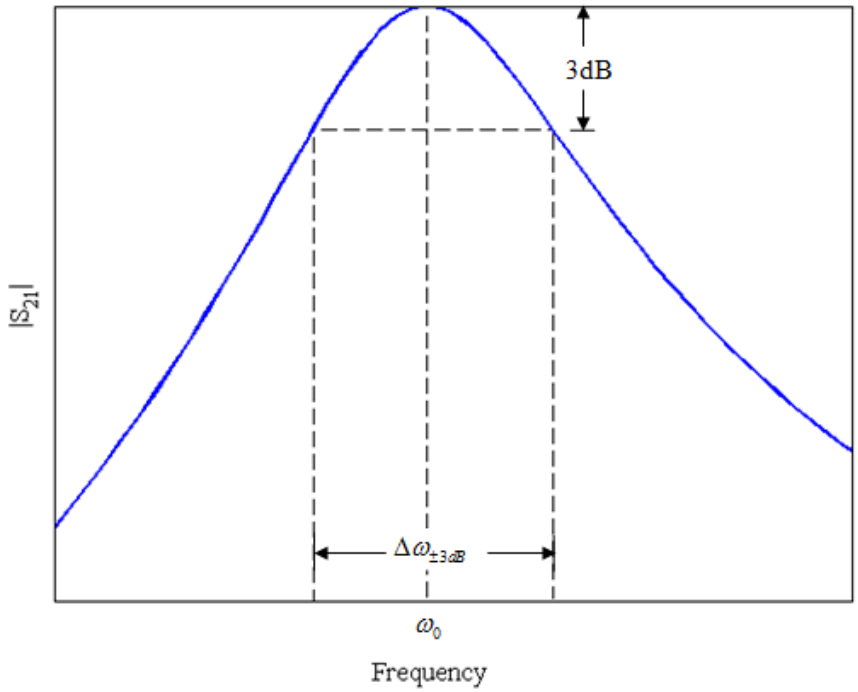

Figure 4.6: Frequency response of a doubly loaded resonator.

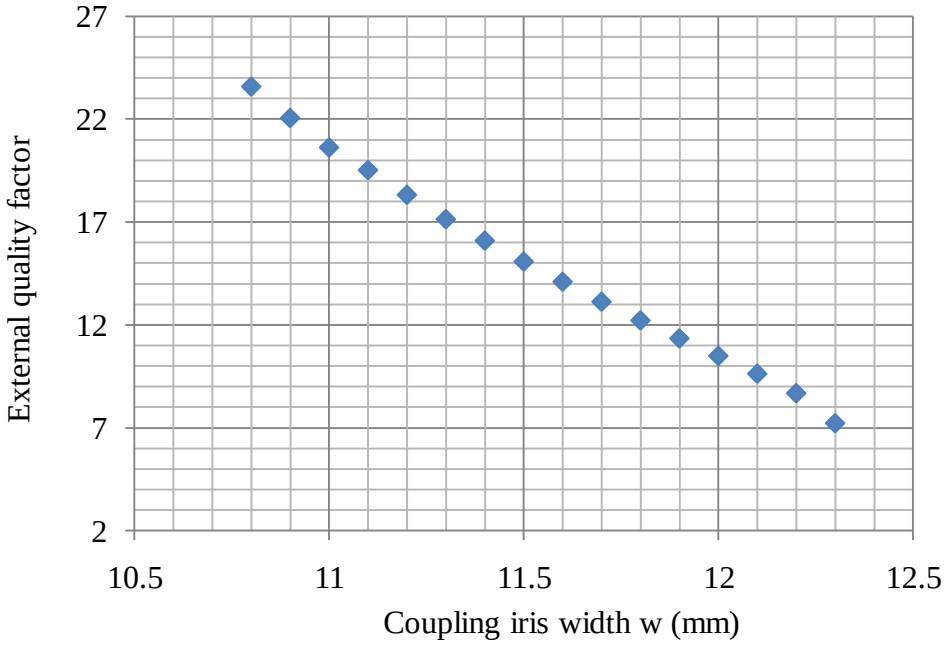

Figure 4.7: External quality factor against varying coupling iris dimensions.

4.4 Design of physical hybrid coupler dimensions

Given in Figure 4.8 is the physical model of the 90° hybrid coupler. The waveguide has an inner dimension of a by b. The lengths of the waveguides and cavity resonators are labelled with l and d, respectively. However, parameters w_0, w_1 and w_2 denote the widths of the coupling apertures. Note that the thickness of the coupling iris is chosen to be $2mm$.

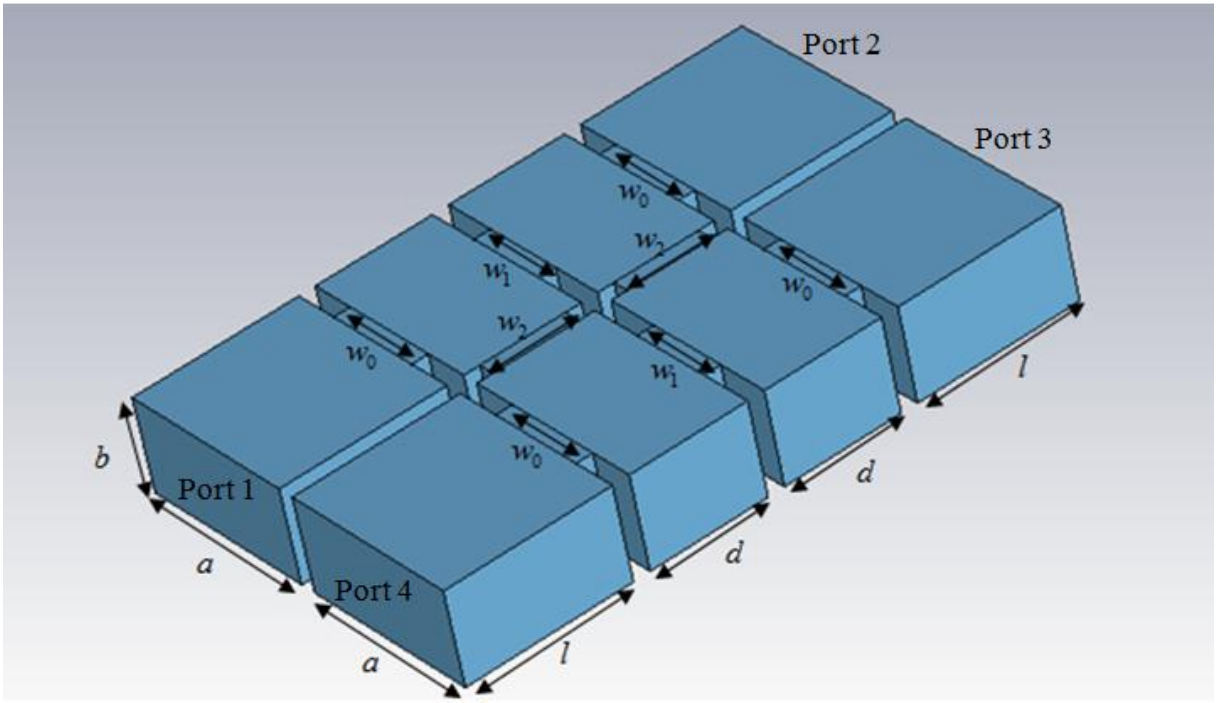

Figure 4.8: Model of the air gap inside the 90° hybrid coupler.

A 90° hybrid coupler is designed at X-band with a centre frequency of 10GHz and a 5% FBW. The standard X-band waveguide has internal dimensions of 22.86mm by 10.16mm [10]. In order to let the waveguide cavity resonant at 10GHz, the length of the waveguide cavity is calculated from (4.7) as 19.88mm.

We then calculate coupling coefficients and external quality factors from (3.47) to (3.49) as

$$[M] = \begin{bmatrix} 0 & 0.0707 & 0 & 0.05 \\ 0.0707 & 0 & 0.05 & 0 \\ 0 & 0.05 & 0 & 0.0707 \\ 0.05 & 0 & 0.0707 & 0.05 \end{bmatrix} \tag{4.13}$$

$$Q_{e1} = Q_{e2} = Q_{e3} = Q_{e4} = 20 \tag{4.14}$$

In order to use the coupling matrix and external coupling factors in the physical design of the coupler, we need to find out the relationship between these parameters and the physical dimensions. As mentioned in Section 4.2 and Section 4.3, a series of EM simulations can be performed by CST to produce plots of coupling coefficients and external quality factors against varying coupling iris dimensions. The plots of the coupling coefficients against varying coupling iris width are given in Figure 4.9 and Figure 4.10. Figure 4.11 shows the external quality factor plotting against varying coupling iris width.

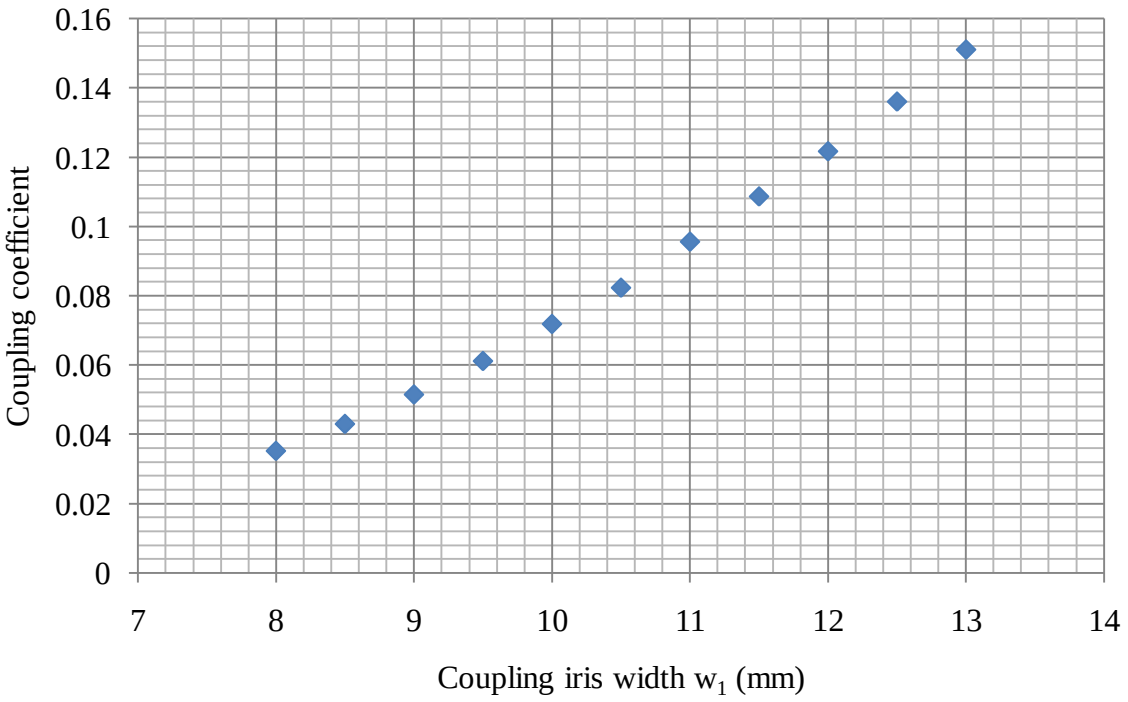

Figure 4.9: Coupling coefficient against varying iris width w_1.

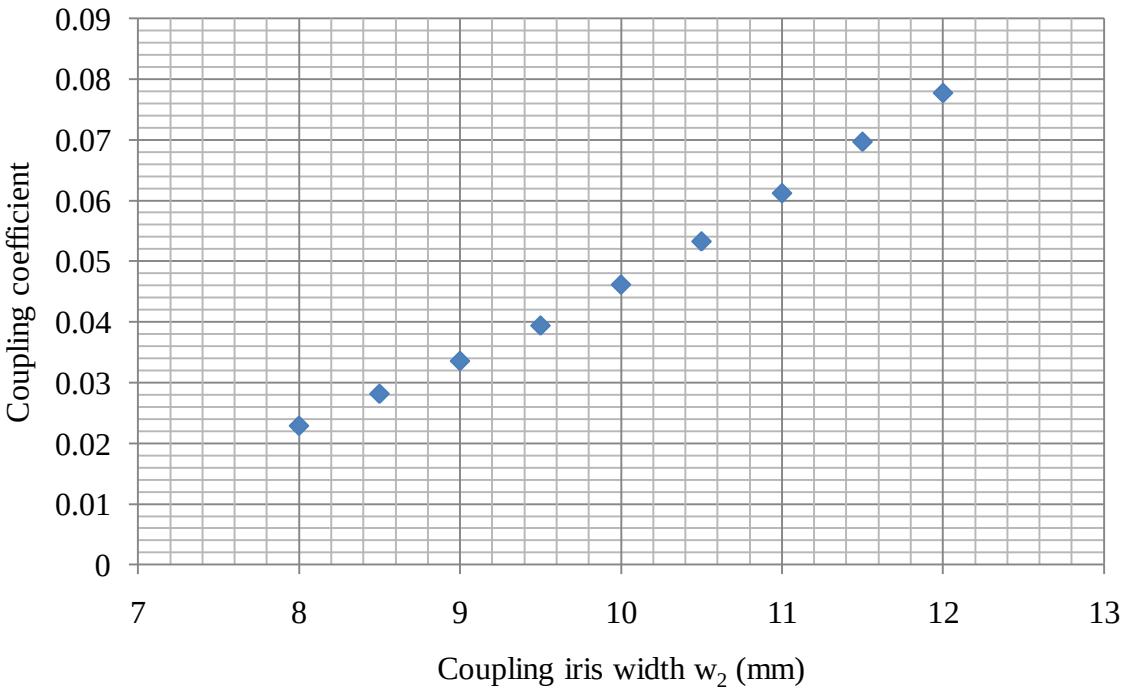

Figure 4.10: Coupling coefficient against varying iris width w_2.

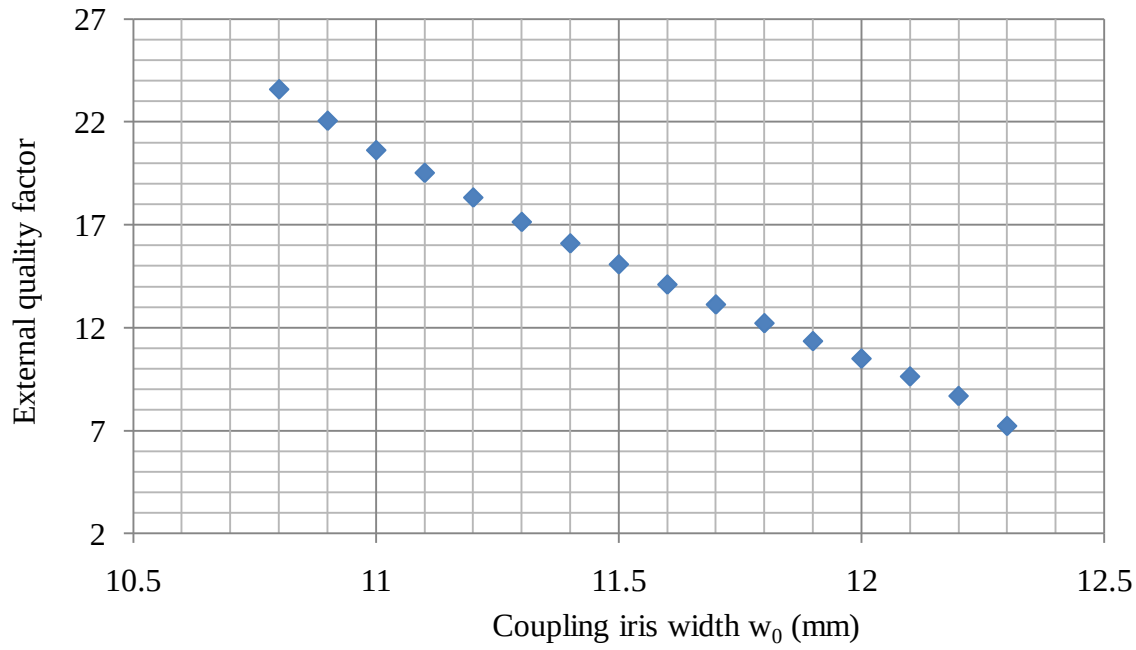

Figure 4.11: External quality factor against varying coupling iris width w_0.

The required physical dimensions of the 90 ° hybrid coupler can be read from Figure 4.9 to Figure 4.11 by finding the width of the coupling iris corresponding to the required coupling coefficient or external quality factor. Note that the introduction of external coupling iris causes a decrease in the resonant frequency, so the length of the cavity is slightly shortened until the 10GHz centre frequency is obtained.

However, this can only provide a good starting point for the design, further optimization for the best performance is needed. One common method is to use CST to perform EM simulations for the whole structure and then optimize the response. The original dimensions as well as the optimized dimensions of the 90 ° hybrid coupler are described in Table 2. With reference to Table 2, the original dimensions obtained from the theoretical analysis and the final dimensions from the optimization have a difference of less than 8%.

Table 2: Dimensions of the 90 ° hybrid coupler before and after optimization.

Parameter	**Original Value (mm)**	**Optimized Value (mm)**	**Description**
a	22.86	22.86	Width of the cavity
b	10.16	10.16	Height of the cavity
d	14.2	14.46	Length of the cavity
l	20.00	20.00	Length of the waveguide
w_0	12.05	11.77	Width of the coupling iris
w_1	10	9.2	Width of the coupling iris
w_2	10.3	10.84	Width of the coupling iris

Shown in Figure 4.12 is the frequency response of the 90° hybrid coupler before and after optimization. It can be seen that the theoretical analysis provides a good starting point for the optimization of the performance of the device.

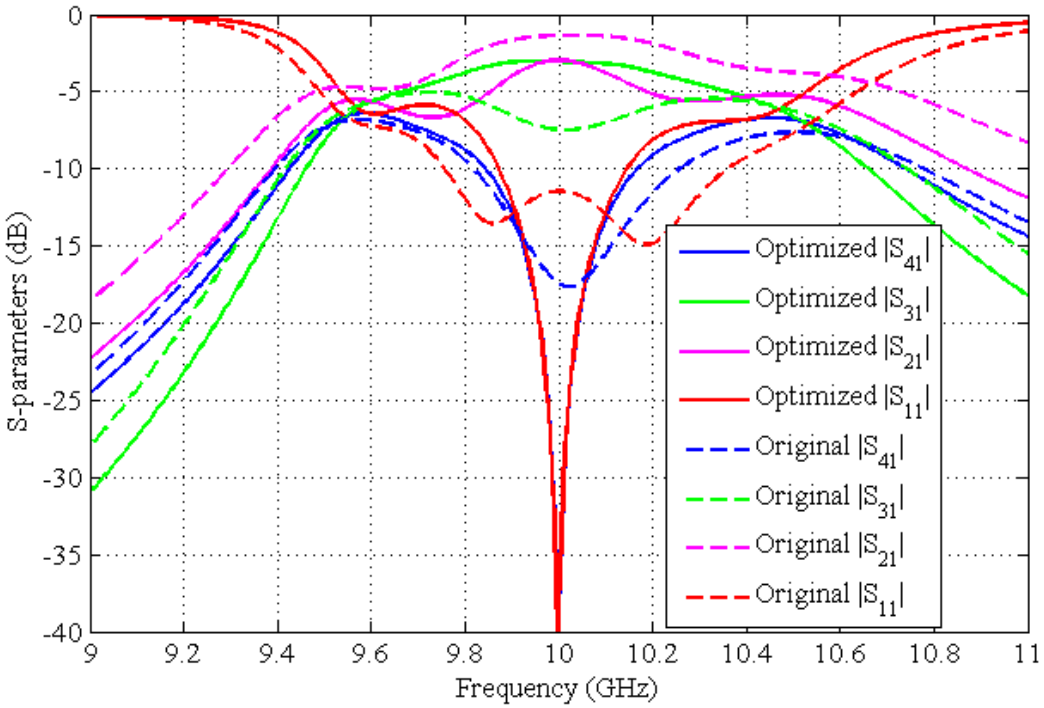

Figure 4.12: Frequency response of the 90° hybrid coupler before and after optimization.

Finally, four 90° E-plane waveguide bends of inner radius $r = 18mm$ are added to the hybrid coupler to help with the connecting to the measuring system. Figure 4.13 shows the structure of the 90° hybrid coupler with embedded waveguide bends.

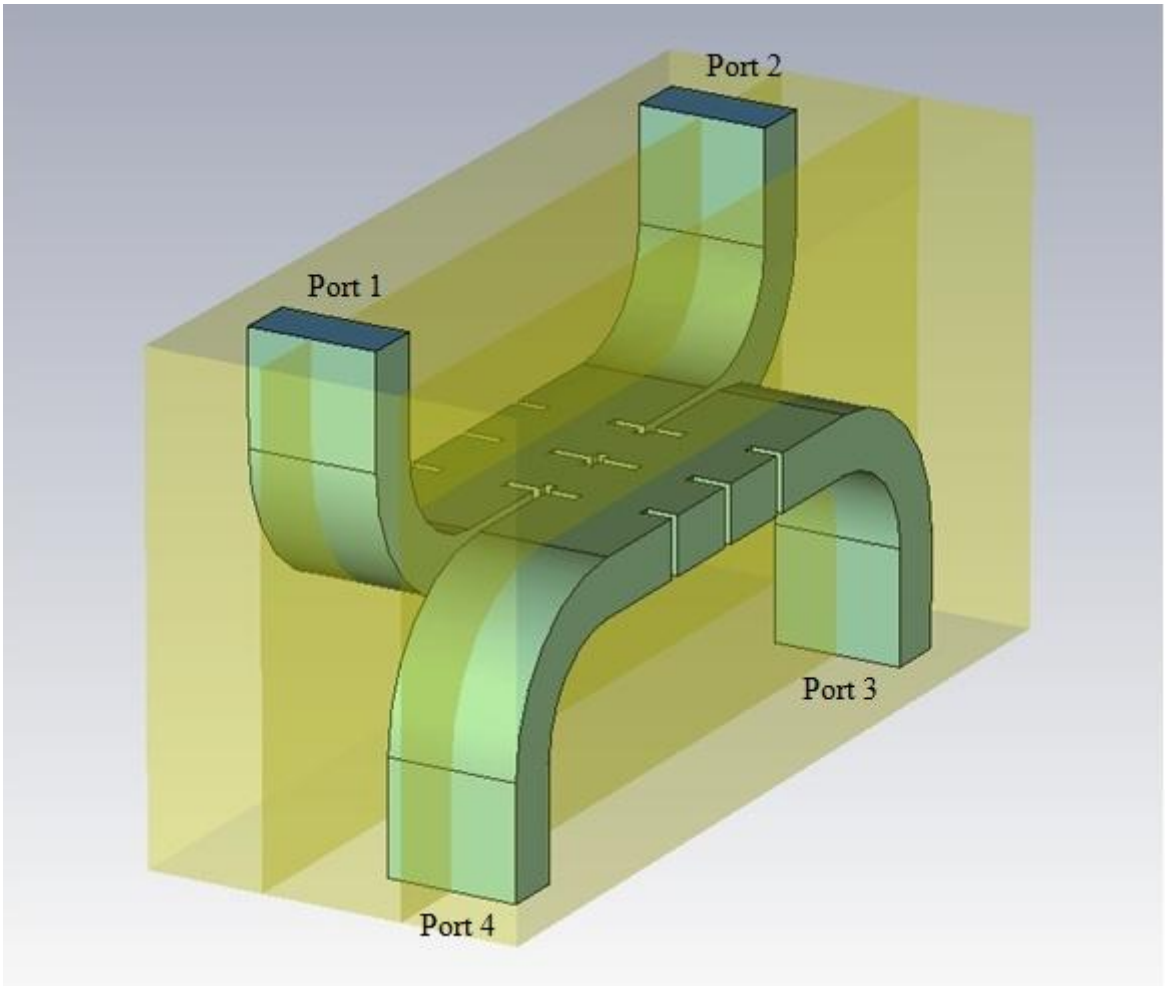

Figure 4.13: Model of the 90 °hybrid coupler with embedded E-plane waveguide bends.

4.5 Fabrication and measured results

With reference to the structure shown in Figure 4.13, the hybrid coupler can be implemented using three metal blocks. However, due to the finite radiuses of the drills used to fabricate the device, round corners must be considered when further altering the dimensions.

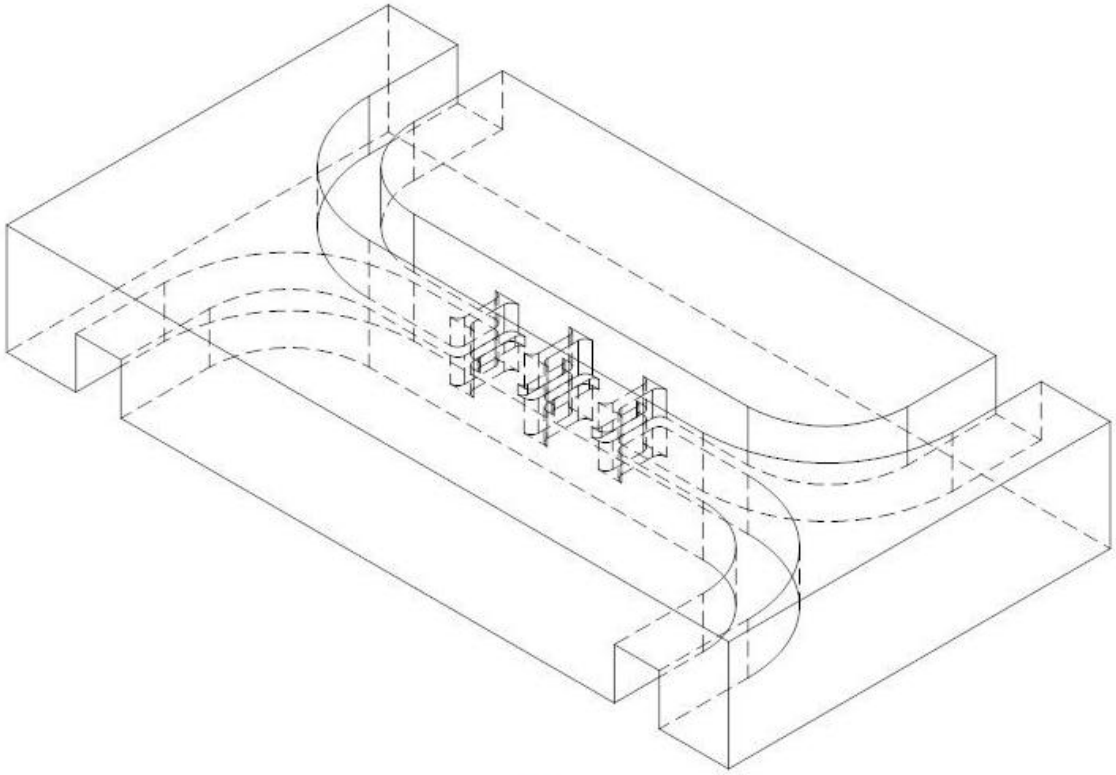

(a)

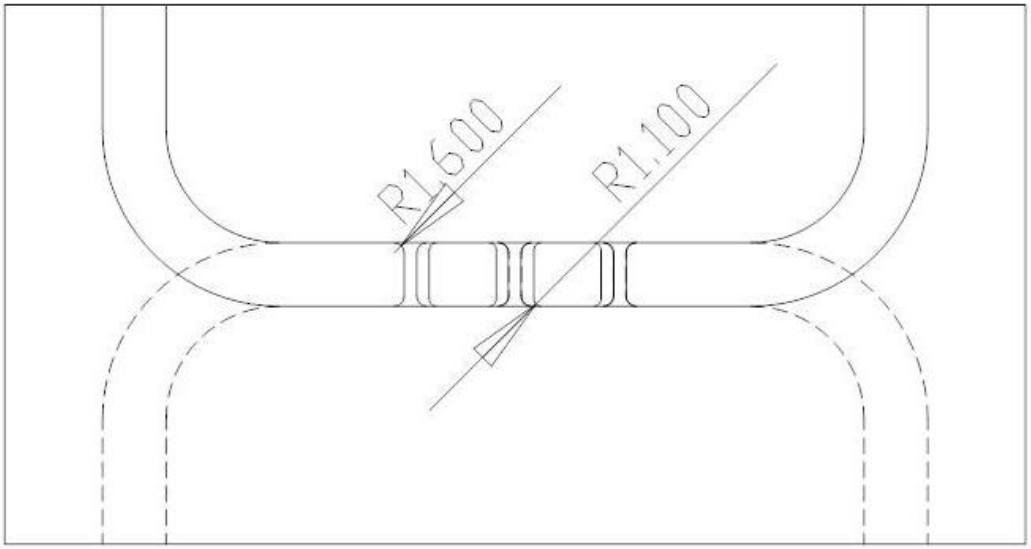

(b)

Figure 4.14: (a) 3D model of the middle block of the hybrid coupler and (b) its top view with labelled radiuses.

Shown in Figure 4.14 (a) is the 3D model of the middle block of the hybrid coupler with round corners, and its top view is given in Figure 4.14 (b), where the radiuses of round corners are $1.1mm$ and $1.6mm$.

The hybrid coupler with round corners is then simulated in CST to further optimize the response. The final optimized values of the parameters are given in Table 3. Note that the value of d is increased, and this is because the round corners reduce the effective length of the resonator.

Table 3: Dimensions of the 90 ° coupled resonator hybrid coupler with round corners.

Parameter	**Without Round Corners (mm)**	**With Round Corners (mm)**
a	22.86	22.86
b	10.16	10.16
d	14.46	14.7
l	20.00	20.00
w_0	11.77	11.77
w_1	9.2	9.2
w_2	10.84	10.72

Figure 4.15 shows photographs of the 90 ° hybrid coupler fabricated from three pieces of aluminium blocks.

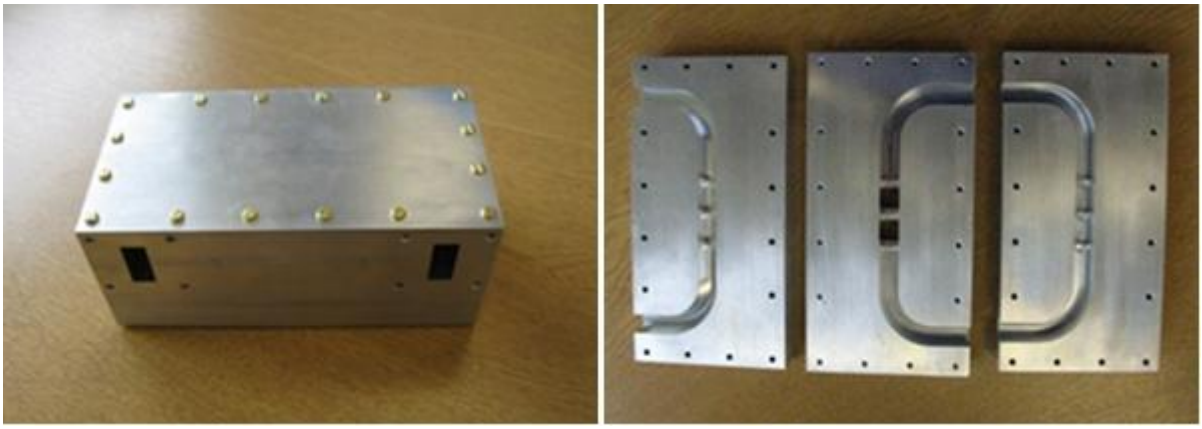

Figure 4.15: Photographs of the 90 °hybrid coupler.

Finally, the measured results of the device without tuning are given in Figure 4.16 and Figure 4.17. As can be seen, there is a good agreement between measurements and simulations. The measured magnitudes of S_{21} and S_{31} at centre frequency are within ±0.2dB from the designed -3dB. The measured phase difference between S_{21} and S_{31} at centre frequency is 87 ° compared to the simulated 90 °.

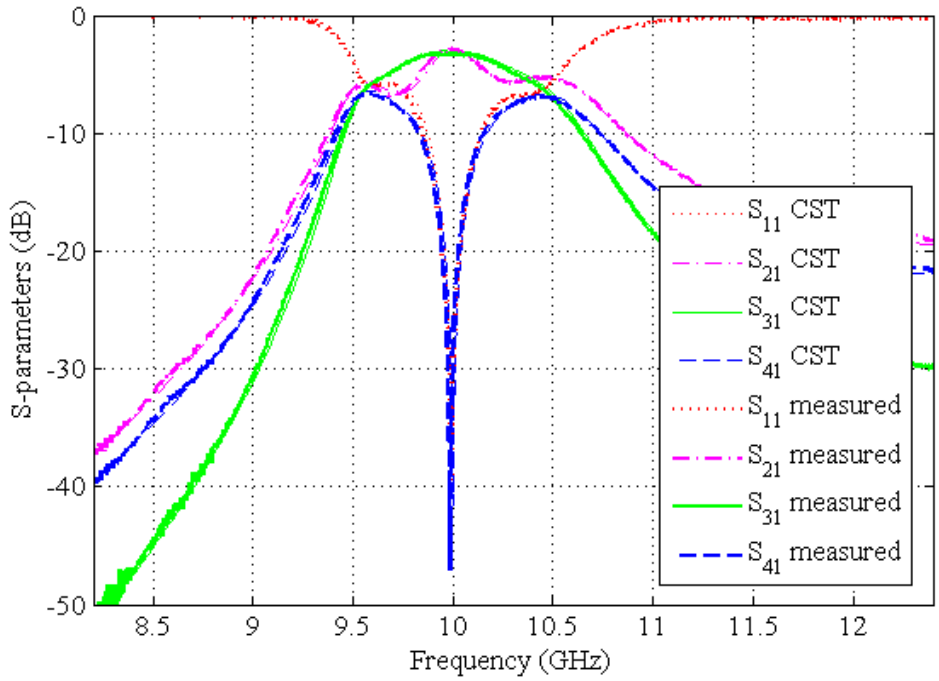

(a)

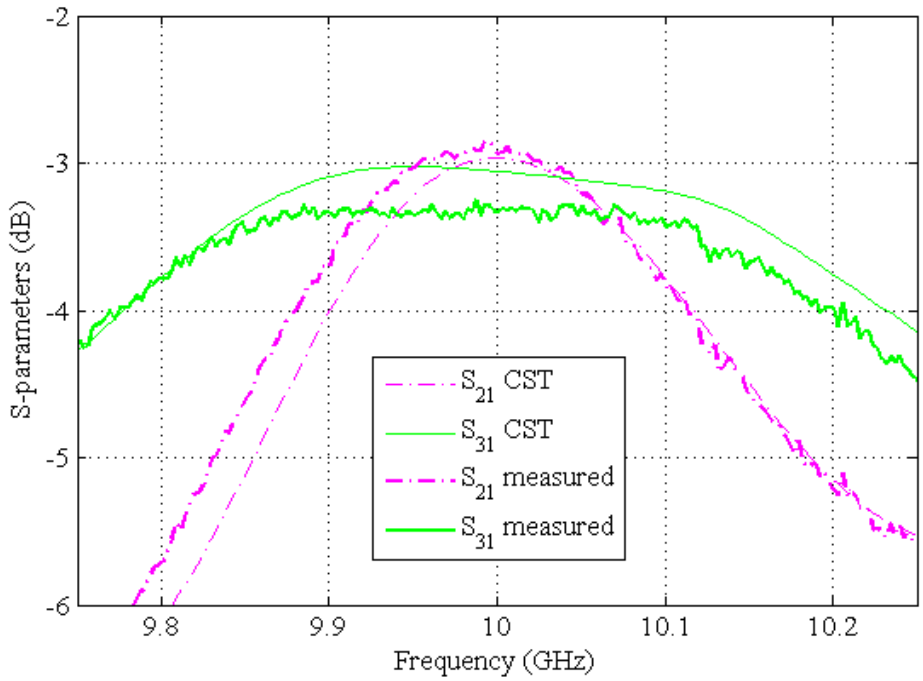

(b)

Figure 4.16: (a) Simulated and measured magnitude responses of 90 °hybrid coupler and (b) centre frequency details.

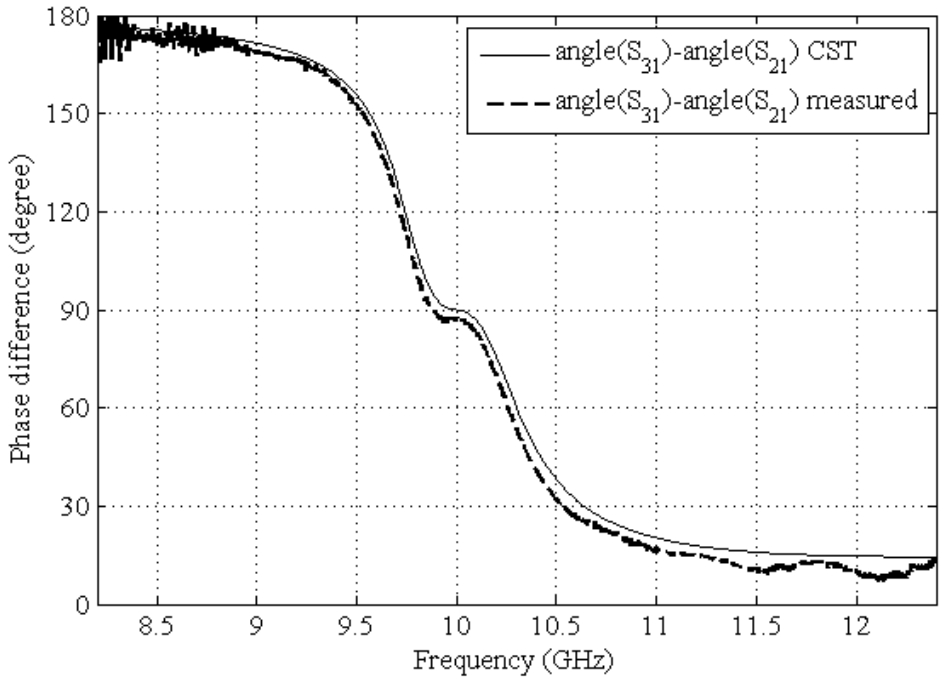

(a)

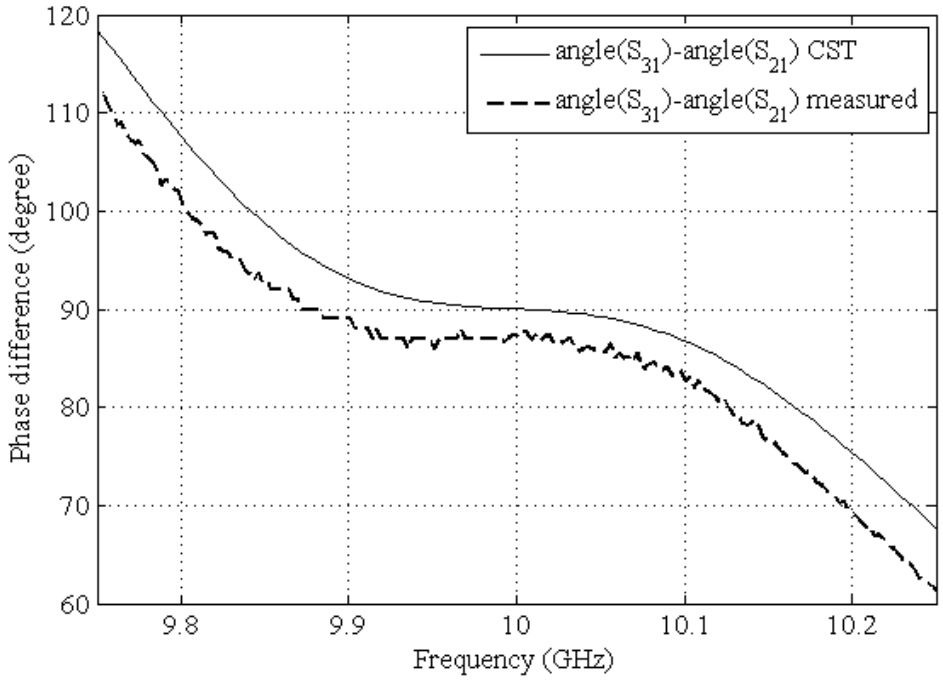

(b)

Figure 4.17: (a) Simulated and measured phase responses of the 90 ºhybrid coupler and (b) centre frequency details.

Chapter 5

Conclusions and further work

5.1 Conclusions

A general technique for the design of coupled resonator filters is based on coupling coefficients of inter-coupled resonators and external quality factors of the input and output resonators. It can be applied to any type of resonator despite its physical structure. The work presented here has extended the design techniques used for two-port filters to four-port hybrid couplers. In particular, an X-band 90 ℃oupled resonator hybrid coupler has been constructed using this principle. This thesis may be categorised into three sections, each corresponding to a step in the design process for coupled resonator hybrid couplers. The first of these steps is to obtain the possible topologies of the coupled resonator hybrid couplers. The second is the synthesis of the coupling matrix and external quality factors, achieved here by calculation from existing hybrid coupler designs. Finally, design the physical dimensions of the hybrid coupler from a particular coupling matrix and external quality factors.

The general coupling matrix is of importance for representing various coupled resonator topologies. It can be derived from a set of loop equations or a set of node equations, depending on whether the couplings are magnetic or electric. The transmission and reflection scattering parameters for four-port coupled resonator circuits have been derived in terms of the general coupling matrix. These useful formulas provide the fundamental of this work.

The equivalent circuit of the conventional branch-line hybrid coupler has been obtained by replacing each branch with its lumped element equivalent. Because the parallel resonator can

be seen as open circuit at resonance, it can be added to the conventional branch-line hybrid coupler without changes in the response at the centre frequency. Formulations used to calculate the coupling coefficients and external quality factors have been derived. A 90° four-coupled resonator hybrid coupler has been successfully synthesised based on the equivalent circuit of the conventional branch-line coupler. It has also been proven that different fractional bandwidth of the hybrid coupler can be achieved by altering the coupling coefficients and external quality factors accordingly. An improved 90° hybrid coupler has been synthesised with six coupled resonators, corresponding to the three-branch branch-line hybrid coupler. A comparison among the conventional branch-line coupler, the four-coupled resonator hybrid coupler and the six-coupled resonator hybrid coupler has been carried out with the same 3dB bandwidth. The results show that the four-coupled resonator hybrid coupler has a performance comparable with conventional branch-line, while in the six-coupled resonator hybrid coupler has a flatter frequency response near the centre frequency. The 180° six-coupled resonator hybrid coupler and an improved 180° ten-coupled resonator hybrid coupler have been synthesised based on the conventional rat-race hybrid coupler and the improved rat-race hybrid respectively.

Finally, an X-band 90° coupled resonator hybrid coupler has been implemented using waveguide cavity resonators, providing validation for using coupling matrix model in the design process for four-port coupled resonator circuits. Waveguide cavity resonators are chosen because of their high unloaded quality factors. The relationship between the coupling coefficients and the physical dimensions has been demonstrated. The frequency characteristics of the fabricated hybrid coupler agree well with the design. The measured magnitudes of S_{21} and S_{31} at centre frequency are within ±0.2dB from the designed -3dB.

The measured phase difference between S_{21} and S_{31} at centre frequency is 87° compared to the simulated 90°.

5.2 Further work

The work on coupled resonator circuits could be pursued further in several different ways. First, the coupled resonator 90° hybrid couplers can be used together with crossovers to form the Butler matrix as shown in Figure 1.12. The crossover as shown in Figure 5.1 is constructed from two back-to-back 90° coupled resonator hybrid couplers. The signal incident at port 1 is coupled to port 3, while the input signal at port 4 will be coupled to port 2.

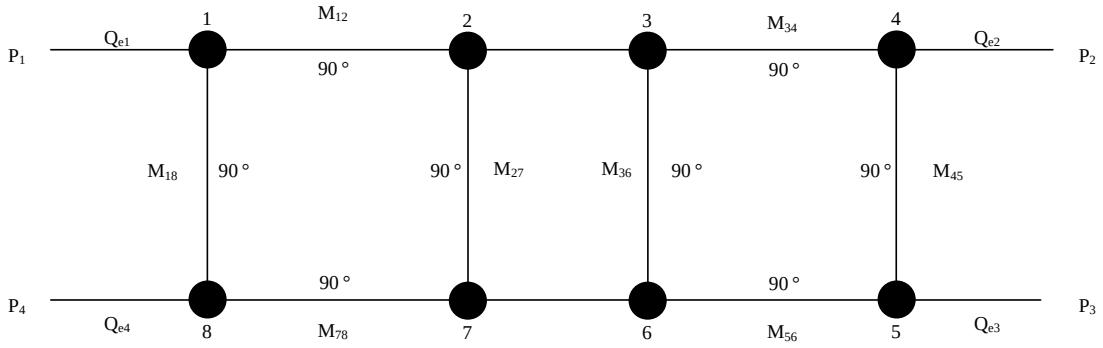

Figure 5.1: Topology of a coupled resonator crossover.

Another area where the current work could be extended is to optimize the coupling matrix so as to produce a filtering response. As presented in Section 3.4.5, the ten-coupled resonator 90° hybrid coupler has two return zeros and a maximum 25dB return loss. More complicated structures can be developed to improve the selectivity. The response of the filtering coupler can be compared with that of the conventional coupler connected with filters.

There are also opportunities to conduct research into the synthesis of more complicated devices with more input and output ports. The design procedure presented in this work can be

generalised to multi-port coupled resonator components, such as multiplexers and N-way power dividers, which are important components in microwave communication systems. As the complexity of the device increases, it may be too complicated to use the analytic solution, thus efficient optimization techniques are required to synthesis the coupling matrix.

Bibliography

[1] H. Jia-Sheng and M. J. Lancaster, "Cross-coupled microstrip hairpin-resonator filters," *Microwave Theory and Techniques, IEEE Transactions on*, vol. 46, no. 1, pp. 118-122, Jan.1998.

[2] R. J. Cameron, C. M. Kudsia, and R. R. Mansour, *Microwave filters for communication systems: fundamentals, design, and applications* Wiley-Interscience, 2007.

[3] J. S. Hong and M. J. Lancaster, *Microstrip filters for RF/microwave applications* Wiley, 2001.

[4] T. F. Skaik, M. J. Lancaster, and F. Huang, "Synthesis of multiple output coupled resonator circuits using coupling matrix optimisation," *Microwaves, Antennas & Propagation, IET*, vol. 5, no. 9, pp. 1081-1088, June2011.

[5] R. L. Haupt, *Antenna Arrays: A Computational Approach* John Wiley & Sons, 2010.

[6] Professor M Lancaster, Dr P Gardner, and Dr F Huang, "Terahertz Micromachined Resonator Superstructures," 2010.

[7] F. H. Fan, W. Ke, H. Wei, H. Liang, and C. Xiao-Ping, "Low-Cost 60-GHz Smart Antenna Receiver Subsystem Based on Substrate Integrated Waveguide Technology," *Microwave Theory and Techniques, IEEE Transactions on*, vol. 60, no. 4, pp. 1156-1165, Apr.2012.

[8] S. B. Cohn and R. Levy, "History of Microwave Passive Components with Particular Attention to Directional Couplers," *Microwave Theory and Techniques, IEEE Transactions on*, vol. 32, no. 9, pp. 1046-1054, Sept.1984.

[9] D. M. Pozar, *Microwave engineering* J. Wiley, 2005.

[10] R. E. Collin, *Foundations for microwave engineering* IEEE Press, 1992.

[11] S. A. Maas, *Microwave mixers* Artech House, 1993.

[12] A. V. Räisänen and A. Lehto, *Radio engineering for wireless communication and sensor applications* Artech House, 2003.

[13] R. J. Mailloux, *Phased array antenna handbook* Artech House, 2005.

[14] K. Fujimoto, *Mobile antenna systems handbook* Artech House, 2008.

[15] J. Butler and R. Lowe, "Beam-Forming Matrix Simplifies Design of Electronically Scanned Antennas," *Electronic Design*, vol. 9, pp. 170-173, Apr.1961.

[16] T. N. Kaifas and J. N. Sahalos, "On the design of a single-layer wideband Butler matrix for switched-beam UMTS system applications [Wireless Corner]," *Antennas and Propagation Magazine, IEEE*, vol. 48, no. 6, pp. 193-204, Dec.2006.

[17] A. Atia, A. Williams, and R. Newcomb, "Narrow-band multiple-coupled cavity synthesis," *Circuits and Systems, IEEE Transactions on*, vol. 21, no. 5, pp. 649-655, Sept.1974.

[18] H. C. Bell, Jr., "Canonical Asymmetric Coupled-Resonator Filters," *Microwave Theory and Techniques, IEEE Transactions on*, vol. 30, no. 9, pp. 1335-1340, Sept.1982.

[19] R. J. Cameron, "General coupling matrix synthesis methods for Chebyshev filtering functions," *Microwave Theory and Techniques, IEEE Transactions on*, vol. 47, no. 4, pp. 433-442, Apr.1999.

[20] R. J. Cameron, "Advanced coupling matrix synthesis techniques for microwave filters," *Microwave Theory and Techniques, IEEE Transactions on*, vol. 51, no. 1, pp. 1-10, Jan.2003.

[21] G. L. Matthaei, L. Young, and E. M. T. Jones, *Microwave filters, impedance-matching networks, and coupling structures* Artech House Books, 1980.

[22] A. Garcia-Lamperez, M. Salazar-Palma, and T. K. Sarkar, "Analytical synthesis of microwave multiport networks,", 2 ed 2004, pp. 455-458.

[23] C. Bowick, J. Blyler, and C. Ajluni, *RF circuit design* Elsevier Science & Technology, 2007.

[24] K. W. Eccleston and S. H. M. Ong, "Compact planar microstripline branch-line and rat-race couplers," *Microwave Theory and Techniques, IEEE Transactions on*, vol. 51, no. 10, pp. 2119-2125, Oct.2003.

[25] C. Kuo-Sheng, L. Ken-Min, W. Yen-Hsiu, T. Tzu-Hao, and Y. Yu-Jie, "Compact Dual-Band Branch-Line and Rat-Race Couplers With Stepped-Impedance-Stub Lines," *Microwave Theory and Techniques, IEEE Transactions on*, vol. 58, no. 5, pp. 1213-1221, May2010.

[26] H. Ghali and T. A. Moselhy, "Miniaturized fractal rat-race, branch-line, and coupled-line hybrids," *Microwave Theory and Techniques, IEEE Transactions on*, vol. 52, no. 11, pp. 2513-2520, Nov.2004.

[27] G. P. Riblet, "A Directional Coupler with Very Flat Coupling," *Microwave Theory and Techniques, IEEE Transactions on*, vol. 26, no. 2, pp. 70-74, Feb.1978.

[28] W. M. Fathelbab, "The Synthesis of a Class of Branch-Line Directional Couplers," *Microwave Theory and Techniques, IEEE Transactions on*, vol. 56, no. 8, pp. 1985-1994, Aug.2008.

[29] R. Mongia, I. J. Bahl, P. Bhartia, and J. Hong, *RF and microwave coupled-line circuits* Artech House, 2007.

[30] J. Reed and G. J. Wheeler, "A Method of Analysis of Symmetrical Four-Port Networks," *Microwave Theory and Techniques, IRE Transactions on*, vol. 4, no. 4, pp. 246-252, Oct.1956.

[31] M. Caulton, B. Hershenov, S. P. Knight, and R. E. DeBrecht, "Status of Lumped Elements in Microwave Integrated Circuits---Present and Future," *Microwave Theory and Techniques, IEEE Transactions on*, vol. 19, no. 7, pp. 588-599, July1971.

[32] H. Uchida, N. Yoneda, Y. Konishi, and S. Makino, "Bandpass Directional Couplers with Electromagnetically-Coupled Resonators," 2006, pp. 1563-1566.

[33] S. Amari, "Synthesis of cross-coupled resonator filters using an analytical gradient-based optimization technique," *Microwave Theory and Techniques, IEEE Transactions on*, vol. 48, no. 9, pp. 1559-1564, Sept.2000.

[34] R. Levy and L. F. Lind, "Synthesis of Symmetrical Branch-Guide Directional Couplers," *Microwave Theory and Techniques, IEEE Transactions on*, vol. 19, no. 2, pp. 80-89, Feb.1968.

[35] I. K. Dong and Y. Naito, "Broad-Band Design of Improved Hybrid-Ring 3-dB Directional Couplers," *Microwave Theory and Techniques, IEEE Transactions on*, vol. 30, no. 11, pp. 2040-2046, Nov.1982.

[36] "Computer Simulation Technology (CST)," 2010.

Appendix: Publications

Shuli Li, **Shani Lu**, and Michael J. Lancaster, "WR-3 Band Butler Matrix Design Using SU-8 Photo-Resist Technology," *IET seminar on Passive RF and Microwave Components*, London UK, March 2012.

WR-3 Band Butler Matrix Design Using SU-8 Photo-Resist Technology

Shuli Li, Shani Lu, Michael J. Lancaster
School of Electronic, Electrical and Computer Engineering, The University of Birmingham, U.K.
Email: sxl971@bham.ac.uk

Abstract

A design of WR-3 band 2x2 Butler Matrix feeding a 2-element slotted waveguide antenna array is presented in this paper. The whole design is based on an SU-8 multi-layer structure, which is expected to be fabricated by metal-coated SU-8 thick resist technology [1]. Each layer of the SU-8 wafer has a thickness of 0.432mm, which matches the narrow-wall height of a WR-3 (220-325GHz) waveguide. To examine the performance of the proposed Matrix, prior to adding antennas, a simulation on the 90 degree resonator based hybrid coupler was carried out using the CST Microwave Studio [2]. The simulation results agree well with the theoretical predictions, validating the proposed design.

I. Introduction

The Butler Matrix is a very attractive beamforming system due to its ability to form orthogonal beams in a simple design. This system can limit the interference of signals in order to increase the channel capacity of communication systems [3].Conventional planar structure microstrip Butler Matrices have been demonstrated [4-5]. As the development of high performance millimeter wave and sub-millimeter wave components and systems, terahertz micromachined circuits have been increasingly utilized [6]. A schematic diagram of the WR-3 band 2x2 Butler Matrix is shown in Fig1. (a). This whole structure is constructed by one 90 degree hybrid coupler and a 2-element slotted waveguide antenna array. This Butler Matrix can be extended to a 2^nx2^n Butler Matrix by increasing the number of 90 degree hybrid couplers and crossovers. The whole structure is to be fabricated on metal-coated SU-8 thick resist and is designed to be built by three layers of SU-8. Such an assembly for the Butler Matrix is illustrated in Fig.1 (b). The antenna has been realized by slotted waveguide antenna array. This antenna array structure has two elements that are spaced by λ_0 at 270GHz in order to fit the WR-3 band waveguide dimensions and get orthogonal beams at the same time. The coupler is shown in Fig1. (b) and is based on four resonators coupled together.

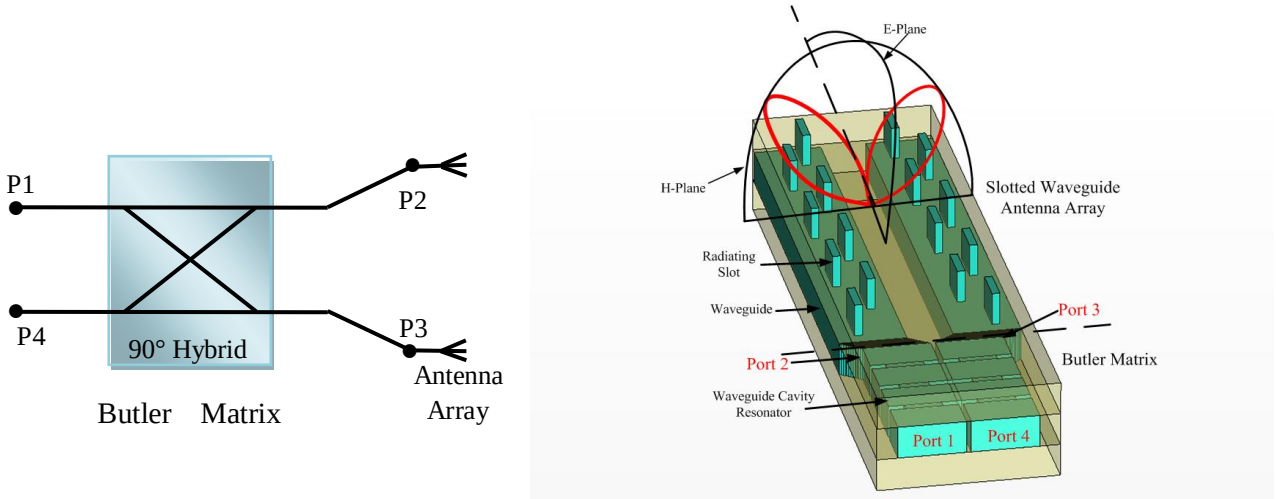

(a) (b)

Fig1. (a) Schematic Diagram for a 2x2 Butler Matrix (b) Assembly of the 2x2 Butler Matrix feeding a 2-element Slotted Waveguide Antenna Array

II. Resonator Design

The 90 degree hybrid coupler in this design is based on waveguide cavity resonators. It is developed from the conventional branch-line coupler as shown in Fig.2, which consists of two quarter-wavelength transmission line sections of characteristic impedance Z_{01}.The two transmission line sections are connected by two shunt branches, which are both quarter-wavelength transmission lines of characteristic impedance Z_{02} at both ends. The branch-line coupler has four ports with the terminal impedance Z_0. By properly choosing the values of Z_{01} and Z_{02} as$Z_{01}=0.707Z_0$ and $Z_{02}=Z_0$ separately, this circuit can operate as a 90 degree hybrid coupler with equal power split at ports 2 and 3 [7].

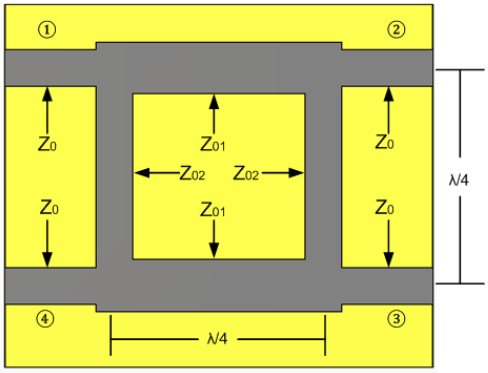

Fig.2 Branch-line Directional Coupler in Microstrip

To implement the resonator based 90 degree hybrid coupler, four resonators with appropriate couplings between each other are introduced [8]. The correct external quality factor (Qe) between ports and resonators also need to be taken into consideration. The topology of this hybrid coupler is shown in Fig.3, as circles of this represent the resonators, while the couplings are depicted by the lines between the circles.

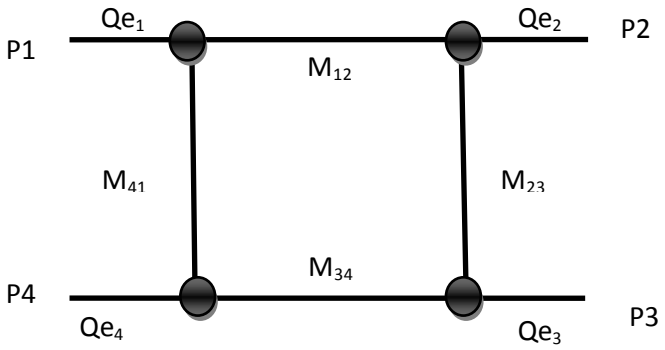

Fig.3 Topology of the Coupled Resonator 90 Degree Hybrid Coupler

For a 90 degree hybrid coupler with a center frequency of 270GHz, and a fractional bandwidth (FBW) of 0.05, the coupling matrix and external quality factors can be calculated as [8-9]:

$$[M]=\begin{bmatrix} M_{11} & M_{12} & M_{13} & M_{14} \\ M_{21} & M_{22} & M_{23} & M_{24} \\ M_{31} & M_{32} & M_{33} & M_{34} \\ M_{41} & M_{42} & M_{43} & M_{44} \end{bmatrix}=\begin{bmatrix} 0 & 0.0707 & 0 & 0.05 \\ 0.0707 & 0 & 0.05 & 0 \\ 0 & 0.05 & 0 & 0.0707 \\ 0.05 & 0 & 0.0707 & 0 \end{bmatrix}$$

$$Q_{e1}=Q_{e2}=Q_{e3}=Q_{e4}=20$$

Fig.4 (a) shows the frequency response of this 90 degree hybrid coupler with the center frequency 270GHz, and FBW=0.05. Fig4. (b) is the phase difference between port2 and port3, it is 90 degree at the center frequency.

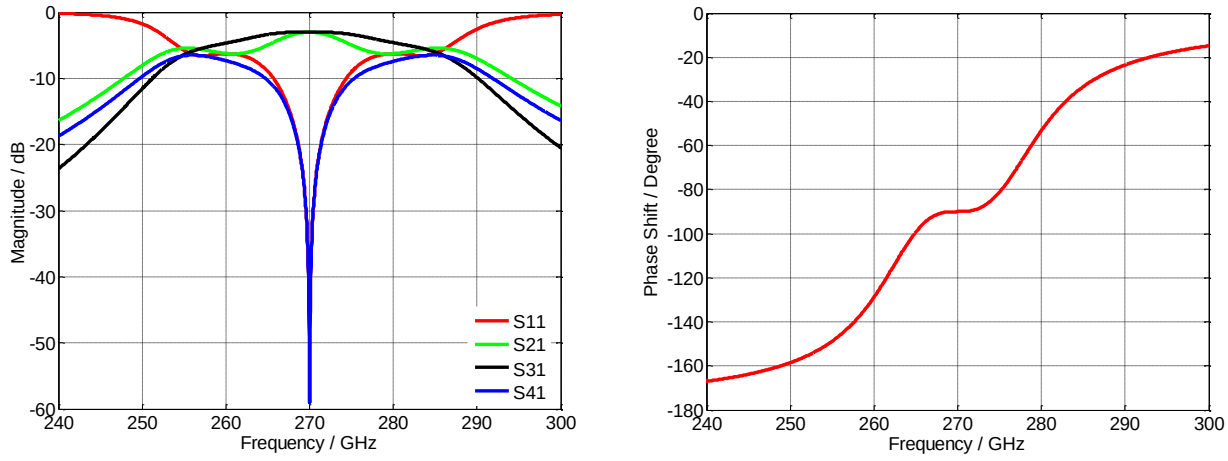

(a) (b)

Fig4. (a) Frequency Response of Magnitude for the 90 Degree Hybrid Coupler calculated from coupling matrix. (b) Frequency Response of Phase Shift Between S21 and S31 for the 90 Degree Hybrid Coupler

III. Waveguide Design

This 90 degree hybrid coupler is implemented by cavity resonators [8], each with a length of half guided wavelength [10], the design has been tailored to suit a simple fabrication for the SU-8 photo-resist technology, for this WR-3 band hybrid coupler, it is constructed by only one layer of SU-8 wafer with a thickness of 0.432mm as shown in Fig.5. The main dimensions for the structure are illustrated in Table 1.

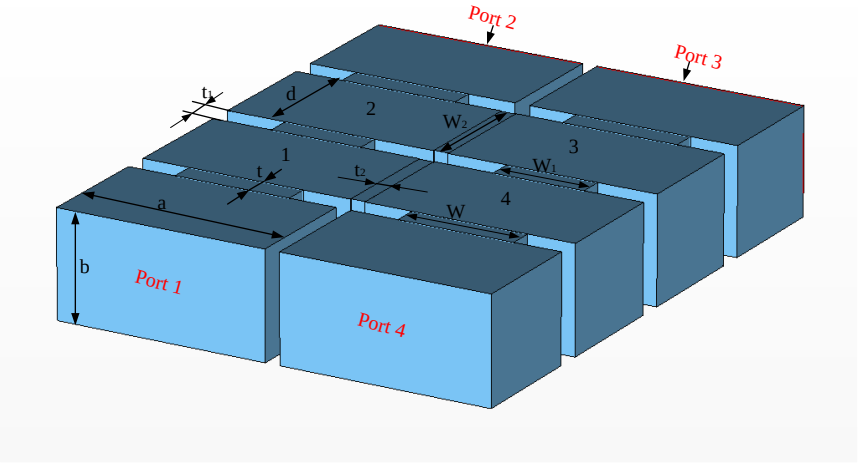

Fig.5 90 Degree Hybrid Coupler with Coupled Waveguide Cavity Resonators

Waveguide Dimensions	a x b	0.864mm x 0.432mm
Waveguide Cavity Resonator Length	d	0.495mm
Aperture Between Port and Resonator	W x t	0.475mm x 0.100mm
Aperture Between Resonator 1 and 2	W_1 x t_1	0.375mm x 0.100mm
Aperture Between Resonator 2 and 3	W_2 x t_2	0.485mm x 0.060mm

Table 1 Summary of Main Design Dimensions

The optimised frequency response simulated by CST Microwave Studio (as shown in Fig.6 (a) by dashed lines) is compared with the response calculated by the coupling matrix mentioned in Part II. It can be noted that the isolation between two output ports is -22.35dB, and the return loss (RL) is also larger than -30 dB. We can further optimize the design to get better RL and isolation, but this will degrade the responses of S21 and S31 to an extent that they cannot both get to exactly –3dB at the center frequency. Fig.6 (b) is comparison of phase difference between port 2 and port 3. From these two figures, the simulation results agree well with the theoretical calculation. The signal fed into port 1 is divided equally at port 2 and port 3 with a phase different of 90 degree.

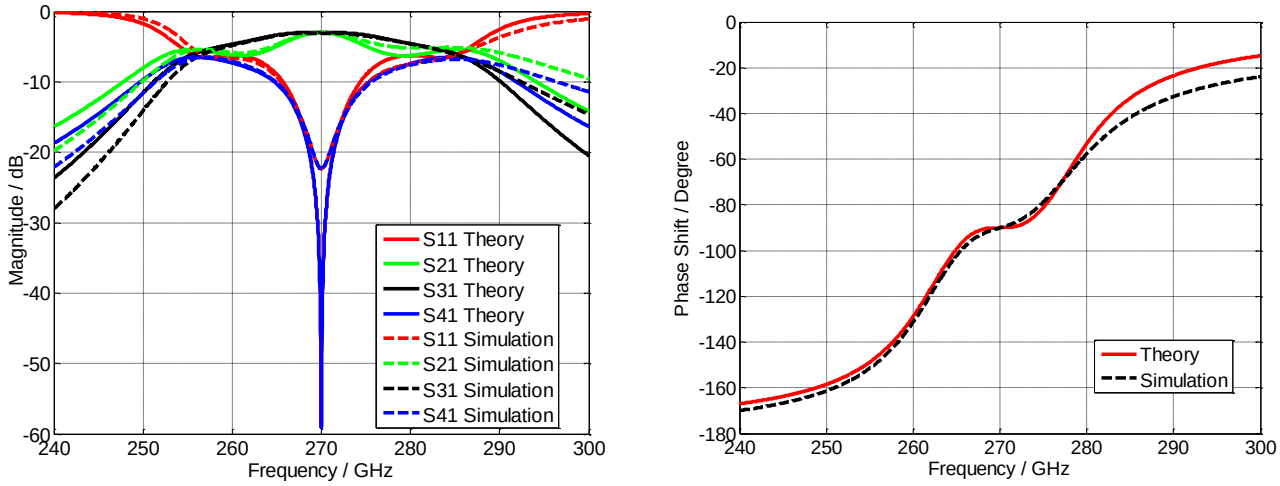

(a) (b)

Fig.6 (a) Comparison of Frequency Response for the 90 Degree Hybrid Coupler with Coupled Waveguide Cavity Resonators (b) Comparison of Phase Shift between S21 and S31 for the 90 Degree Hybrid Coupler Coupled Waveguide Cavity Resonators

IV. Future Work and Conclusion

In this paper, the idea of a WR-3 band Butler Matrix constructed by a resonator-based 90 degree hybrid coupler feeding a 2-element slotted waveguide antenna array has been implemented. All the structure is built on multi-layers and is tailored to suit the SU-8 photo-resist technology. The simulated results agree well with the theoretical calculation, which will lead to a more accurate measurement result after construction. The optimization of the 8-slot waveguide antenna will continue. Theoretical predictions of radiation patterns will be predicted in order to compare with the optimization result by CST. Experimental measurements will be carried out on this system, and the obtained results will be presented and discussed in the future.

References

[1] Jiang K, Lancaster MJ, Llamas-Garro I , "SU-8 Ka-band filter and its microfabrication", *et al. Journal of Micromechanics and Mocrpengineering*, vol. 15, pp.1522-1526, Aug.2005

[2]CST Microwave Studio Germany, CST GmbH, 2006

[3] Ming-Ju Ho, Stuber,G.L., Austin, M.D., "Performance of switched-beam smart antennas for cellular radio systems" , *IEEE Trans. Veh. Technol.*, vol.47, no. 1, pp. 10-19, Feb. 1998

[4]Denidni,T.A., Libar, T.E., "Wide band four-port butler matrix for switched multibeam antenna arrays", *IEEE Proc. PIMRC 2003*, vol. 3, pp. 2461-2464, Sep.2003

[5] C.Tseng, C.Chen, T.Chu, "A Low-Cost 60-GHz Switched-Beam Patch Antenna Array With Butler Matrix Network", *IEEE Antennas Wirless Propag. Lett.*, vol. 7, pp. 432-435, 2008

[6] I. Llamas-Garro, A. Corona-Chavez, "Micomachined Transmission Lines for Millimetre-wave Applications", *2006 Int. Conf. on Electronics, Communications and Computers*, pp. 15, Feb. 2006

[7]Rajesh Mongia, Inder Bahl , Prakash Bhartia, "RF and Microwave Coupled-Line Circuits", Artech House Microwave Library, 2nd Edition, May. 1999

[8] Lu Private Communication, to be published in PhD thesis, the University of Birmingham

[9]Hong, J., and Lancaster, M.J.: "Microstrip Filters for RF/Microwave Applications", John Wiley & Sons, Inc, 2001

[10] Robert S. Elliott, "An introduction to Guided Waves and Microwave Circuits". Prentice-Hall International Editions, 1993